Thesis

Cosmological constraints: anisotropic dark energy, the Hubble constant, and the neutrino mass

CARDONA CASTRO, Wilmar

Abstract

Nous avons tout d'abord étudié les causes fondamentales de l'accélération de l'expansion de l'univers. Nous nous sommes interrogés sur les effets de la présence d'un stress méchanique anisotrope dans les perturbations de matière et d'énergie sombres, de même que dans les propriétés statistiques du fond cosmique des micro-ondes. Deuxièmement, nous avons estimé l'importance toute particulière de l'effet de lentille gravitationnelle lorsque l'on analyse les données d'un catalogue de galaxies tel que EUCLID. On a montré que négliger cet effet dans les contraintes cosmologiques de la masse de neutrinos fausserait les mesures de leur masse, empêchant ainsi une des résultats essentiels des futurs catalogues de galaxies. Troisièmement, nous avons développé une méthode statistique qui emploie des hyperparamètres Bayesiens afin de mesurer le paramètre Hubble avec les données disponibles. Cette approche permet un traitement compréhensif des ensembles de données disponibles sans l'utilisation d'algorithmes arbitraires pour le traitement de données aberrantes.

Reference

CARDONA CASTRO, Wilmar. *Cosmological constraints: anisotropic dark energy, the Hubble constant, and the neutrino mass*. Thèse de doctorat : Univ. Genève, 2016, no. Sc. 4997

URN : urn:nbn:ch:unige-905164
DOI : 10.13097/archive-ouverte/unige:90516

UNIVERSITÉ DE GENÈVE
Section de Physique
Département de Physique Théorique

FACULTÉ DES SCIENCES
Professeur MARTIN KUNZ

Cosmological constraints: anisotropic dark energy, the Hubble constant, and the neutrino mass

THÈSE

présentée à la Faculté des sciences de l'Université de Genève
pour obtenir le grade de
Docteur ès sciences, mention physique

par

Wilmar Alberto Cardona Castro

de
Palmira (Colombie)

Thèse N^o 4997

Genève
Atelier de reproduction de la Section de Physique
2016

UNIVERSITÉ DE GENÈVE

FACULTÉ DES SCIENCES

Doctorat ès sciences
Mention physique

Thèse de *Monsieur Wilmar CARDONA CASTRO*

intitulée :

"Cosmological Constraints: Anisotropic Dark Energy, the Hubble Constant and the Neutrino Mass"

La Faculté des sciences, sur le préavis de Monsieur M. KUNZ, professeur associé et directeur de thèse (Département de physique théorique), Madame R. DURRER, professeure ordinaire (Département de physique théorique), Monsieur A. HEAVENS, professeur (Astrophysics, Blackett Laboratory, Imperial College London, United Kingdom) et Madame V. PETTORINO, docteure (Institute for Theoretical Physics, University of Heidelberg, Germany), autorise l'impression de la présente thèse, sans exprimer d'opinion sur les propositions qui y sont énoncées.

Genève, le 17 octobre 2016

Thèse - 4997 -

Le Doyen

N.B. - La thèse doit porter la déclaration précédente et remplir les conditions énumérées dans les "Informations relatives aux thèses de doctorat à l'Université de Genève".

To le Salève and its steepest way up

Acknowledgements

This trip started a few years ago in Palmira, Colombia. I have no words to thank the unconditional support of my family. In particular, my parents gave the right initial conditions and have been accompanying me despite the distance. When I was in Rio de Janeiro doing my master, Marcela Ñañez helped me out with bureaucracy required by my funding agency. My Colombian friends Carlos, Rocío, Mauricio, Johanna, and Sergio encouraged me to pursue this project and made jokes at the right moment. When I was in Colombia doing my bachelor, Luis Granda and Juan Granada provided the references for my application to the scholarship I had the past four years. I thank the support of the Departamento Administrativo de Ciencia, Tecnología e Innovación (Colciencias) as well as the administrative help of LASPAU.

I am pretty grateful with Martin Kunz who gave me the opportunity to come to one of the best cosmology groups in Europe. He patiently advised my work over the past four years, introduced me to research topics, encouraged me to work on different subjects, helped me with bureaucracy, and kindly provided financial aid to make my stay in Geneva easier.

I am very thankful with Alan Heavens, Ruth Durrer, and Valeria Pettorino for accepting to be part of the jury. I also profited from their vast experience on the different projects where we worked jointly. Adam Riess kindly provided both Cepheid stars and Supernovae type Ia data before publication. Moreover, he answered questions about the data, suggested tests for one the projects in this thesis, and presented preliminary results in the conference COSMO-16.

Discussions with my collaborators Lukas Hollenstein, Francesco Montanari, and Marco Tucci were very helpful. I shared my office for about one year with Savvas Nesseris and profited from his experience. I thank Licia Verde and Raúl Jimenez for hospitality during my visit to Barcelona. I appreciated the cordial reception of Björn Malte and Valeria Pettorino during my visit to Heidelberg.

My friends in Geneva played a part in this project. Indeed, Barbara Angerer was fundamental. She stayed with me and supported me in hard moments. Moreover, she carefully read several parts of the thesis. David Mogrovejo and Florian Teischinger read both introduction and summary, and made my stay in Geneva very pleasant. Rachel Gepp backed me up from Brazil.

I am grateful with Francine Gennai-Nicole and Cécile Jaggi-Chevalley who nicely helped me with bureaucracy. Andréas Malaspinas was always available to help with computational resources and the website administration. I am thankful to Pascale Sciarini, Stella Saavedra, Gilbert Fisher, and Monique Vatter for helpful discussions. Finally, I thank Yves Roset who gave me the opportunity to be part of his association and read the French version of the abstract.

Abstract

This thesis focused on cosmological constraints. First, we investigated the problem of determining the fundamental causes of the universe's accelerated expansion. We studied how the presence of a non-zero dark energy anisotropic stress impacts both the dark matter and dark energy perturbations, as well as Cosmic Microwave Background (CMB) angular power spectrum. Second, we investigated the impact of neglecting lensing convergence when analysing data from a EUCLID-like survey. We showed that neglecting lensing convergence when constraining neutrino masses would lead to spurious detection of their absolute mass scale, thus hindering one of the key goals of future surveys. Third, we developed a statistical method using Bayesian hyper-parameters to measure the Hubble constant H_0 with available data. The method allows a comprehensive treatment of available data sets with no need for arbitrary outlier rejection algorithms. Our best estimate of $H_0 = 73.88 \pm 2.16 \mathrm{km\,s^{-1}\,Mpc^{-1}}$ is in good agreement with previous direct measurements, but it is slightly less precise. This can be understood since our method reveals remaining inconsistencies among the data sets.

Résumé

Le contenu de cette thèse a pour sujet les contraintes cosmologiques. Nous avons tout d'abord étudié les causes fondamentales de l'accélération de l'expansion de l'univers. Nous nous sommes interrogés sur les effets de la présence d'un stress méchanique anisotrope dans les perturbations de matière et d'énergie sombres, de même que dans les propriétés statistiques du fond cosmique des micro-ondes (Cosmic Microwave Background). Dans un second temps, nous avons estimé l'importance toute particulière de l'effet de lentille gravitationnelle lorsque l'on analyse les données d'un catalogue de galaxies tel que EUCLID. On a montré que négliger cet effet dans les contraintes cosmologiques de la masse de neutrinos aurait pour conséquence de fausser les mesures de leur masse, empêchant ainsi une des résultats essentiels des futurs catalogues de galaxies. Dans une troisième, nous avons développé une méthode statistique qui emploie des hyperparamètres Bayesiens (Bayesian hyper-parameters) afin de mesurer le paramètre Hubble H_0 avec les données disponibles. Cette approche permet un traitement compréhensif des ensembles de données disponibles sans l'utilisation d'algorithmes arbitraires pour le traitement de données aberrantes. Notre meilleur mesure de $H_0 = 73.88 \pm 2.16 \mathrm{km\,s^{-1}\,Mpc^{-1}}$ correspond parfaitement avec les mesures précédentes. Néanmoins, elle a une incertitude plus grande. Ceci s'explique par le fait que la méthode utilisée met en évidence des incohérences entre les ensembles de données.

Contents

Introduction

The 20th century gradually saw the emergence of the standard model of cosmology. A linear relation between distances and recession velocities of galaxies [1], the observed abundance of chemical elements in the universe [2–5], and the existence of the Cosmic Microwave Background radiation (CMB) [5, 6] evidenced a dynamical rather than static universe: the universe is expanding. Observations of type Ia supernovae in 1998 [7, 8] modified a "little bit" the picture, setting one of the most important problems cosmologists will be addressing in the 21st century: the universe is not only expanding, it is speeding up and cosmologists want to find out why.

The cosmological principle – the assumption that the universe at sufficiently large scales is homogeneous and isotropic – is one of the cornerstones of the concordance model of cosmology [9, 10]. If one assumes there is no charge asymmetry in the universe [11], the only relevant interaction on large scales is gravity. In the vanilla model of cosmology the gravitational interaction is described by Einstein's General Relativity. Solutions for Einstein's field equations – that couple geometry to both matter-energy and pressure – satisfying the cosmological principle are known the since early 20th century [12–15]. In those solutions – the so-called FLRW metric – the expansion of the universe is given by the scale factor $a(t)$, a function which depends on the cosmic time t and scales the distance between two given points as the universe expands. The matter content in the standard model of cosmology is only partially given by particles in the Standard Model (SM) of particle physics (i.e., photons, electrons, and so on). The remaining matter, dubbed Cold Dark Matter (CDM) because it only seems to interact with the baryonic matter through gravity, is required, for instance, to fit observations of galaxy velocities in galaxy clusters [16]. Finally, in order to describe the accelerated expansion of the universe, the concordance model of cosmology reintroduces the cosmological constant Λ (first introduced by Albert Einstein in the early 20th century). The standard model of cosmology is thus named ΛCDM model.

The universe is obviously not completely homogeneous since inhomogeneities exist, such as galaxies and clusters of galaxies. Moreover, both the convergence of observations into a flat universe and the fact that the CMB appears to be incredibly uniform in regions now still causally disconnected make the ΛCDM model an incomplete description of the universe. These three main difficulties of the standard model of cosmology (i.e., structure formation, horizon, flatness) can be solved by adding an inflationary epoch to the history of the universe [17]. In the simplest inflationary scenarios the potential energy of a scalar field drives an exponential expansion in the very early universe rendering the universe extremely flat very quickly (within about 10^{-35} s). The universe would have evolved from a tiny patch (about 10^{-26} m) where regions that are today causally isolated were then in causal contact thus solving the horizon problem of the standard model of cosmology. Perhaps most importantly, inflationary models predict that quantum fluctuations of the scalar field in the early stage of the universe would have seeded the density fluctuations we observe today in the form of galaxies, galaxy clusters, and CMB fluctuations.

Over the past three decades cosmology has become more and more precise. Full sky CMB experiments such as Cosmic Background Explorer (COBE) [18], Wilkinson Microwave Anisotropy Probe (WMAP) [19], and PLANCK satellite [20] have measured CMB anisotropies in different frequencies and on a wide range of angular scales thus allowing a careful study of the predictions made by the inflationary ΛCDM model and determine its parameters. The CMB spectrum matches incredibly well that of a black body with temperature 2.7 K as predicted by the standard model [5]. By investigating CMB fluctuations cosmologists have been able to constrain to high accuracy the curvature of the universe: it agrees very well with the flatness prediction of inflationary models [21]. Although rather controversial, there is no compelling evidence for significant deviations of the cosmological principle in the Planck CMB data [22]. Furthermore, current CMB experiments support the existence of dark matter and also the accelerated expansion of the universe. Galaxy surveys such as Sloan Digital Sky Survey (SDSS) have also played an important role in testing cosmological models [23, 24]. Partially mapping the distribution of mass in the universe, using observations of $\approx 10^6$ galaxies with mean red shift $z \approx 0.1$, the SDSS collaboration detected a baryon acoustic peak which is an imprint of the recombination-epoch acoustic oscillations on the low-redshift clustering of matter [25]. This detection confirms a prediction of the standard cosmological theory. Upcoming galaxy surveys offer thus an important complementary probe and will be key for testing cosmological models in the near future, for instance to determine the neutrino mass.

The current concordance cosmological model, although both simple and a good fit

for current data sets, lacks in fundamental grounds. On the one hand, it assumes the existence of dark matter which thus far has not been directly observed; the only known dark matter candidate being neutrinos. On the other hand, the cosmological problem poses a serious conundrum for quantum field theory which is unable to explain the extremely tiny observed value of the vacuum energy. Numerous alternative approaches to explain the accelerated expansion of the universe from first principles have been proposed over past years. In one family of models evolving scalar fields – easily found in fundamental theories of matter – have been used to model dark energy as a fluid driving the late-time acceleration [26]. Another family of models exploits the ambiguity of the cosmological constant in the Einstein field equations and proposes that modifications of General Relativity – the theory of gravity in the concordance model – could be the reason that accounts for the speeding up of the universe [27]. Therefore although remarkable progress has been made on both theory and observation, degeneracies at the model level[1] remain and efficient ways to discriminate cosmological models are needed.

In Chapter 1 of this thesis Lukas Hollenstein, Martin Kunz and I have considered one possibility for breaking degeneracies at the model level. Dark energy anisotropic stress is a key feature as it allows to discriminate the standard dynamical dark energy model – a scalar field minimally coupled to gravity– from the so-called modified gravity models. In linear theory, the former class of models does not support any anisotropic stress whereas models such as scalar-tensor and $f(R)$ generically have a non-zero anisotropic stress. We have adopted a phenomenological approach and studied a model of anisotropic dark energy which encompasses both internally and externally sourced anisotropic stress, that additionally allows for a scale dependence [30]. In particular, we have investigated how the presence of a non-zero dark energy anisotropic stress impacts both the dark matter and dark energy perturbations, as well as CMB angular power spectrum. We found approximate solutions for both dark matter and dark energy perturbations in some particular scenarios and constrained dark energy anisotropic stress parameters with recent data sets.

Gleaning information about cosmological parameters from all the available data sets will surely shed light on the shortcomings of the ΛCDM model. Indeed, upcoming galaxy surveys such as Dark Energy Survey (DES), Dark Energy Spectroscopic Instrument (DESI), Large Synoptic Survey Telescope (LSST), Physics of the Accel-

[1]The situation is even worse taking into account the number of inflationary scenarios which are compatible with current observations. Although non-Gaussianity of CMB fluctuations was expected to break the degeneracy in inflationary models, the 2015 Planck results [28, 29] showed that there are still several inflationary models compatible with observations.

erating Universe Survey (PAUS), and EUCLID will play a key role in understanding the accelerated expansion of the universe and constrain the neutrino masses. The coming of all this new data will require very careful analyses and appropriate modelling of the statistical properties of the matter density field. In particular, since those galaxy surveys will probe scales comparable to the horizon, analyses must properly include relevant relativistic effects. In Chapter 2 of this thesis, Ruth Durrer, Martin Kunz, Francesco Montanari and I have investigated the impact of neglecting lensing convergence when analysing data from a EUCLID-like survey. We have shown that neglecting lensing convergence when constraining neutrino masses, for instance, would lead to spurious detection of their absolute mass scale, thus hindering one of the key goals of future surveys [31]. Moreover, we found that since biases of cosmological parameters in analyses neglecting lensing might reach several standard deviations, the usual linear approximation in Fisher matrix formalisms breaks down, therefore it might no longer be appropriate. We have then adopted a Markov Chain Monte Carlo (MCMC) approach to yield reliable forecasts.

Reliable, accurate, model independent measurements of the Hubble constant H_0 are essential to understand the physics behind the phenomenologically successful ΛCDM model. Accurate and precise determinations of H_0 will make possible to put tighter constraints on dark energy parameters – such as the equation of state for dark energy w – and the mass of neutrinos. Although direct measurements of H_0 have proven to be difficult (e.g., control of systematic errors, relatively small data sets, fully consistency of different methods for measuring distances), remarkable progress has been achieved over past decades; improvements include an enlarged sample of SNe Ia hosts having a Cepheid calibrated distance, reduction of uncertainties on anchor distances, and increase of infra-red observations of Cepheid stars. All these efforts have yielded a direct H_0 measurement almost as precise as the indirect determination for the ΛCDM model derived by the Planck collaboration [21, 32]. The group led by Adam Riess has recently found a H_0 value which is in about 3σ disagreement with that derived from CMB measurements [32]. The reasons underlying this tension are unclear (e.g., remaining CMB systematics, issues with utilised statistical methods), but if the disagreement is proved robust, it might signify new physics. In Chapter 3 of this thesis, Martin Kunz, Valeria Pettorino, and I have developed a statistical method using Bayesian hyper-parameters to measure the Hubble constant with the available data. The method allows a comprehensive treatment of the available data sets with no need for arbitrary outlier rejection algorithms. Our measurement of H_0 is slightly less precise than that by Riess et al. [32], but we understand this as a result of inconsistencies in the data sets.

Chapter 1

Traces of dark energy anisotropic stress

1.1 Introduction

The last twenty years have witnessed a revolution in observational cosmology, with an incredible growth of data available to cosmologists. When interpreted within the cosmological standard model, one consequence of the observations is the need for an accelerated expansion of the Universe. To drive this acceleration a new constituent is required, called dark energy. The main candidate model for the dark energy is the cosmological constant Λ, but this model suffers from severe fine-tuning issues. Even though cosmologists have been very active and have invented a large number of other possible models, including modifications to general relativity as the theory of gravity, none of them appear like natural candidates for the dark energy (see e.g. [26, 27, 33–36] for reviews).

The jury is therefore still out concerning the nature of the dark energy, and it may be preferable to approach the problem from the observational side, by characterising the possible observational consequences of the dark energy, and then investigating the link between those and its physical nature. (See e.g. [37] for a short review, as well as [38–42] for recent works on parameterised or effective action approaches.)

Useful quantities that are close to the observations are the functions that describe the metric [39, 43–46]. If we only use quantities up to first order in perturbation

theory, and keep only scalar perturbations, then the metric can be written as

$$g_{\mu\nu}dx^\mu dx^\nu = a^2\left\{-(1+2\psi)\ d\eta^2 + (1-2\phi)\ \delta_{ij}dx^i dx^j\right\}\ , \tag{1.1}$$

where we used the longitudinal gauge. The relevant quantities then are the scale factor $a(\eta)$, or equivalently the Hubble parameter $H(\eta)$, and the two gravitational potentials $\phi(k,\eta)$ and $\psi(k,\eta)$. The evolution of the Hubble parameter is measured by probes like the luminosity distance to type-Ia supernovae (SNe Ia) or the baryonic acoustic oscillations (BAO). Possible probes of the gravitational potentials include weak lensing which measures the integral of $\phi+\psi$, the motion of test particles which is governed by ψ or also the integrated Sachs-Wolfe (ISW) effect of the cosmic microwave background (CMB) or the large-scale distribution of galaxies.

The standard dynamical dark energy model invokes an additional minimally coupled scalar field, possibly with a non-canonical kinetic term. An important feature of this class of models is that the scalar field does not support any anisotropic stress in linear theory, i.e. the space-space part of its energy-momentum tensor has only a trace contribution. So-called modified-gravity models, which include scalar-tensor, $f(R)$, brane-world and similar models, generically have a non-zero (effective) contribution to the anisotropic stress. As a non-zero anisotropic stress manifests itself through a gravitational slip, $\phi \neq \psi$, the effective anisotropic stress provides a crucial observational test for the nature of the dark energy [47, 48].

Much of the effort in the literature has so far focused on determining observational bounds on the background evolution, usually for scalar field models without anisotropic stress (e.g. [26, 34, 36, 49]). In this project we will investigate specifically how a non-zero anisotropic stress impacts the dark energy and dark matter perturbations, as well as the CMB. For this, we use phenomenological prescriptions that are motivated by the typical behaviour of the anisotropic stress for a range of modified gravity models. We focus on two model ingredients: externally and internally sourced anisotropic stress which reflects a simplified version of a more general structure proposed in [39]. The paper is structured as follows: in the next section we briefly present the perturbation equations including anisotropic stress, which also serves to define our notation, as well as our closure relations for the pressure perturbations and the dark energy anisotropic stress. We then study the phenomenological impact of the presence of a nonzero anisotropic stress in Section 1.3, before discussing observational constraints from the CMB and geometrical probes in Section 1.4. In Section 1.5 we relate the effect of the anisotropic stress to the 'modified growth' parameterisations that are commonly used in the literature. We finally conclude in Section 1.6. The appendices contain more detailed explanations for the stability analysis as well

as some exact but cumbersome solutions of the perturbation evolution.

1.2 Models of anisotropic dark energy

1.2.1 Perturbation equations

We have already given the perturbed metric in longitudinal gauge in Eq. (1.1). A prime will stand for the derivative w.r.t. conformal time, η, and $\mathcal{H} \equiv a'/a = aH$ is the comoving Hubble parameter while H is the physical Hubble parameter that takes the value of the Hubble constant H_0 today when $a_0 = 1$. The continuity and Euler equations for the dark energy perturbations read [50–52]

$$\delta'_{de} + 3\,\mathcal{H}\left(\frac{\delta P_{de}}{\rho_{de}} - w\delta_{de}\right) + (1+w)kv_{de} - 3(1+w)\phi' = 0 \tag{1.2}$$

$$v'_{de} + \mathcal{H}(1-3c_a^2)v_{de} - k\left(\psi + \frac{\delta P_{de}}{(1+w)\rho_{de}} - \frac{2\pi_{de}}{3(1+w)}\right) = 0 \tag{1.3}$$

where the adiabatic sound speed is

$$c_a^2 \equiv \frac{P'_{de}}{\rho'_{de}} = w - \frac{w'}{3\,\mathcal{H}(1+w)}\,. \tag{1.4}$$

The evolution equations for the dark matter are the same, but with $w_m = \delta P_m = \pi_m = 0$. Notice that in terms of the often used variable σ for the anisotropic stress [52] we have that $\pi = (3/2)(1+w)\,\sigma$.

In addition to these evolution equations we need the Einstein constraint equations to compute the impact of the dark matter and dark energy perturbations on the metric. For the scalar perturbations considered here, there are two independent Einstein equations which we can take to be

$$-k^2\phi = 4\pi G a^2\left(\rho_m\Delta_m + \rho_{de}\Delta_{de}\right)\,, \tag{1.5}$$

$$k^2(\phi-\psi) = 8\pi G a^2 \rho_{de}\pi_{de}\,. \tag{1.6}$$

Here we wrote the Poisson equation (1.5) directly in terms of the comoving density perturbation Δ which is linked to the density perturbation in the longitudinal gauge δ by a gauge transformation, $\Delta = \delta + 3\,\mathcal{H}(1+w)v/k$. In the equation for the slip (1.6) we further used that $\pi_m = 0$ (which is strictly speaking only true at first order

in perturbation theory [53]). From the two equations (1.2) and (1.3) one can derive a single second order evolution equation for δ_{de} by solving the continuity equation (1.2) for v_{de} and substituting that (and its derivative) into the Euler equation (1.3). We find

$$\begin{aligned}\delta''_{de} &+ (1-6w)\,\mathcal{H}\delta'_{de} + 3\,\mathcal{H}\left(\frac{\delta P_{de}}{\rho_{de}}\right)' + 3\Big[(1-3w)\,\mathcal{H}^2 + \mathcal{H}'\Big]\left(\frac{\delta P_{de}}{\rho_{de}} - w\delta_{de}\right) \\ &- 3\,\mathcal{H}w'\delta_{de} = 3(1+w)\left[\phi'' + \left(1 - 3w + \frac{w'}{(1+w)\,\mathcal{H}}\right)\mathcal{H}\phi'\right] \\ &- k^2\left[(1+w)\psi + \frac{\delta P_{de}}{\rho_{de}} - \frac{2}{3}\pi_{de}\right]. \end{aligned} \tag{1.7}$$

To this point we did not make any assumptions on δP_{de}, π_{de} and w. However, already the last term makes clear that $k^2\pi_{de}$ acts as a source for δ_{de} while the pressure counteracts the gravitational collapse. $-k^2\psi$ is also a source because $\psi = \phi$ for vanishing anisotropic stresses and $-k^2\phi \propto \mathcal{H}^2\Delta_{tot}$.

1.2.2 Modelling the DE pressure perturbation

We define the effective, non-adiabatic sound speed of DE in its rest-frame, $\partial_\mu P_{de} \equiv c_s^2\partial_\mu\rho_{de}$. This is the form of the sound speed that e.g. K-essence type models exhibit, with $c_s^2 = 1$ for a canonical scalar field. When we perform a gauge transformation to the longitudinal gauge, we find

$$\frac{\delta P_{de}}{\rho_{de}} = c_s^2\delta_{de} + 3(1+w)\left(c_s^2 - c_a^2\right)k^{-1}\,\mathcal{H}v_{de}\,. \tag{1.8}$$

We keep the sound speed c_s as a free parameter, but assume it to be a constant.

1.2.3 Model 1: externally sourced anisotropic stress

In the quasi-static limit of DGP, the metric potentials are directly linked to the matter perturbations through a time-dependent function [54] and consequently also the anisotropic stress is proportional to Δ_m [47] with, in general, a time-dependent coefficient. Another motivation to link the dark energy anisotropic stress to the matter is the possibility of couplings between dark energy and dark matter. To keep the model simple we use

$$\pi_{de} \;\equiv\; e_\pi a^n \Delta_m \tag{1.9}$$

with a constant coefficient e_π. We will see that this term will act as an additional source for δ_{de}. When looking at the constraints from data in section 1.4 we will fix $n = 0$, which is also roughly the behaviour of the effective anisotropic stress in the DGP model.

1.2.4 Model 2: counteracting the pressure perturbation

In [55] a coupling of the anisotropic stress to the pressure perturbation was proposed, $\sigma \propto \delta P_{de}/\rho_{de}$, linking isotropic and anisotropic stresses which appears quite natural[1]. For non-zero sound speed the pressure perturbation is related to the density perturbation by our model (1.8). Here we formulate the dependence directly in terms of the comoving density perturbation since this is a gauge-invariant prescription. In addition, we allow for a different behaviour on small and large scales, with a transition scale k_T

$$\pi_{de} = f_\pi \frac{(k/k_T)^2}{1+(k/k_T)^2}\Delta_{de} \quad , k_T = g_\pi \mathcal{H}(a) \tag{1.10}$$

with constant parameters f_π and g_π. We can then write this model also as

$$\pi_{de} = \frac{f_\pi}{1+(g_\pi \mathcal{H}/k)^2}\Delta_{de}\,. \tag{1.11}$$

For $f_\pi = (3/2)c_s^2$ the anisotropic stress cancels the pressure perturbation in the Euler equation (1.3) on sub-horizon scales, but not in the continuity equation (1.2) and the Einstein constraints.

The dark energy model used here corresponds actually to a subset of the closure relations given in Eq. (2.47) of [39], although we originally started this work before those relations were derived. The pressure perturbation is just the first term of the first equation in their (2.47) with $c_s^2 = C^2$ (plus the usual contribution to Σ_1 from the gauge transformation). The externally sourced anisotropic stress contribution parameterised by e_π belongs in this context to the dark matter coupling term with parameter β_π. The second contribution to the anisotropic stress here corresponds to the first term in their (2.47), parameterised by Π. The scale-dependence in our prescription leads to a suppression on large scales, and then 'turns on' the anisotropic stress on scales $k \gg k_T$, similar to the behaviour of the non-minimally coupled

[1] A similar link was also exploited in [47] to define the pressure perturbation when mimicking DGP.

K-*essence* model described in the second part of [39] where the authors found a 'perfect' and an 'imperfect' regime. (However, here we limit ourselves to a case where effectively $M_C^2 = 0$ and $\kappa' = 0$.) For a detailed comparison to [39], notice that we use a different sign convention for the metric, and that their $(k/a)^2\delta\pi$ is our $\rho_{de}\pi_{de}$.

Our model also satisfies the constraint equations derived in [40]. These are a consequence of the Bianchi identities, which lead to $\nabla_\mu G^\mu_\nu = 0$, and of the covariant conservation of the matter energy-momentum tensor $\nabla_\mu T^\mu_\nu = 0$. The constraint equations are equivalent to the covariant conservation of the energy momentum tensor of the dark energy. For a general fluid they are equivalent to the conservation equations (1.2) and (1.3).

Anisotropic stress perturbations in dark energy have been studied before, see e.g. Refs. [56–59]. However, note that the approach taken in these references is very different to ours (and that of Refs. [47, 55]). In the former, the Boltzmann hierarchy of a generic fluid of collisional particles is truncated at the level of the anisotropic stress [60]. A viscosity parameter $c^2_{\rm vis}$ is introduced and the behaviour of anisotropic stress of radiation (up to the quadruple) is recovered for $c^2_{\rm vis} = 1/3$. It turns out that such anisotropic stress, often referred to as viscosity, tends to wash out fluctuations in the dark energy and, therefore, makes dark energy perturbations even harder to detect than in the absence of anisotropic stress. On the contrary, the models discussed here are designed to imitate typical modified gravity scenarios and therefore aim at creating very different effects, e.g. detectable gravitational slip on sub-horizon scales.

1.3 Phenomenology

From now on we consider the equation of state w as a free parameter, but assume it to be a constant. From the evolution equation of δ_{de}, Eq. (1.7), we can see that the effective source term at high k (on sub-horizon scales) is proportional to

$$k^2\left[(1+w)\psi + \frac{\delta P_{de}}{\rho_{de}} - \frac{2}{3}\pi_{de}\right] \approx k^2\left[c_s^2\Delta_{de} - \frac{2}{3}\pi_{de}\right] . \tag{1.12}$$

Here we neglected the velocity contribution $\propto v/k$ and the potential ψ, as both are suppressed by inverse powers of k relative to Δ. We then have a second-order equation for Δ_{de} with the above term proportional to Δ_{de}. If the pre-factor of Δ_{de}

in this expression is positive, then it will lead to an oscillatory behaviour of Δ_{de} and the behaviour of the dark energy perturbations on small scales will be stable. In this case Eq. (1.12) can be used to define an effective sound speed for the dark energy. If on the other hand the pre-factor is negative then we expect rapid growth of the perturbations on small scales which in general renders the model unviable.

Based on these considerations it makes thus sense to define an effective sound speed, which for the models described in the last section takes the form

$$c_{\rm eff}^2 \equiv c_s^2 - \frac{2f_\pi}{3}\,. \tag{1.13}$$

It is this effective sound speed that characterises the propagation of perturbations and the pressure support (and hence the clustering properties) on small scales (see also [39, 58, 59] where the same combination was found to be relevant). Here we also assumed that the scales of interest satisfy $k^2/\mathcal{H}^2 \gg g_\pi^2$.

Since the full system of differential equations cannot be solved analytically in general, we will focus in the next subsections on limiting cases for which dark matter and dark energy perturbations decouple from each other. In some of them we compare our results with the full numerical solutions explicitly, however we have checked for all of them that the approximate expressions show a behaviour that is representative of the full numerical solution in the relevant regime (see Figure 1.3). We found it to be convenient to solve the 4-dimensional system (1.2)–(1.3) for the dark matter and dark energy perturbations by using the dimensionless variables

$$V_m \equiv -\frac{kv_m}{\mathcal{H}}\,, \quad V_{de} \equiv -\frac{kv_{de}(1+w)}{\mathcal{H}}\,, \tag{1.14}$$

along with the density contrast variables δ_m and δ_{de}. This choice makes it simpler to expand the equations consistently in powers of k to study separately the super- and sub-horizon behaviour, and we checked that we are are able to recover the solutions for dark matter and dark energy perturbations in the matter dominated era found in [61].

1.3.1 Sub-horizon scales

On sub-horizon scales, $k/\mathcal{H} \gg 1$, we find three scenarios where dark matter and dark energy perturbations decouple. These correspond to: i) dark matter domination ii) dark energy domination without dark matter contribution to the dark energy

anisotropic stress ($e_\pi = 0$) and iii) the particular case where $f_\pi = -1/2$. Although for the last case we find analytical solutions for dark matter perturbations, they do not seem to have a special physical relevance and we will not discuss this case further.

Dark matter domination

During dark matter domination the evolution of the conformal Hubble parameter and (neglecting decaying modes and focusing on sub-horizon scales) the solutions for matter perturbations are given by (e.g. [61])

$$\mathcal{H}^2 = H_0^2 \frac{\Omega_m}{a}\,, \qquad \delta_m = V_m = \delta_0 a \tag{1.15}$$

where δ_0 is a constant. Using the solutions (1.15) it is possible to find a second order equation for the dark energy density perturbations (assuming that $k^2/\mathcal{H}^2 \gg 9(1+w)/4e_\pi a^n$) during matter domination which we can write as

$$\begin{aligned} \delta''_{de} &+ \left[\frac{3-6w+4f_\pi}{2a}\right]\delta'_{de} \\ &+ \left[\frac{9H_0^2\Omega_m(1-6c_{\rm eff}^2)(c_{\rm eff}^2+\frac{2f_\pi}{3}-w)+4f_\pi g_\pi^2 H_0^2\Omega_m+6ac_{\rm eff}^2k^2}{6a^2H_0^2\Omega_m}\right]\delta_{de} \\ &= \frac{2\delta_0 e_\pi a^n k^2}{3H_0^2\Omega_m}\,. \end{aligned} \tag{1.16}$$

In Principle, this equation can be solved analytically in terms of Bessel and hypergeometric functions (see Eq. (B.1) of Appendix B). The argument of the Bessel functions is proportional to $\sqrt{c_{\rm eff}^2}$, and as in the case of dark energy domination in Section 1.3.1, the perturbations grow exponentially fast for $c_{\rm eff}^2 < 0$ because the argument of the Bessel functions becomes imaginary. It is however more instructive to look separately at super- and sub-sound horizon limits where we can simplify the equation further and so obtain more tractable solutions.

Super-sound horizon (but sub-horizon)

The sound horizon is set by $\mathcal{H}/c_{\rm eff}$, i.e. a given k is super-sound horizon but sub-horizon if $\mathcal{H} \ll k \ll \mathcal{H}/c_{\rm eff}$. So for a clean separation of scales we need $c_{\rm eff} \ll 1$,

which means we can just take the limit $c_{\rm eff} \to 0$ in Eq. (1.16). We notice from Eq. (1.13) that if $0 \leq c_s^2 \leq 1$, then $0 \leq f_\pi \leq 3/2$.[2] We find

$$\begin{aligned} \delta''_{de} &+ \left[\frac{3-6w+4f_\pi}{2a}\right]\delta'_{de} + \left[\frac{3(2f_\pi-3w)+4f_\pi g_\pi^2}{6a^2}\right]\delta_{de} \\ &= \frac{2\delta_0 e_\pi a^n k^2}{3H_0^2\Omega_m}\,. \end{aligned} \tag{1.17}$$

The homogeneous part of the equation clearly has power-law solutions, in general the solution for Eq. (1.17) is of the form

$$\delta_{de} = A_1 a^{\frac{1-\alpha-\beta}{2}} + B_1 a^{\frac{1-\alpha+\beta}{2}} + \frac{2\delta_0 e_\pi k^2 a^{2+n}}{3H_0^2\Omega_m[2(1+\alpha)+\vartheta+n(3+\alpha+n)]} \tag{1.18}$$

where

$$\vartheta = \frac{3(2f_\pi-3w)+4f_\pi g_\pi^2}{6} \tag{1.19}$$

$$\alpha = \frac{3-6w+4f_\pi}{2} \tag{1.20}$$

$$\beta = \sqrt{1-2\alpha+\alpha^2-4\vartheta} \tag{1.21}$$

and A_1 and B_1 are two constants of integration. The last term in Eq. (1.18) is a growing mode driven purely by the external anisotropic stress (the part of the anisotropic stress coupled to Δ_m), and it can more clearly be written as

$$\delta_{de}^{(e_\pi)} = e_\pi \delta_m \left(\frac{k^2}{\mathcal{H}^2}\right) \frac{2a^n}{3[2(1+\alpha)+\vartheta+n(3+\alpha+n)]}\,. \tag{1.22}$$

The factor $(k/\mathcal{H})^2$ in this expression interpolates between 1 on horizon scales (where $k = \mathcal{H}$) and $1/c_{\rm eff}^2$ on sound horizon scales (where $c_{\rm eff}k = \mathcal{H}$), i.e. between the terms containing e_π in Eqs. (1.39) and (1.26).

We show the exponents of the homogeneous solutions as a function of the parameters f_π and g_π in Figure 1.1. For $g_\pi \lesssim 1$ we find a growing mode when $f_\pi \lesssim -1$, and for very negative f_π this mode can grow very quickly. This rapid perturbation growth will eventually lead to a conflict with observations so that we expect to find a lower limit for f_π around $f_\pi \simeq -3$ to -5 based on the growth of dark energy perturbations

[2] If c_s^2 can take negative values then f_π can be negative as well since $f_\pi = 3c_s^2/2$ when $c_{\rm eff} = 0$. This is not a problem for the stability of the perturbations, as that is governed by $c_{\rm eff}$.

during dark matter domination. For $g_\pi \gg 1$ the dark energy perturbations grow extremely fast as soon as f_π becomes negative, rendering this part of parameter space unviable. (For $f_\pi > 0$ the exponent is purely imaginary, so that the dark energy perturbations oscillate without growing.) We will see in the next section that this g_π dependent lower limit on f_π is indeed clearly visible.

With Eq. (1.18) we can also find an expression for the dark energy velocity perturbation,

$$\begin{aligned} V_{de} &= \frac{[B_1(1+4f_\pi-6w-\alpha+\beta)a^\beta + A_1(1+4f_\pi-6w-\alpha-\beta)]a^{\frac{1-\alpha-\beta}{2}}}{2} \\ &+ \frac{2e_\pi k^2\delta_0(2+2f_\pi-3w+n)a^{2+n}}{3H_0^2(2+\vartheta+2\alpha+n(3+n+\alpha))\Omega_m}\,. \end{aligned} \tag{1.23}$$

Sub-sound horizon

The equations for dark energy velocity and density perturbations in this case are given by

$$\begin{aligned} V'_{de} &+ \frac{1-6c_{\rm eff}^2}{2a}V_{de} = -\frac{c_{\rm eff}^2k^2}{H_0^2\Omega_m}\delta_{de} \\ &+ \frac{\delta_0}{6H_0^2\Omega_m}\left[4e_\pi a^{n+1}k^2 + 9H_0^2(1+w)\Omega_m\right]\,, \end{aligned} \tag{1.24}$$

$$\delta'_{de} + \frac{3(c_s^2-w)}{a}\delta_{de} = \frac{V_{de}}{a}\,. \tag{1.25}$$

Here we re-introduced the second, sub-dominant term in Eq. (1.24) for the special case $e_\pi = 0$. Like [61] we can argue that if we want to avoid large velocity perturbations, then we expect the source terms in Eq. (1.24) to cancel to a high degree. It follows that

$$\delta_{de} = a\delta_0\left[\frac{2e_\pi a^n}{3c_{\rm eff}^2} + \frac{3H_0^2\Omega_m(1+w)}{2ac_{\rm eff}^2k^2}\right] \tag{1.26}$$

$$\begin{aligned} V_{de} &= a\delta_0\left[\frac{2}{3c_{\rm eff}^2}e_\pi a^n\left\{1+3(c_{\rm eff}^2-w)+2f_\pi+n\right\}\right. \\ &\left. + \frac{3H_0^2\Omega_m\left\{3(c_{\rm eff}^2-w)+2f_\pi\right\}(1+w)}{2ac_{\rm eff}^2k^2}\right] \end{aligned} \tag{1.27}$$

where the last term in each equation is only relevant if $e_\pi = 0$. We see that during matter domination the dark energy perturbations in the sub-sound horizon regime

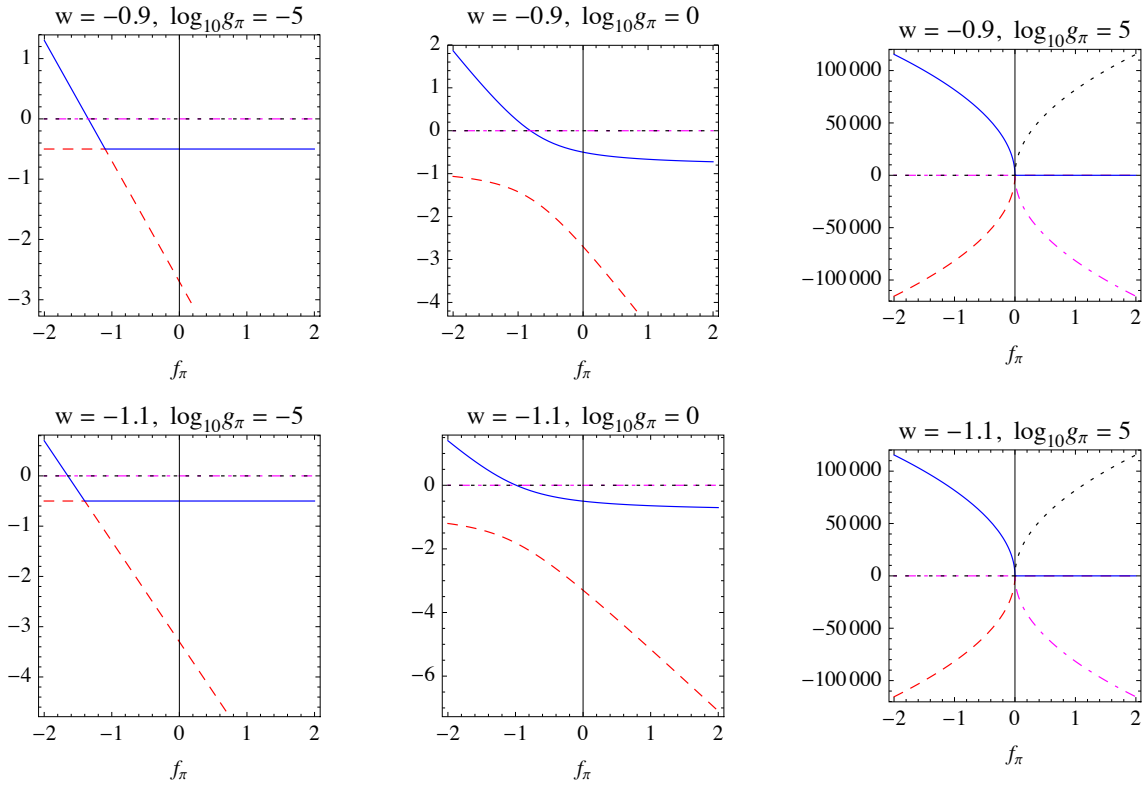

Fig. *1.1: The dark energy perturbations during matter domination in the sub-horizon but super-sound horizon regime have a power-law behaviour. Here we show the exponents of the first two terms in Eq. (1.18) for a range of values of the parameters f_π and g_π (the parameter e_π leads to an additional growing mode driven by the dark matter). Real and imaginary parts for the exponent of the first term are plotted in red dashed and magenta dot-dashed lines, respectively. For the second term the real part is plotted in blue and the imaginary part is shown in black dotted lines. Positive real parts correspond to growing modes, not necessarily instabilities.*

only grow if the coupling to Δ_m is non-zero. In that case δ_{de} is proportional to $a^n\delta_m$. If $e_\pi = 0$ then the dark energy perturbations become constant on sub-sound horizon scales in matter domination. However, it should be mentioned that we have here neglected modes that are usually decaying (as in appendix B of [61]). As mentioned at the start of the section, if $c^2_{\rm eff} < 0$ then the full solution of Eq. (1.16) grows exponentially.

Dark energy domination and $e_\pi = 0$

Considering that during dark energy domination the conformal Hubble parameter can be approximated by

$$\mathcal{H}^2 = H_0^2 \frac{\Omega_x}{a^{1+3w}}\,, \tag{1.28}$$

we find a homogeneous second order equation for the dark energy density perturbations,

$$\begin{aligned} \delta''_{de} \;+\; & \left\{ \frac{3+4f_\pi-9w}{2a} \right\} \delta'_{de} + \left\{ \frac{a^{1+3w} c_{\rm eff}^2 k^2}{a^2 H_0^2 \Omega_x} + \frac{f_\pi(2g_\pi^2-9-27w)}{3a^2} \right. \\ - \; & \left. \frac{3(c_{\rm eff}^2+\frac{2f_\pi}{3})\left[6(c_{\rm eff}^2+\frac{2f_\pi}{3})-(1+4f_\pi+3w)\right]+3(1-w)(1+3w)}{2a^2} \right\} \delta_{de} = 0\,. \end{aligned} \tag{1.29}$$

Again we can look at both super and sub-sound horizon limits for this equation.

Super-sound horizon

In the super-sound horizon limit Eq. (1.29) becomes

$$\begin{aligned} \delta''_{de} \;+\; & \left[\frac{3+4f_\pi-9w}{2a} \right] \delta'_{de} \\ + \; & \left[\frac{4f_\pi(-3+g_\pi^2-9w)+9(3w^2-2w-1)}{6a^2} \right] \delta_{de} = 0 \end{aligned} \tag{1.30}$$

which again has power-law solutions given by

$$\delta_{de} = A_3 a^{\frac{1-\alpha_3-\beta_3}{2}} + B_3 a^{\frac{1-\alpha_3+\beta_3}{2}} \tag{1.31}$$

where

$$\begin{aligned} \alpha_3 &= \frac{3+4f_\pi-9w}{2} \\ \vartheta_3 &= \frac{4f_\pi(-3+g_\pi^2-9w)+9(3w^2-2w-1)}{6} \\ \beta_3 &= \sqrt{1-2\alpha_3+\alpha_3^2-4\vartheta_3} \end{aligned} \tag{1.32}$$

We plot the behaviour of the exponents in Figure 1.2. Overall, the behaviour is similar to the one shown in Figure 1.1: For small g_π the perturbations can grow

rapidly if $f_\pi \lesssim -3$ while for large g_π they grow quickly whenever $f_\pi < 0$. For velocity and matter perturbations we have

$$\begin{aligned} V_{de} &= \frac{a^{\frac{1-\alpha_3-\beta_3}{2}}}{2}\left[B_3 a^{\beta_3}(1+6c_s^2-6w-\alpha_3+\beta_3)+A_3(1+6c_s^2-6w-\alpha_3-\beta_3)\right] \\ \delta_m &= 6(1+2f_\pi)a^{\frac{1-\alpha_3-\beta_3}{2}}\left[\frac{B_3 a^{\beta_3}}{(1-\alpha_3+\beta_3)(2-3w-\alpha_3+\beta_3)}\right. \\ &\quad \left. + \frac{A_3}{(-1+\alpha_3+\beta_3)(-2+3w+\alpha_3+\beta_3)}\right] + \delta_0 \qquad (1.33) \\ V_m &= \frac{3(1+2f_\pi)a^{\frac{1-\alpha_3-\beta_3}{2}}\left[A_3(-2+3w+\alpha_3-\beta_3)+B_3 a^{\beta_3}(-2+3w+\alpha_3+\beta_3)\right]}{(2-3w-\alpha_3+\beta_3)(-2+3w+\alpha_3+\beta_3)} \end{aligned}$$

where we have neglected a decaying mode in the matter density perturbation. We can see that the dark matter density perturbation δ_m follows the dark energy perturbations and grows at the same rate (in addition to a constant mode).

Sub-sound horizon

On the other hand, in the sub-sound horizon limit and if we assume

$$\frac{c_{\rm eff}^2 k^2}{\mathcal{H}^2} \gg \frac{f_\pi(2g_\pi^2-9-27w)}{3} - \frac{3c_s^2\left[6c_s^2-(1+4f_\pi+3w)\right]+3(1-w)(1+3w)}{2}$$

equation (1.29) reads

$$\delta_{de}'' + \left[\frac{3+4f_\pi-9w}{2a}\right]\delta_{de}' + \left[\frac{c_{\rm eff}^2 k^2}{H_0^2\Omega_x a^{1-3w}}\right]\delta_{de} = 0 \qquad (1.34)$$

and we expect to have exponential growth if $c_{\rm eff}^2 < 0$. The general solution of Eq. (1.34) is given by

$$\delta_{de} = \left(\frac{x_3}{2}\right)^{\frac{1-\alpha_4}{1+3w}}\left\{A_4\, J_{\nu_1}(x_3) + B_4\, J_{-\nu_1}(x_3)\right\} \qquad (1.35)$$

where

$$\begin{aligned} \alpha_4 &= \frac{3+4f_\pi-9w}{2} \\ \nu_1 &= \frac{\alpha_4-1}{1+3w} \\ x_3 &= \frac{2a^{\frac{1+3w}{2}}c_{\rm eff}k}{(1+3w)H_0\sqrt{\Omega_x}}\,, \qquad (1.36) \end{aligned}$$

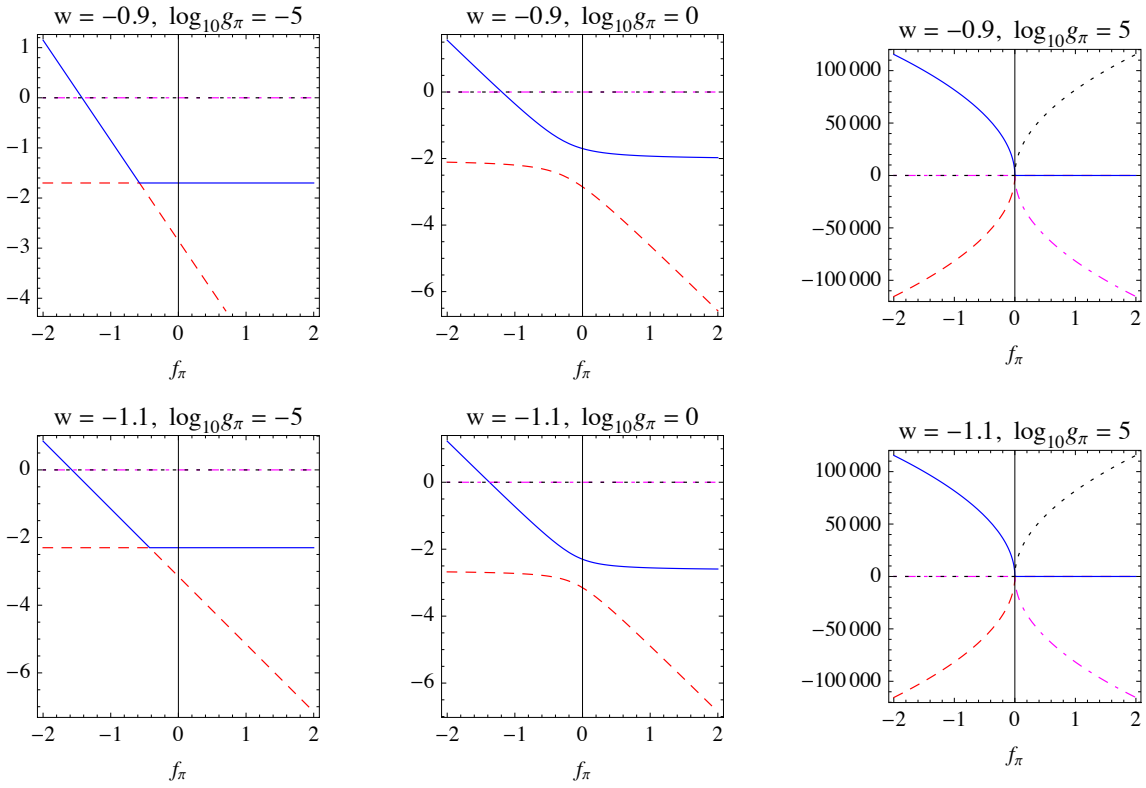

Fig. *1.2: The dark energy perturbations during dark energy domination in the sub-horizon but super-sound horizon regime have a power-law behaviour, with the exponents given here for a range of values of the parameters f_π and g_π. Here we plot the exponents of the two terms in Eq. (1.31): red dashed (real part) and magenta dot-dashed (imaginary part) lines correspond to the first term whereas blue (real part) and black dotted (imaginary part) lines correspond to the second term.*

and A_4 and B_4 are constants.[3] We see that for $c^2_{\rm eff} < 0$ the argument x_3 of the Bessel functions becomes imaginary, and indeed the perturbations will grow exponentially. Stable perturbations in this regime thus require $f_\pi < 3c_s^2/2$. We can also see that the overall pre-factor of Eq. (1.35) behaves like $a^{(1-\alpha_4)/2}$, where the exponent is linearly decreasing with f_π, i.e. the dark energy perturbations grow faster for more negative f_π. We therefore expect also a lower cutoff for f_π, around $f_\pi \approx -7$.

[3]Gamma functions, similar to those appearing in solutions in Appendix B, have been absorbed in the constants A_4 and B_4. These constants are fixed by the initial conditions.

1.3.2 Super-horizon scales

When considering super-horizon scales, $k/\mathcal{H} \ll 1$, we find that dark matter and dark energy perturbations decouple from each other again in matter and dark energy domination. However, we could only find analytical solutions during matter dominance.

Dark matter domination

Since scales larger than the horizon are also super-sound horizon scales, we can set $c_{\rm eff} = 0$ which according to Eq. (1.13) is equivalent to setting $c_s^2 = 2f_\pi/3$. Then, if we use Eq. (1.15) for the Hubble parameter and neglect decaying modes, we find the following set of solutions for matter and dark energy perturbations

$$V_m = \delta_0 a\,, \qquad \delta_m = \delta_0 \frac{3H_0^2\Omega_m}{k^2}\,, \tag{1.37}$$

$$V_{de} = \delta_0 a \left[\frac{4e_\pi a^n}{4f_\pi - 3 - 2n} + \frac{3(1+w)}{3-4f_\pi}\right]\,, \tag{1.38}$$

$$\delta_{de} = \delta_0 \frac{3H_0^2\Omega_m}{k^2}\left[\frac{4e_\pi a^n(2f_\pi - 3w)}{(4f_\pi - 3 - 2n)(2f_\pi + n - 3w)} - \frac{3(1+w)}{4f_\pi - 3}\right]\,. \tag{1.39}$$

We see that outside of the horizon the dark energy density perturbation grows like a^n – in the particular case when $n = 0$ or $e_\pi = 0$, the dark energy density perturbation (like the dark matter one) is always constant on super-horizon scales. We also notice that it is non-zero only if either the dark energy is coupled to the dark matter through $e_\pi \neq 0$ or if $w \neq -1$ [4]. We also note that we recover the solutions found in [61] in the absence of anisotropic stress.

We summarise in Table 1.1 the regions in parameter space where we expect rapid growth of the perturbations that is not compatible with the existence of a stable universe. The growth of the perturbations on sub-sound horizon scales for $c_{\rm eff}^2 < 0$ is exponential and corresponds to the usual instability for negative sound speeds. For theories with a given c_s^2 this provides an upper limit for the parameter f_π, namely $f_\pi < 3c_s^2/2$. On scales that are sub-horizon but lie above the sound horizon, the

[4] But notice that on sub-horizon scales a non-zero anisotropic stress of the dark energy itself can drive the dark energy perturbations even if $w = -1$ and $e_\pi = 0$, see Section 1.3.1. However, for our model 2 the perturbations only grow if $f_\pi < -5/4$ and only in the sub-horizon but super-sound horizon regime.

scales		rapid growth	
		matter dominance	dark energy dominance $(e_\pi = 0)$
sub-horizon	sub-sound	$c_{\rm eff}^2 < 0$	$c_{\rm eff}^2 < 0$
	super-sound	$f_\pi \ll \dfrac{9w}{2(3+2g_\pi^2)}$	$f_\pi \ll \dfrac{27w^2-18w-9}{4(3-g_\pi^2+9w)}$

Tab. *1.1: Regimes and regions in parameter space where dark energy perturbations grow rapidly.*

perturbations grow as a power law with a very high power for sufficiently negative f_π, as indicated in the table.[5] This provides a lower limit for f_π as such a rapid growth of the dark energy is again not compatible with the data.

In the next section we are going to vary $c_{\rm eff} > 0$ and f_π independently, so that c_s^2 can take any value. For this reason we will not see the upper cutoff on f_π from the instability arising due to $c_{\rm eff}^2 < 0$, as we never enter in this regime, but we will see the lower cutoff. Also, as in the approximate solutions shown in Figure 1.3, we will limit ourselves to $n = 0$ for the model 1 defined by Eq. (1.9).

1.4 Observational constraints

In this section, we investigate the parameter degeneracies and the constraints on the anisotropic stress models for dark energy imposed by different cosmological observations. We use a modified version of the `CosmoMC` code (version Mar 13 [62, 63]) to perform Markov-chain Monte-Carlo (MCMC) explorations of the model likelihoods. The sampler calls a modified version of the `CAMB` code[6] (version Mar 13 [64, 65]) to

[5]The regions in the table correspond to the sub and super-sound horizon limits of the second order Eqs. (1.16) and (1.29). Note that according to the general solution for matter dominance and sub-horizon scales, Eq. (B.1), there is also exponential growth on super-sound horizon scales for $c_{\rm eff}^2 < 0$.

[6]The modified codes are available at http://cosmology.unige.ch/content/cosmomc-and-camb-early-dark-energy-and-anisotropic-stress and the chains (1.4 GB) can be downloaded from http://theory.physics.unige.ch/∼kunz/traces-anisotropic-dark-energy/ade_chains.tar.gz.

compute the linear theory CMB spectra for a given model. In all cases we use constraints on the number of relativistic degrees of freedom at Big-Bang nucleosynthesis (BBN) [66] and put a prior on the age of the Universe to be between 10 and 20 Gyrs. In addition we use the CMB likelihood code of the Planck collaboration (version 1.0 [67, 68]) which includes the Planck first data release combined with WMAP 9yr low-multipole polarisation data [69]. Moreover, we add the high-multipole temperature data from the South Pole Telescope (SPT) [70] and the Atacama Cosmology Telescope (ACT) [71]. In the following, we use the abbreviation *CMB data* for the combination of Planck temperature, WMAP9 low-multipole polarisation, and ACT and SPT temperature (referred to as *Planck*+WP+highL in the Planck papers). We expect the CMB data to provide constraints not only on the parameters that describe the primordial power spectrum and the re-ionisation history but also to mildly constrain the late-time evolution of the gravitational potentials through the integrate Sachs-Wolfe effect and CMB lensing.

To further constrain the parameters that are relevant for the late-time evolution of the background geometry, the density parameter and equation of state of dark energy, we also use constraints on the distance–redshift relation from baryon acoustic oscillations (BAO) and type Ia supernovae (SNe Ia). Currently, there are seven BAO measurements available: two from the Sloan Digital Sky Survey (SDSS) DR7 [72, 73], one from the 6dF Galaxy Survey [74], three from the WiggleZ Dark Energy Survey [75], and one from the SDSS-III Baryon Oscillation Spectroscopic Survey (BOSS) DR9 [76]. In case of the supernovae, we use the compilation of 473 SNe Ia provided by the SuperNova Legacy Survey (SNLS) team [77]. The fact that Planck prefers a slightly different value for H_0 than local measurements of the Hubble parameter in a flat ΛCDM cosmology raises concerns about the compatibility of these data sets [68]. For this reason we chose not to include constraints on the local expansion rate. If we included the H_0 constraint of [78] we would find that the confidence intervals for w are shifted slightly towards more negative values, with $w = -1$ sitting close to the 2σ limit. On the other hand, we would not find significant changes in the constraints on the parameters that govern the dark energy perturbations when including H_0 data.

Using large-scale structure data like the galaxy power spectrum $P(k)$ correctly in the context of dark energy and modified gravity models is quite involved. There are hidden model assumptions in the analysis of the data and the construction of the likelihood. For example, the background cosmology is used when converting angles and redshifts to k vectors. Moreover, the impact of modifications of gravity on galaxy bias and non-linear clustering is mostly unknown. For these reasons we

limit ourselves for the time being to the data sets mentioned above.

For the parameter estimation we vary a base set of seven parameters (those of the flat wCDM model). These are the amplitude, $\ln[10^{10} A_s]$, and the tilt, n_s, of the spectrum of primordial scalar curvature perturbations (modelled as a power law normalised at $k = 0.05\,\mathrm{Mpc}^{-1}$), the reionisation optical depth, τ, the physical baryon and cold dark matter energy fractions, $\Omega_b h^2$ and $\Omega_c h^2$, 100 times the ratio of the sound horizon to the angular diameter distance to the last-scattering surface, θ, and finally the constant equation of state parameter of dark energy, w. In the figures we will replace the "fundamental" parameters A_s and θ by the variance of fluctuations in spheres of 8 Mpc today, σ_8, and the value of the Hubble parameter today, H_0 (in units of km/s/Mpc), that are both derived parameters.

In addition to the base model, we vary or fix the values of the parameters that describe the properties of the dark energy perturbations: the effective sound speed, $\log_{10} c^2_{\mathrm{eff}}$, the external anisotropic stress parameter, e_π, and the internal anisotropic stress parameter, f_π, with its transition scale, $\log_{10} g_\pi$. We use flat priors for all parameters, set adiabatic initial conditions for the evolution of the cosmological perturbations, and ignore vector and tensor modes for simplicity.

Let us first take a look at the effect of the different data sets on the parameter constraints. In Figure 1.4 we show the marginalised posteriors and the marginalised 2d-likelihood contours of a parameter subset in the full model, i.e. varying all dark energy parameters including the anisotropic stress model, e_π, f_π, g_π (for $n = 0$). We compare the effect of adding more data: blue is *CMB data* only, red is *CMB+BAO*, and black and the likelihood density plots are *CMB+BAO+SNe*. For parameters that are not related to dark energy anisotropic stress the likelihood contours shrink considerably when adding the low-redshift data, as they contain much information on the late-time expansion and therefore on w. The constraints on the anisotropic stress parameters are not much altered by adding low-redshift data because BAO and SNe do not contain information on the growth of structure that is affected by the dark energy clustering. To improve those constraints we would need to add information on galaxy clustering, redshift space distortions and cosmic shear.

The (f_π, $\log_{10} g_\pi$) plane also shows nicely the lower limit on f_π from the rapid growth of perturbations. As argued in the discussions of the sub horizon / super-sound horizon perturbation evolution in section 1.3.1 and shown in Figs. 1.1 and 1.2, a very negative value of f_π is in conflict with observations as the dark energy perturbations become large. We can also see how the lower limit on f_π changes as a function of g_π, with $g_\pi \gg 1$ requiring $f_\pi > 0$.

It is interesting to note that the marginalised likelihood in the $(\log_{10} c^2_{\rm eff},\, f_\pi)$ plane peaks where f_π is negative and $\log_{10} c^2_{\rm eff}$ close to 0, while the $(f_\pi,\, \log_{10} g_\pi)$ plane shows that the likelihood for negative f_π is much lower than for positive f_π. Note that this is a volume effect of the marginalization. If we were to fix $c_{\rm eff} = 1$, then the high plateau of the likelihood in the $(f_\pi,\, \log_{10} g_\pi)$ plane would shift from the positive–positive to the negative–negative quadrant, and the situation would be quite different.

Thus, if we had additional observables that even more strongly prefer $c_{\rm eff} = 1$, we would conclude $f_\pi \leq 0$. The constraints on e_π would not be affected as it is virtually not degenerate with $\log_{10} c^2_{\rm eff}$. There is a hint that this could actually be the case: the CFHTLens weak lensing survey [79] as well as the Planck cluster counts [80] prefer σ_8 and Ω_m considerably lower than Planck alone (in the ΛCDM model). We added a toy constraint on the combination $\sigma_8(\Omega_m/0.27)^{0.6}$ that reflects the weak lensing and cluster counts, and noticed that it is passed through the parameter degeneracies in such a way that it constrains $c^2_{\rm eff} \sim 1$ and f_π and $\log_{10} g_\pi$ both negative. In this case f_π turns out to be strongly constrained and $f_\pi = 0$ is already in quite some tension with the toy data. We interpret this as a hint that additional dark energy degrees of freedom are able to reconcile apparent tensions between different current data sets. However, we emphasise that the analysis of the weak lensing and cluster count likelihood needs to be done fully correctly within the framework of a generalised dark energy model like ours, and the constraints quoted in the literature [79, 80] cannot directly be implemented since they are derived for the ΛCDM model.

Next, let us study the anisotropic stress model parameters. In Figure 1.5 we show the marginalised posteriors and 2d-likelihoods using the full data set, *CMB+BAO+SNe*. We compare the different models: for green we fix $(e_\pi,\, f_\pi,\, \log_{10} g_\pi) = (0, 0, 0)$, for blue we fix $(f_\pi,\, \log_{10} g_\pi,\, \log_{10} c^2_{\rm eff}) = (0, 0, 0)$, for red we fix $(f_\pi,\, \log_{10} g_\pi) = (0, 0)$, and for black and the likelihood density plots we vary all parameters. We observe that in case of no anisotropic stress, green, the dark energy sound speed is only very mildly preferred to be close to 1, as expected from earlier studies, see e.g. [81, 82]. Finally, in Figure 1.6 we show the marginalised posteriors for the remaining six base parameters, $\{\Omega_b h^2,\, \Omega_c h^2,\, n_s,\, \tau,\, \sigma_8,\, H_0\}$, that are not directly related to dark energy. We note that all models with dark energy anisotropic stress slightly prefer a higher σ_8 than in the smooth dark energy case, $c_{\rm eff} = c_s = 1$ (see [83] for a study of the impact of w on σ_8 in smooth dark energy models). This is compatible with the discussion above on the slight tension between constraints on σ_8 from Planck CMB and Planck cluster counts as well as weak lensing.

1.5 Modified growth parametrisations

In this project we used prescriptions for the 'hydrodynamical' closure relations that define δP and π in terms of other variables, in order to complete the system of equations. Instead of defining the dark energy momentum tensor, it is also possible to introduce functions that describe the change to the matter growth rate [85, 86] or that modify the Einstein equations with an effective Newton's constant and a gravitational slip [43]. The latter parametrisation is in principle equivalent to giving δP and π as shown explicitly in [53], but the modified growth rate on its own is not sufficient and needs to be supplemented by an additional condition. We will call these approaches 'modified growth' parameterisations, see also section 1.3.2 of [36] for a more detailed introduction.

As the modified growth approach is quite popular and since several groups have derived predictions for the accuracy with which these parameters can be measured (e.g. [43, 87, 88]), we give here the expressions necessary to compute these quantities in general and discuss the links between them and our parametrisation. We then show what bounds we can infer on these modified growth parameters from the data that we use, in the context of our model.

1.5.1 Definition of the modified growth parameters

In general the presence of a dark energy fluid or of a modification of General Relativity will affect the growth rate of the dark matter perturbations. We define the growth factor g as the logarithmic derivative of the comoving matter density perturbation,

$$g \equiv \frac{d\log\Delta_m}{d\log a} \tag{1.40}$$

The growth factor is often approximated using the growth index, γ, as

$$g = \Omega_m(a)^\gamma \tag{1.41}$$

where $\Omega_m(a) \equiv 8\pi G a^2\rho_m(a)/(3\,\mathcal{H}^2)$. In general, g and γ are space and time dependent functions. To investigate γ we express it in terms of g

$$\gamma = \frac{\log g}{\log\Omega_m(a)} \tag{1.42}$$

and we have implemented these expressions in CAMB so that we can obtain limits on g and γ as derived parameters from our MCMC chains.

However, in general we have two scalar degrees of freedom, related to the possibility to choose independent closure relations for both δP_{de} and π_{de} in the fluid picture. To model these two degrees of freedom, we introduce a parameter Q which describes either an effective Newton's constant QG or an additional contribution to the clustering from Δ_{de} through the Poisson equation for ϕ. In addition, we parameterise the gravitational slip (the difference of the gravitational potentials which is in our model due to the anisotropic stress of the dark energy) as η,

$$Q \equiv \frac{-k^2\phi}{4\pi G a^2 \rho_m \Delta_m} = 1 + \frac{\rho_{de}\Delta_{de}}{\rho_m \Delta_m}\,, \qquad \eta \equiv \frac{\phi}{\psi}\,. \tag{1.43}$$

η should not be confused with conformal time, obviously. This parameter is occasionally called ϖ in the literature.

We can now derive some relations between different parameters. For example we have that

$$\frac{1}{\eta} = 1 + \frac{2}{Q}\frac{\rho_{de}\pi_{de}}{\rho_m\Delta_m} = 1 + \frac{2\rho_{de}\pi_{de}}{\rho_m\Delta_m + \rho_{de}\Delta_{de}}\,. \tag{1.44}$$

In a pure model 1 situation, i.e. with $f_\pi = 0$, we then have that

$$\frac{1}{\eta} = 1 + \frac{2e_\pi}{Q}\frac{\rho_{de}}{\rho_m} = 1 + \frac{2e_\pi}{Q}\frac{\Omega_{de}}{\Omega_m}a^{-3w} \approx 1 + \frac{2e_\pi}{Q}\,, \tag{1.45}$$

where the final expression is valid at late times for our averaging (see below).

1.5.2 Constraints on the modified growth parameters in our model

In general the modified growth parameters are functions of scale and time. We limit here our investigation to the late-time behaviour, by averaging the parameters over the range $z = 0 \ldots 1$ using 10 values linearly spaced in z. The scale dependence can be important, so we consider separately 'large' scales, $k = 10^{-3}\,h\,\mathrm{Mpc}^{-1}$ and 'small' scales, $k = 10^{-1}\,h\,\mathrm{Mpc}^{-1}$.

In Figure 1.8 we show Q and η values of a sample of 'type 1' models accepted by the MCMC algorithm where e_π varies and f_π is zero. In the first column we also fix

$c_s = 1$ (which is equivalent to $c_{\rm eff} = 1$ as $f_\pi = 0$), and in this case we can access only a narrow region in (Q, η) space. This is not unexpected as in general we need to vary both δP_{de} and π_{de}. When doing so in the second and third column, and now a much larger part of the (Q, η) parameter space is accessible. This also illustrates that our models are able to probe quite generally the space of modifications of the growth parameters.

We can also see very nicely from the colours in the first two columns of Figure 1.8 how a non-zero e_π changes the growth rate γ, with pretty much a one-to-one mapping between the two on small scales. The sound speed on the other hand leads to a rotation in the (Q, η) parameter space on small scales.

We can understand this latter behaviour with the help of the relation (1.45): The presence of an anisotropic stress induced by e_π impacts not only η, but also Q. On sub-sound-horizon scales and during matter domination the induced dark energy perturbations are given by Eq. (1.26),

$$\Delta_{de} \approx \delta_{de} \approx a\delta_0 \left(\frac{2e_\pi a^n}{3c_{\rm eff}^2}\right) \approx \left(\frac{2e_\pi a^n}{3c_{\rm eff}^2}\right) \Delta_m \,, \tag{1.46}$$

and therefore we have in that limit that

$$Q = 1 + \frac{2e_\pi a^n}{3c_{\rm eff}^2}\frac{\rho_{de}}{\rho_m} \;\Rightarrow\; \frac{1}{\eta} = 1 + \frac{6c_{\rm eff}^2 e_\pi a^n \rho_{de}}{2e_\pi a^n \rho_{de} + 3c_{\rm eff}^2 \rho_m} \,. \tag{1.47}$$

For high sound speed, $c_s \approx 1$, we find from the MCMC exploration that at 95% CL $-0.01 < e_\pi < 0.18$, and the allowed region shrinks around $e_\pi = 0$ as the sound speed decreases, see the red contours in Figure 1.5. Plotting the curves $Q(e_\pi; c_{\rm eff})$ and $\eta(e_\pi; c_{\rm eff})$ for the allowed values of e_π leads to a figure that corresponds very well to the region visible in the upper row of Figure 1.8. We notice that for $e_\pi = 0$ we have that $Q = 1$ and $\eta = 1$ independently of the sound speed. This behaviour is clearly visible in the figure. We can also see that as $c_{\rm eff} \to 0$ the slip vanishes, $\eta \to 1$, even if $e_\pi \neq 0$, while the impact of e_π on Q is enhanced, explaining the horizontal line visible in the top right-hand panel of Figure 1.8 for low sound speed.

On large scales, the impact of $c_{\rm eff}$ is more indirect, by changing the size of the sound horizon. We can see that for a lower effective sound speed we have a larger Q for a given η, as the dark energy is able to cluster more easily. On super-sound (but sub-horizon) scales and during matter dominance, dark energy density perturbations

are given by (Eq. (1.18))

$$\Delta_{de} \approx \frac{2e_\pi a^n \Delta_m}{3\left[2\left(1+\alpha\right)+\vartheta+n(3+\alpha+n)\right]}\frac{k^2}{\mathcal{H}^2} \tag{1.48}$$

$$Q = 1+\frac{2e_\pi a^n}{3}\frac{\rho_{de}}{\rho_m}\frac{k^2}{\mathcal{H}^2} \tag{1.49}$$

$$\frac{1}{\eta} = 1+\frac{6e_\pi a^n \rho_{de}}{3\rho_m + 2e_\pi a^n \rho_{de}\frac{k^2}{\mathcal{H}^2}\left[2\left(1+\alpha\right)+\vartheta+n(3+\alpha+n)\right]^{-1}}\,. \tag{1.50}$$

On the other hand, if we consider solutions on super-horizon scales, that is, Eq. (1.37)-(1.38), we have

$$\Delta_{de} \approx \Delta_m \left[\frac{4e_\pi a^n - 3(1+w)}{-3}\right], \tag{1.51}$$

$$\begin{aligned} Q &= 1+\left[-\frac{4}{3}e_\pi a^n + (1+w)\right]\frac{\rho_{de}}{\rho_m} \\ \Rightarrow \quad \frac{1}{\eta} &= 1+\frac{6e_\pi a^n \rho_{de}}{3\rho_m - \left[4e_\pi a^n - 3(1+w)\right]\rho_{de}} \end{aligned} \tag{1.52}$$

The last equation shows that on horizon scales dark energy can cluster even if $e_\pi = 0$. This is the reason why there is no 'clean' intersection of the curves at $Q = 1$, $\eta = 1$ in the lower row of Figure 1.8.

1.6 Conclusions

In this paper we study effective fluid dark energy models that have a non-zero anisotropic stress π_{de}. These models can represent not only dark energy, but also modified gravity models [47]. We consider specifically two scenarios, one where the dark energy anisotropic stress is linked to the dark matter density perturbations by a parameter e_π, and another model where π_{de} is linked to the dark energy density perturbations by a parameter f_π. These are only two out of a range of possibilities that arise naturally in general models like the Horndeski Lagrangian, but we think that they illustrate rather well the impact of a non-zero anisotropic stress that is either internal to the dark energy (model 2) or externally sourced (model 1). In addition we allow for a free sound speed c_s for the dark energy perturbations.

When studying the evolution of the perturbations, we find that the internal anisotropic stress changes the effective sound speed of the dark energy, see Eq. (1.13). This means that the anisotropic stress can stabilise the dark energy perturbations even if $c_s^2 < 0$, but also that $c_s^2 > 0$ does not guarantee stability, as the relevant quantity is $c_{\text{eff}}^2 = c_s^2 - 2f_\pi/3$. We also find that a sufficiently negative π_{de} (relative to Δ_{de}) can lead to rapid growth of the dark energy perturbations in the regime that is sub-horizon but outside of the sound horizon (cf Table 1.1).

We further find that the contribution to π_{de} from Δ_m acts like an external source of dark energy perturbations. This coupling can lead to growing perturbations both inside the dark energy sound horizon and outside of the Hubble horizon, at least as long as the dark matter is dominating the evolution of the universe. With the purely 'internal' anisotropic stress of our model 2 (where $\pi_{de} \sim \Delta_{de}$) this does not happen. If the coupling to the matter perturbations is zero, then the dark energy perturbations become constant on sub-sound horizon or super-Hubble horizon scales during matter domination, even in the presence of an internal π_{de} (except when the effective sound speed of the dark energy becomes imaginary).

For all of these special cases we provide analytical approximations for the behaviour of the dark energy perturbations. On the one hand, these are useful to understand the behaviour of the dark energy and the resulting observational constraints, and on the other hand, they can be used to correctly set initial conditions for numerical codes.

When looking at the constraints from the cosmic microwave background, augmented by distance data from BAO and SN-Ia, we find that the external contribution to π_{de} is quite well constrained, $-0.01 < e_\pi < 0.13$ at 95% CL for $f_\pi = 0$ (marginalised over $\log(c_{\text{eff}})$), and $-0.01 < e_\pi < 0.23$ when also marginalising over f_π and g_π, see Figure 1.5. The internal contribution is much less constrained, and is limited mostly by the stability of the perturbations. We also considered the resulting constraints on the 'modified growth' parameters like the growth index γ, the effective Newton's constant Q and the gravitational slip η, shown in Figure 1.8.

Overall, adding anisotropic stress to dark energy models (effectively turning them into modified gravity models [48]) opens up a new region of parameter space that is poorly constrained by the primary CMB anisotropies alone. Constraining these models requires additional data that probes the evolution of the perturbations, like weak lensing observations, redshift space distortions, the galaxy distribution and the growth rate of structure. Currently ongoing and future experiments will provide a wealth of data to improve our understanding of the dark energy, but it is important

that the data sets are analysed carefully and consistently by taking into account the full cosmological model, without assuming ΛCDM or smooth dark energy from the beginning.

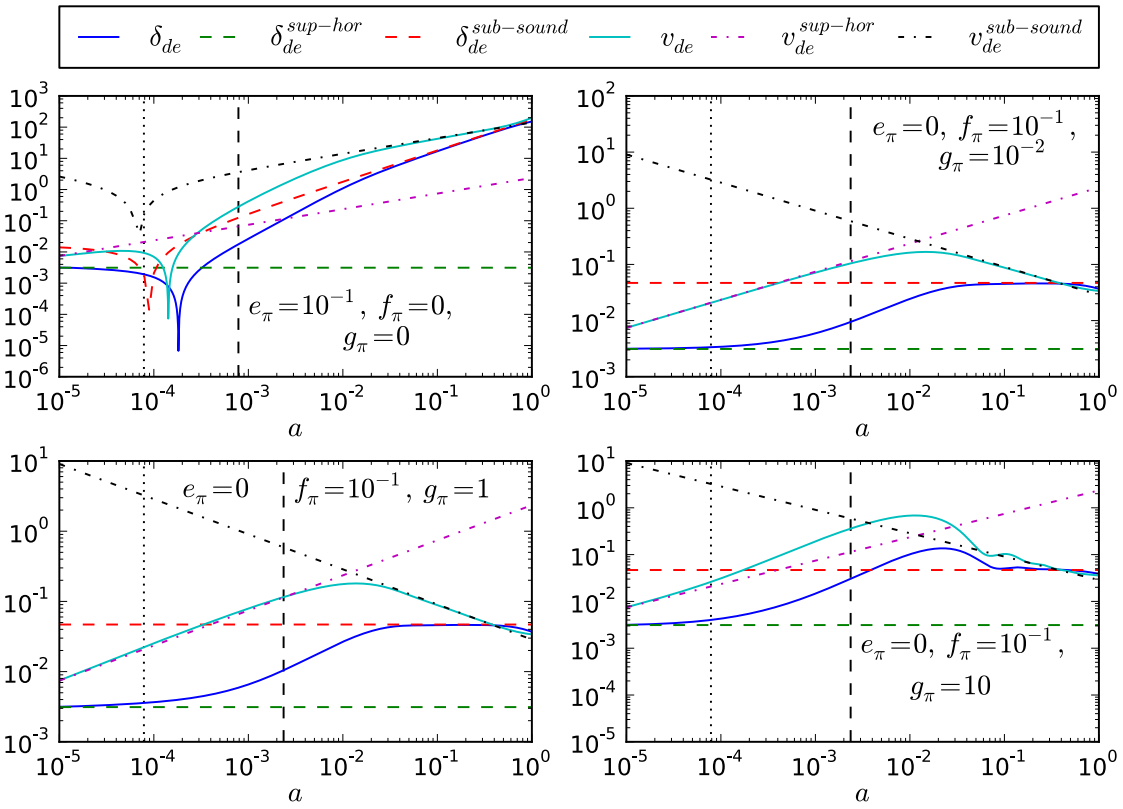

Fig. *1.3: The figure shows the behaviour of the variables δ_{de} and v_{de} for $k = 1.5 \times 10^{-2}$, $c_s^2 = 10^{-1}$, $w = -1.05$, $n = 0$ (the power in Eq. (1.9)) and different combinations of parameters e_π, f_π and g_π. The blue and cyan curves are the numerical solutions. Green dashed and magenta dot-dashed curves are analytical solutions on super horizon scales, Eqs. (1.38)-(1.39). On the other hand, the red dashed and black dot-dashed curves are analytical solutions on sub-sound horizon scales given by Eqs. (1.26)-(1.27). The vertical lines give the scale factor at which the mode enters the effective sound horizon (dashed line) and the Hubble horizon (dotted line). We consider a longer dynamic range in a to illustrate the transition from super-horizon to sub-sound horizon scales more clearly, without however including radiation in the numerical solution.*

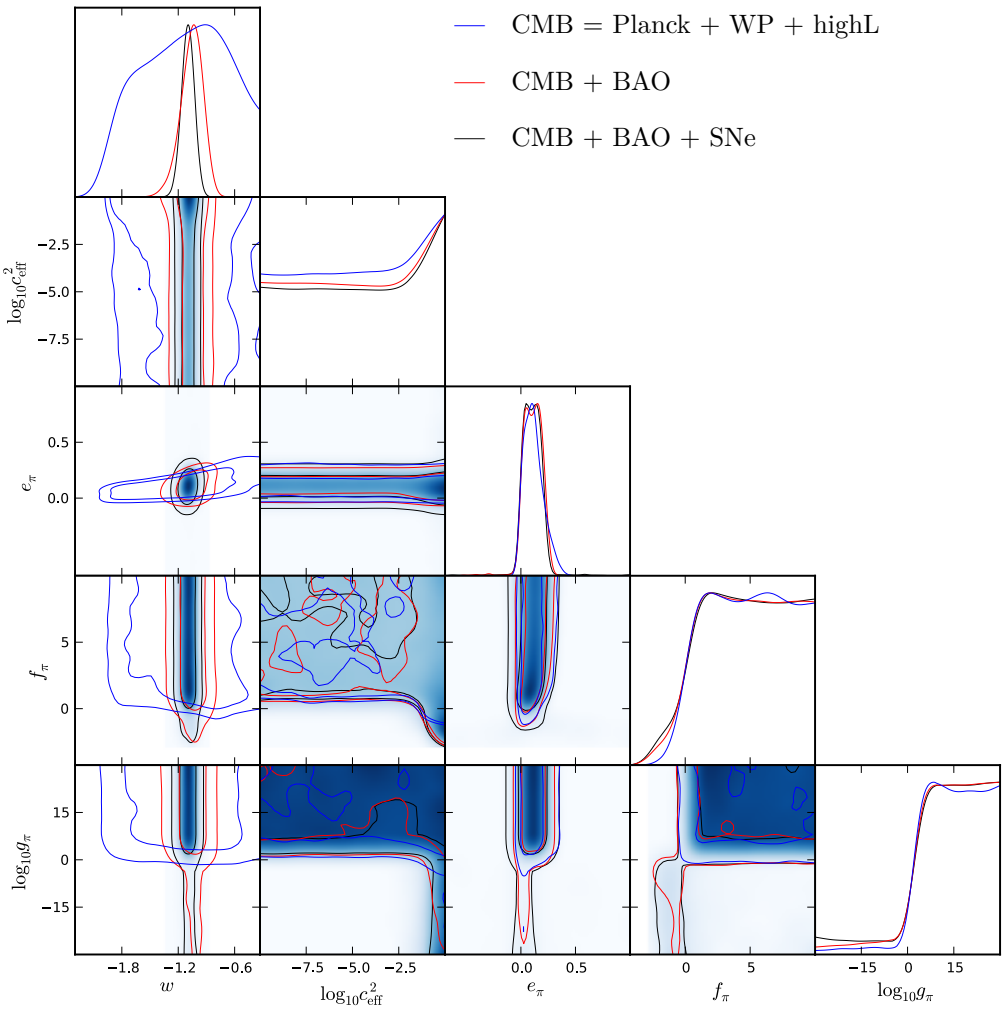

Fig. *1.4: Marginalised 2d likelihoods and 1- and 2-σ contours of combinations of the model parameters $\{w,\, e_\pi,\, f_\pi,\, \log_{10} g_\pi,\, \log_{10} c^2_{\rm eff}\}$. We compare the use of different data sets: blue is* CMB data *only, red is* CMB+BAO*, and black and the likelihood density plots are* CMB+BAO+SNe*. In all cases we vary all parameters.*

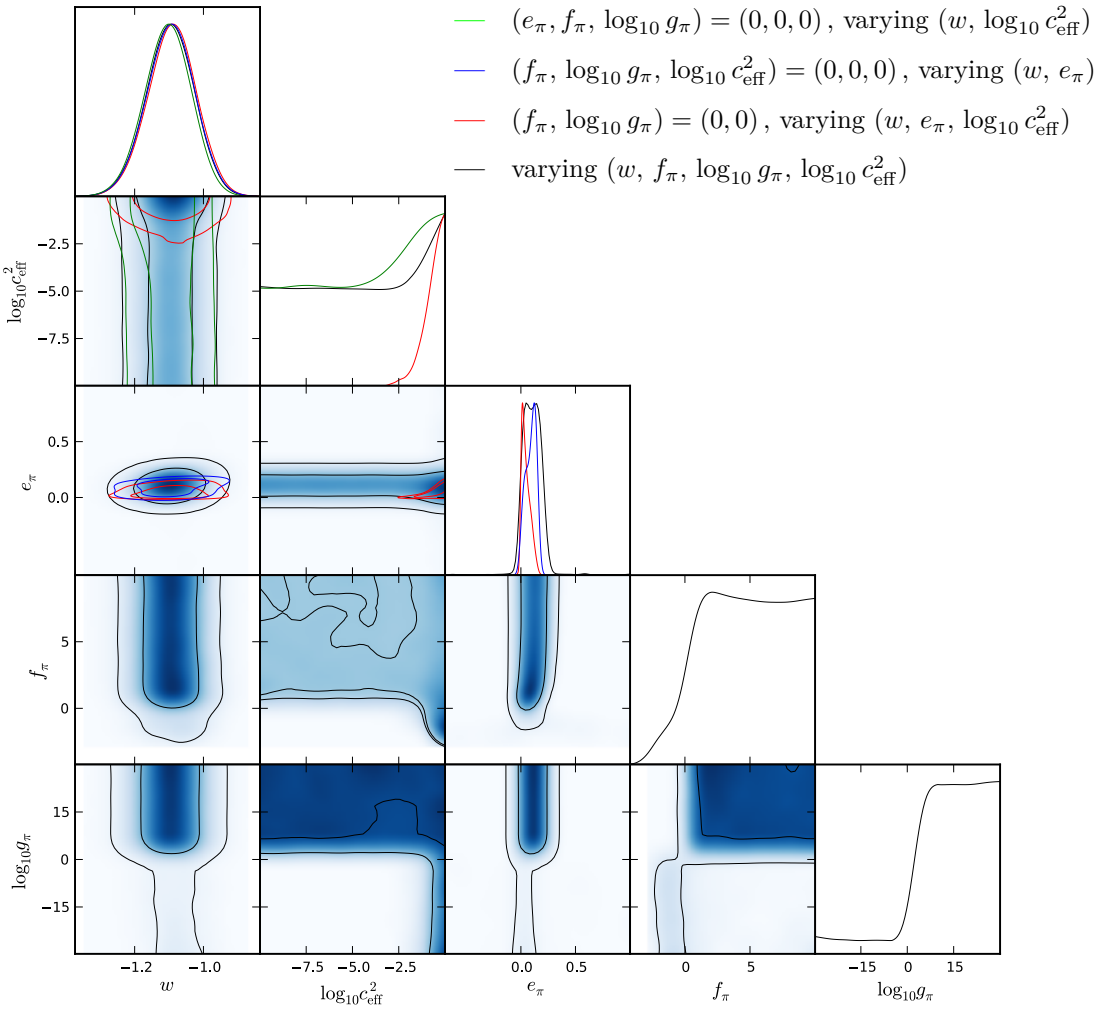

Fig. *1.5: Marginalised 2d likelihoods and 1- and 2-σ contours of combinations of the model parameters $\{n_s, \sigma_8, w, e_\pi, f_\pi, \log_{10} g_\pi, \log_{10} c^2_{\rm eff}\}$. We compare the different models: for blue we fix $(f_\pi, \log_{10} g_\pi, \log_{10} c^2_{\rm eff}) = (0, 0, 0)$, for red we fix $(f_\pi, \log_{10} g_\pi) = (0, 0)$, and for black and the likelihood density plots we vary all parameters (except for the scaling exponent n of model 1 which is always set to $n = 0$). Here we are using the full data set,* CMB+BAO+SNe.

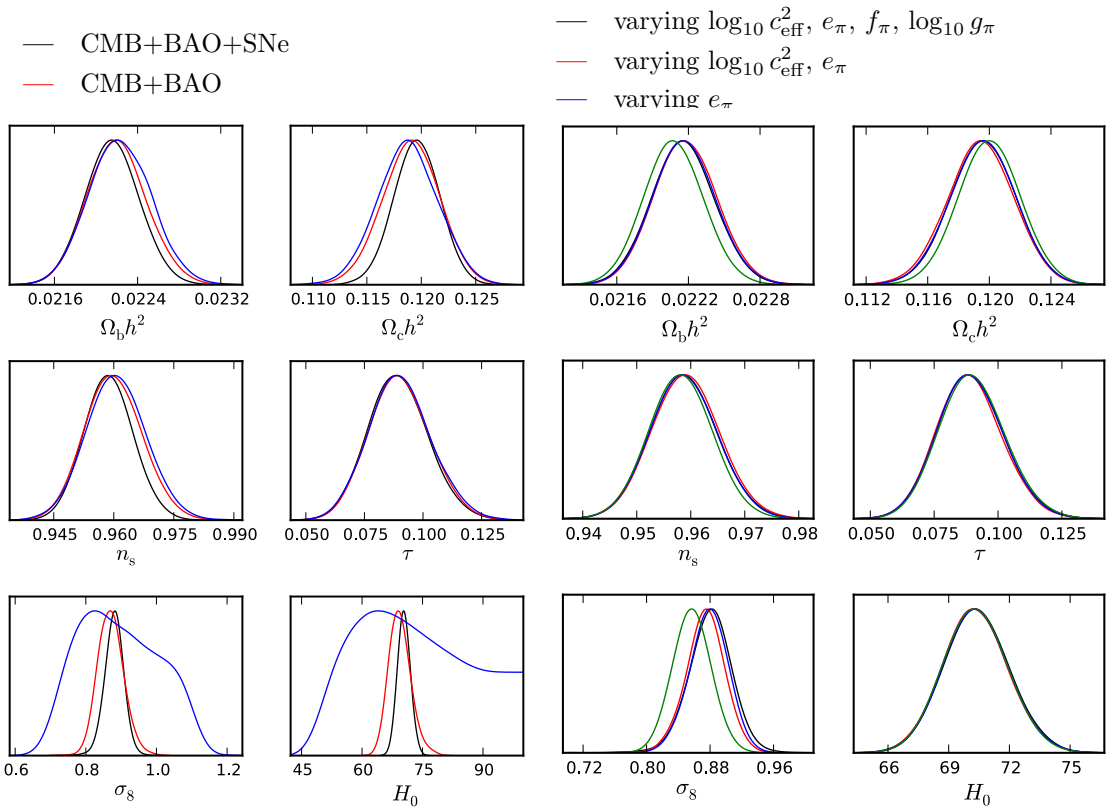

Fig. *1.6: Marginalised posteriors of those model parameters not directly related to dark energy* $\{\Omega_b h^2, \Omega_c h^2, n_s, \tau, \sigma_8, H_0\}$. Left panel*: comparison of different data sets as in Figure 1.4. The addition of background data sets helps to constrain especially* H_0 *and* σ_8. Right panel*: comparison of different models as in Figure 1.5. The constraints on these parameters do not change significantly when the anisotropic stress is non-zero, with the exception of* σ_8 *which prefers a slightly higher value.*

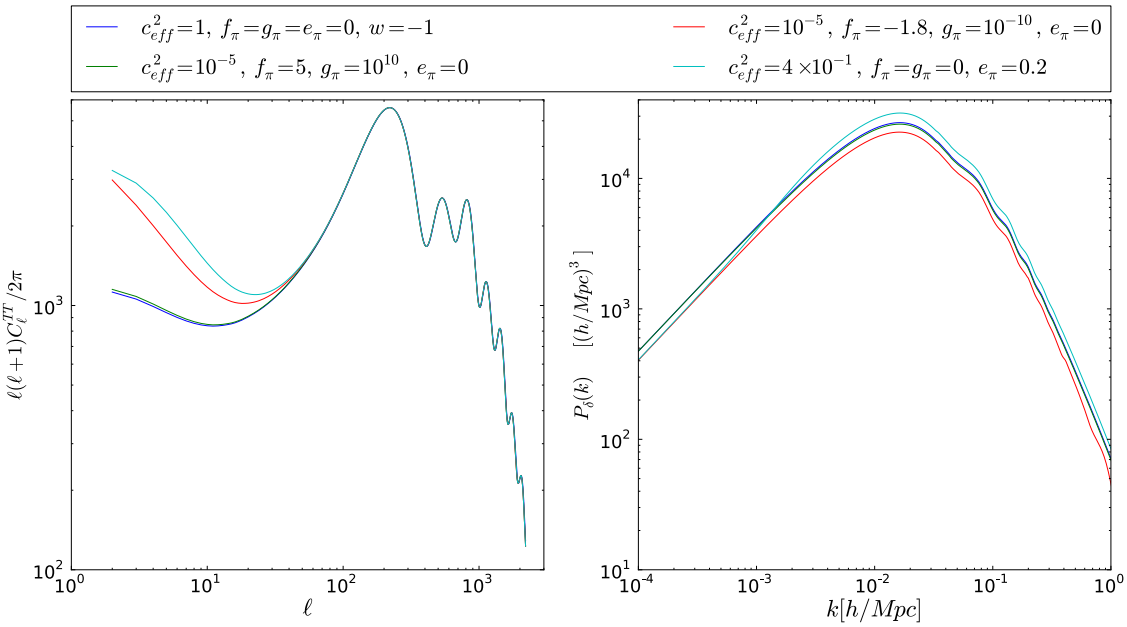

Fig. *1.7: CMB angular power spectra (left panel) and matter power spectra (right panel). The concordance model is shown in blue. In green we plot a model with internally sourced anisotropic stress whose parameters are allowed by the cosmological constraints. Two models with parameters excluded by cosmological constraints are depicted in red (internally sourced anisotropic stress) and cyan (externally sourced anisotropic stress). For those models different from the concordance model we used $w = -0.95$. In the CMB the differences appear on large scales as the ISW effect is strongly affected by the late-time anisotropic stress of the dark energy. The impact on the matter $P(k)$ is less strong and on scales smaller than the peak appears mostly as a shift in the normalisation (and thus a shift in σ_8), although this is different on large scales (that are however difficult to observe in galaxy surveys). The effect looks degenerate with an early dark energy contribution (see e.g. Figure 5 of [84]) and it may also be difficult to distinguish observationally from galaxy bias.*

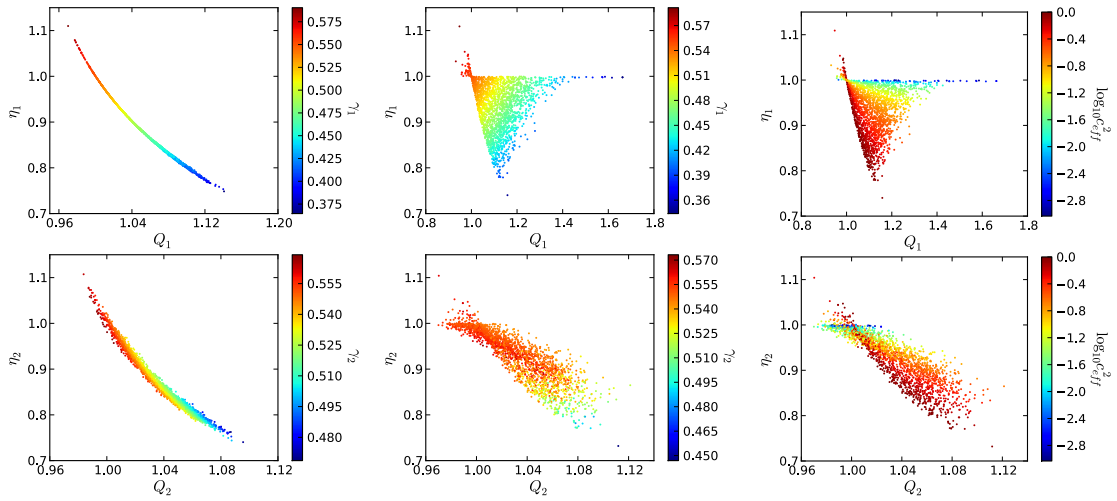

Fig. *1.8: Scatter plots of samples of accepted models in our MCMC chains for $f_\pi = 0$ and e_π varying, when using the full data set,* CMB+BAO+SNe. *The lower row of figures shows the behaviour on large scales ($k_1 = 10^{-3}\,h\,\mathrm{Mpc}^{-1}$), while the upper row depicts smaller scales ($k_2 = 10^{-1}\,h\,\mathrm{Mpc}^{-1}$).* First column: *the sound speed is held fixed, $c_s = 1$, and the growth index, γ, nicely parametrises the single allowed line in the (Q, η) plane.* Second column: *the sound speed is allowed to vary, a whole area is sampled in the (Q, η) plane, and the growth index only parametrises one direction.* Third column: *the other direction is parametrised by the sound speed.*

Chapter 2

Lensing convergence and neutrino mass in galaxy surveys

2.1 Introduction

Measurements of the Cosmic Microwave Background (CMB) anisotropies over the past three decades represent a remarkable achievement in cosmology [18–20]. Constant increases in both amount and quality of data not only have allowed more rigorous tests of cosmological models, but also have required the improvement of both the tools and methods we use for the analysis of those data sets. This progress has turned out in a phenomenological model of the universe which fits reasonably well most of the available observations [21].

Although the ΛCDM model is relatively successful at explaining the current observations, most of the underlying physics in the model remains unknown (e.g., dark energy, dark matter). In particular, the unknown Cold Dark Matter (CDM) constitutes about 30% of the energy content in the universe. Searches for dark matter particles have come out with no conclusive results, leaving neutrinos as the only known dark matter candidate. Neutrino experiments have shown that neutrinos are massive particles, but have been unable to provide an absolute scale for their masses [89, 90].

Since massive neutrinos change the background evolution of the universe, CMB measurements can be utilised to constraint their masses. When the neutrino mass is small ($\approx 0.1\, eV$) neutrinos have a modest signature on the CMB angular power spectrum

and those constraints can provide only an upper limit for the neutrino mass. Degeneracies with other parameters in the cosmological model (e.g., the equation of state of dark energy w or the Hubble parameter H_0) help to further degrade constraints on the neutrino mass from CMB data.

By mapping the distribution of matter in the universe one can also test cosmological models. Galaxy surveys, probing the low red-shift universe, allow to break parameter degeneracies hence improving the constraints on the neutrino masses [91]. Massive neutrinos would suppress the clustering of galaxies at small scales thus damping the matter power spectrum $P(k)$ on those scales. It is expected that future galaxy surveys will be able to measure this suppression and therefore determine the absolute mass of the neutrinos.

Future galaxy surveys will probe distance scales comparable to the Hubble horizon (a few tens of $\mathrm{Gpc}^3/\mathrm{h}^3$) thus allowing more rigorous analysis. Non-linearities and relativistic effects such as red-shift space distortions and lensing convergence should then be consistently included in galaxy clustering analyses if the constraining power of the survey is not to be wasted. This chapter aims at showing the importance of the inclusion of lensing convergence in galaxy clustering analyses. In particular, we show that if future analyses neglected the lensing convergence, measurements of the neutrino masses would be severely biased thus throwing away valuable information and leading to misleading conclusions about the cosmological model.

The plan of the chapter is as follows. In the next Section we recall how galaxy number counts are modelled. Our methodology is explained in Section 2.3. Then in Section 2.4 we show and discuss our results. Finally, we give our conclusions in Section 2.5.

2.2 Galaxy number counts angular power spectrum

Although galaxy red-shift surveys measure red-shift z and direction $\mathbf{n}$ of sources in the sky, analyses of galaxy clustering data are commonly done by using the matter power spectrum $P(k, z)$ [92] which is not an observable. An alternative approach uses the angular matter power spectrum $C_\ell(z, z')$ which is an observable. It has been shown in [93] that for galaxy catalogues with photometric red-shifts, an analysis of the $C_\ell(z, z')$ spectra can perform significantly better than one using $P(k, z)$. This is due to both an optimal use of red-shift information and the not averaging over

directions in the $C_\ell(z, z')$ approach. It is therefore more suitable to work with the angular matter power spectrum and we have chosen to do so in this project.

Galaxy number counts for a survey with limiting magnitude $m_{\rm lim}$ is given by

$$n(z, \mathbf{n};\, m_{\rm lim}) = \bar{n}(z)\left[1 + \Delta(z, \mathbf{n}; m_{\rm lim})\right], \tag{2.1}$$

where $\bar{n}(z)$ is the mean galaxy density per red-shift and per steradian at red-shift z, and

$$\begin{aligned}\Delta(z, \mathbf{n}; m_{\rm lim}) &= b(z)D + \frac{1}{\mathcal{H}}\left[\dot{\Phi} + \partial_r^2 V\right] + (2 - 5s)\left[\int_0^r \frac{d\tilde{r}}{r}(\Phi + \Psi) - \kappa\right] \\ &+ (f_{\rm evo} - 3)\,\mathcal{H}V + (5s - 2)\Phi + \Psi + \left(\frac{\dot{\mathcal{H}}}{\mathcal{H}^2} + \frac{2 - 5s}{r\,\mathcal{H}} + 5s - f_{\rm evo}\right) \\ &\times \left(\Psi + \partial_r V + \int_0^r d\tilde{r}(\dot{\Phi} + \dot{\Psi})\right)\end{aligned} \tag{2.2}$$

is the perturbation in the number density of sources which emerges due to both red-shift density perturbations and volume distortions [94–96]. In Eq. (2.2), $b(z)$ takes into account that galaxies are biased tracers of the underlying dark matter distribution, D is the density fluctuation in comoving gauge, $\mathcal{H} \equiv aH$ is the conformal Hubble parameter, Φ and Ψ are the Bardeen potentials [50], V is the velocity potential for peculiar velocities in the longitudinal gauge, $v_i = -\partial_i V$, s is the magnification bias , κ is the convergence, r is the comoving distance, $f_{\rm evo}$ is the evolution bias, and a dot denotes derivative w.r.t. conformal time. Both the evolution bias and the magnification bias functions are defined below when giving the survey specifications.

Similarly to what is done in CMB analysis with temperature fluctuations, it is useful to expand the perturbation in the number density of galaxies in spherical harmonics $Y_{\ell m}(\mathbf{n})$. Whereas for the CMB case one expands the temperature fluctuations field $\Delta T(\mathbf{n})$ at a single red-shift ($z \sim 1000$), when analysing galaxy catalogues we have data for a range of red-shifts and therefore the expansion takes into account this red-shift dependence

$$\Delta(z, \mathbf{n}) = \sum_{\ell, m} a_{\ell m}(z) Y_{\ell m}(\mathbf{n}), \tag{2.3}$$

where we have omitted the limiting magnitude. Assuming statistical isotropy, it is possible to define the angular matter power spectrum through the expansion (2.3) as

$$\langle a_{\ell m}(z) a^*_{\ell m}(z')\rangle \equiv \delta_{\ell\ell'}\delta_{mm'} C_\ell(z, z'). \tag{2.4}$$

In practice, galaxy clustering data is commonly analysed by using tomographically binned samples of galaxies. The catalogue can be divided in different red-shift bins according to normalised window functions $W_{\Delta z_i}(z, z_i)$ of width Δz_i and centred in red-shift z_i. One can then define correlations between red-shift bins i and j as

$$C_\ell^{ij} \equiv \int dz dz' W_{\Delta z_i}(z, z_i) W_{\Delta z_j}(z, z_j) C_\ell(z, z'). \tag{2.5}$$

In this project we have used synthetic galaxy clustering data for a survey consistent with the Euclid photometric catalogue:

- the covered sky fraction $f_{\rm sky} = 0.364$;
- we divide the catalogue into $N_{\rm bin} = 5$ Gaussian red-shift bins (Gaussian window functions $W_{\Delta z_i}$) containing equal number of galaxies;
- the galaxy red-shifts are assumed to range from 0.1 to 2;
- the galaxy density $d = 30\,{\rm arcmin}^{-2}$;
- the number of galaxies per red-shift and per steradian

  $$\frac{dN}{dz d\Omega} = 3.5 \times 10^8 z^2 \exp\left[-\left(\frac{z}{z_0}\right)^{3/2}\right] \qquad z_0 = 0.637, \tag{2.6}$$

  is shown in Figure 2.1;
- the number of galaxies per steradian within a given red-shift bin is

  $$\mathcal{N} = \frac{1}{N_{\rm bin}} \int dz \frac{dN}{dz d\Omega}; \tag{2.7}$$

- as suggested by previous studies (see, for instance, [23]) we assume a scale-independent galaxy bias

  $$b(z) = b_0 \sqrt{1+z}; \tag{2.8}$$

- following [97], the magnification bias for an Euclid-like survey is modelled as

  $$s(z) = \sum_{k=0}^{3} s_k z^k, \tag{2.9}$$

  with $s_0 = 0.1194$, $s_1 = 0.2122$, $s_2 = -0.0671$, $s_3 = 0.1031$;

- finally, the evolution bias

$$f_{\rm evo}(z) \equiv \frac{\partial \ln \left(a^3 \frac{dN}{dz d\Omega} \right)}{\partial \ln a}, \tag{2.10}$$

where a is the scale factor and we assume that the survey observes all the galaxies in the windows. The galaxy bias and the magnification bias are shown in Figure 2.2.

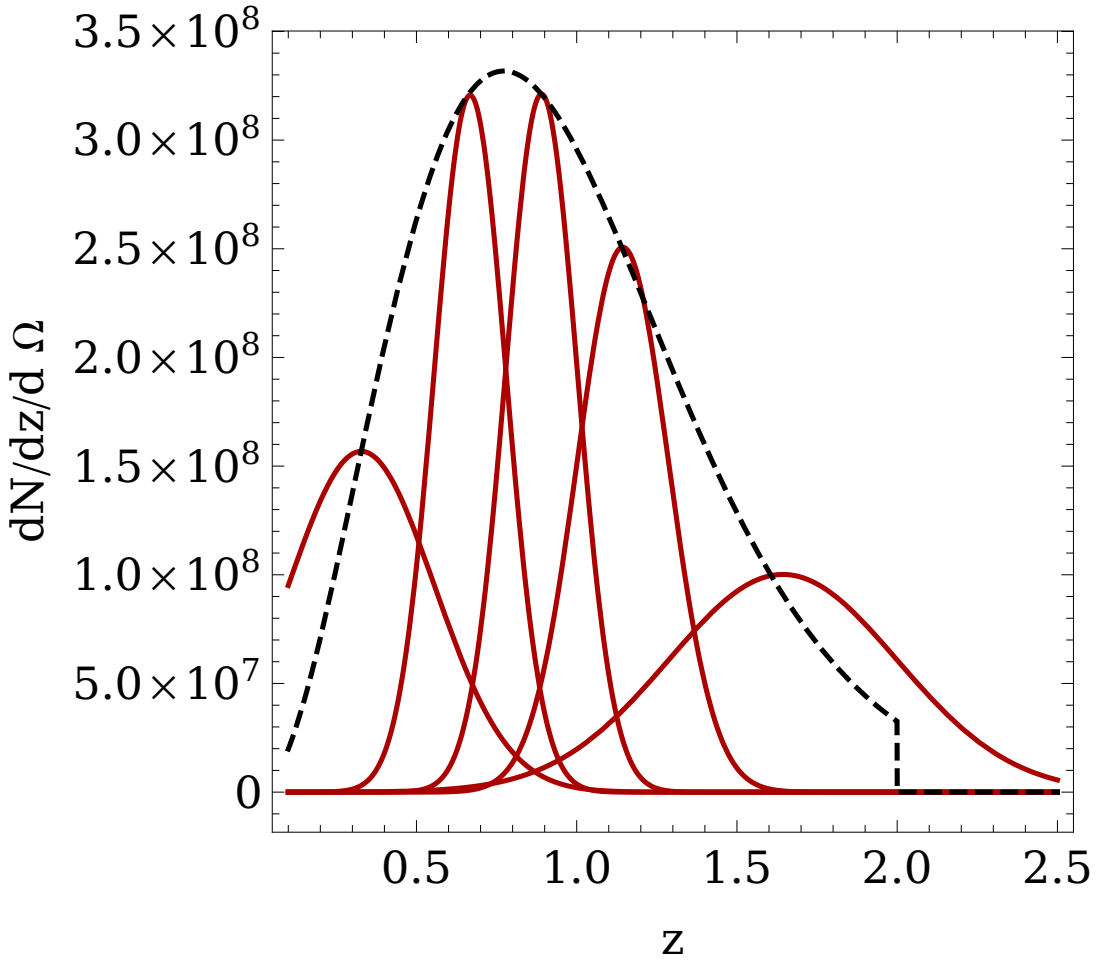

Fig. *2.1: Euclid photometric galaxy density distribution (black line) with a division into 5 bins containing the same number of galaxies.*

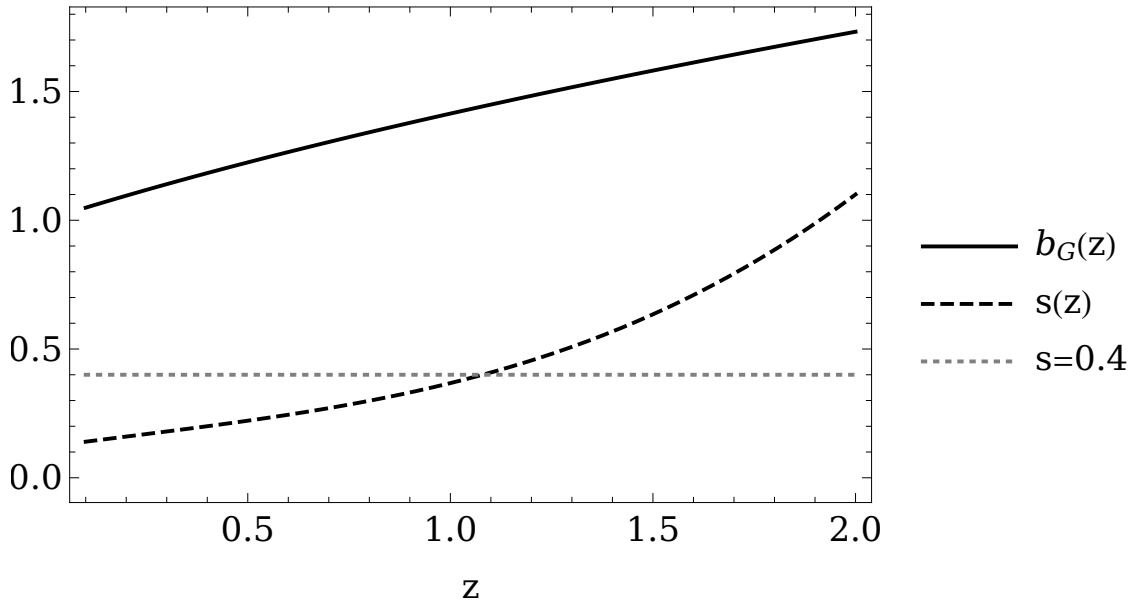

Fig. *2.2: Galaxy bias $b_G(z)$ and magnification bias $s(z)$ for Euclid. The magnification bias is computed at the limiting magnitude $m_{\rm lim} = 24.5$. As a reference, we also plot the value $s = 0.4$ at which the lensing contribution to number counts changes sign.*

Having the survey specifications we can compute angular matter power spectrum as in Eq. (2.5). We have utilised the code CLASSgal [98] where galaxy number counts have been implemented including relativistic corrections in Eq. (2.2). In the next section we study the importance of including the effect of lensing convergence in galaxy clustering analyses when determining the neutrino mass.

2.3 Methodology

In order to show how important the inclusion of lensing convergence in galaxy clustering analyses is, we perform a Markov Chain Monte Carlo (MCMC) analysis [24, 62, 99] both including and neglecting the lensing effect. Studies analysing the bias on cosmological parameters due to neglecting lensing convergence can be found in the literature, but they do Fisher matrix analyses and focus on either the primordial non-Gaussianity parameter (i.e., $f_{\rm NL}$) [100] or dark energy parameters (e.g., w, Ω_Λ) [101]. Although in this project we stress on the neutrino mass, we also discuss other parameters in the concordance model.

The MCMC technique is more suitable than a Fisher matrix method. Current Boltzmann codes such as CLASS [102] or CAMB [64] are accurate to 1% (with nominal precision settings), but it is possible for random numerical errors to exceed this. Future surveys will provide more precise Large Scale Structure (LSS) measurements and therefore these effects might become problematic for approaches that rely on computation of derivatives as a function of parameters (e.g., Fisher matrix). Since our MCMC approach average over $\sim 10^5$ galaxy number counts spectra, it is much less sensitive to those numerical errors than the Fisher matrix approach.

We assume a fiducial flat ΛCDM model consistent with results from the Planck collaboration [21], including massive neutrinos with a normal mass hierarchy (dominated by the heaviest neutrino mass eigenstate). The cosmological parameters of our fiducial model are the reduced baryon density parameter, $\omega_{\rm b} = 2.225 \times 10^{-2}$, the cold dark matter density parameter, $\omega_{\rm cdm} = 0.1198$, the scalar spectral index, $n_{\rm s} = 0.9645$, the amplitude of curvature fluctuations, $\ln 10^{10} A_{\rm s} = 3.094$, the Hubble constant, $H_0 = 67.27\,{\rm km\,s^{-1}\,Mpc^{-1}}$, and the sum of the neutrino masses, $\sum m_\nu = 0.06\,{\rm eV}$.

To take into account a theoretical error on non-linear scales we use Halofit [103] to rescale all linear transfer functions. The rescaling for the matter power spectrum in models including massive neutrinos has been already implemented in CLASSgal. Transfer functions are rescaled by the square root of

$$\alpha(k,z) = \frac{\ln[1+k/k_{\rm NL(z)}]}{1+\ln[1+k/k_{\rm NL(z)}]} f_{\rm th}, \tag{2.11}$$

where $k_{\rm NL}$ is the non-linear scale determined by the Halofit algorithm, and $f_{\rm th}$ is the error percentage on non-linear scales that we have chosen to be $f_{\rm th} = 10\%$. The theoretical error power spectra E_ℓ^{ij} are then computed by taking the absolute value of the resulting C_ℓ^{ij}. Because computing E_ℓ^{ij} with high accuracy is time-computing demanding, in this project we compute the error power spectra only for the fiducial model, that is, we ignore the parameter dependence on the theoretical error. In addition, since the perturbation on the number density of galaxies is not a continuous field, it is usually assumed that galaxies form a Poisson sample of the density field [92] and therefore there is a shot-noise contribution $\mathcal{N}^{-1}$ to the error budget in the angular power spectra.

Finally, the galaxy number counts are modelled as

$$C_\ell^{A,\,ij} = C_\ell^{ij} + E_\ell^{ij} + \mathcal{N}^{-1}\delta^{ij}, \tag{2.12}$$

where $A =$ obs, th and $i, j = 1, ..., N_{\rm bin}$ are red-shift bin indices. Here $C_\ell^{\rm obs}$ stands for spectra computed for our fiducial model which includes the effect of lensing convergence, and $C_\ell^{\rm th}$ stands for models which might or might not include lensing convergence. In the next Section we will study the impact of switching lensing convergence off in $C_\ell^{\rm th}$ when fitting this kind of models to our fiducial $C_\ell^{\rm obs}$.

Following the cosmic shear implementation in [104] we have implemented a Gaussian likelihood for an Euclid-like survey. For given observed and theoretical power spectra in Eq. (2.12), let us define the determinants

$$d_\ell^{\rm th} = \det\left(C_\ell^{{\rm th},\,ij}\right), \tag{2.13}$$

$$d_\ell^{\rm obs} = \det\left(C_\ell^{{\rm obs},\,ij}\right). \tag{2.14}$$

Additionally, one can define a mixed determinant $d_\ell^{\rm mix}$ formed from $d_\ell^{\rm th}$: one takes each term in $d_\ell^{\rm th}$ and replaces one at a time $C_\ell^{{\rm th},\,ij}$ by the corresponding $C_\ell^{{\rm obs},\,ij}$. If we worked with 2 red-shift bins, the mixed determinant would read

$$d_\ell^{\rm mix} = C_\ell^{{\rm obs},\,11} C_\ell^{{\rm th},\,22} + C_\ell^{{\rm th},\,11} C_\ell^{{\rm obs},\,22} - 2 C_\ell^{{\rm th},\,12} C_\ell^{{\rm obs},\,12}. \tag{2.15}$$

It is known that in an ideal full-sky experiment, the different multipoles in an spherical harmonics expansion of a given function are uncorrelated. Then in this simple case one can write the Gaussian likelihood

$$\mathcal{L} = \widetilde{\mathcal{N}} \Pi_\ell \left\{ \frac{1}{(d_\ell^{\rm th})^{\frac{2\ell+1}{2}}} \exp\left[-\frac{(2\ell+1)}{2} \frac{d_\ell^{\rm mix}}{d_\ell^{\rm th}} \right] \right\}, \tag{2.16}$$

where $\widetilde{\mathcal{N}}$ is a normalisation constant. The effective chi square is defined as

$$\chi^2_{\rm eff} \equiv -2 \ln \mathcal{L} = -2 \ln \widetilde{\mathcal{N}} + \sum_\ell (2\ell+1) \left(\ln d_\ell^{\rm th} + \frac{d_\ell^{\rm mix}}{d_\ell^{\rm th}} \right), \tag{2.17}$$

which is minimal for $d_\ell^{\rm mix} = N_{\rm bin} d_\ell^{\rm th} = N_{\rm bin} d_\ell^{\rm obs}$. Having into account the partial sky coverage these definitions lead to a χ^2 relative to the fiducial model given by

$$\Delta\chi^2 = \sum_{\ell=2}^{\ell_{\rm max}} (2\ell+1) f_{\rm sky} \left(\ln \frac{d_\ell^{\rm th}}{d_\ell^{\rm obs}} + \frac{d_\ell^{\rm mix}}{d_\ell^{\rm th}} - N_{\rm bin} \right), \tag{2.18}$$

where to be conservative in the treatment of non-linear effects we use $\ell_{\rm max} = 400$. In order to optimise the computation of the angular power spectra $C_\ell^{{\rm A},\,ij}$ we use the Limber approximation and adjust the precision parameters in CLASSgal to have $\Delta\chi^2 \lesssim 0.2$ for $C_\ell^{\rm th}$ including lensing evaluated at the fiducial model. These adjustments are necessary to make feasible our MCMC approach and mean that our computations are accurate up to $\Delta\chi^2 \lesssim 0.2$.

2.4 Results

Utilising the approach explained in Section 2.3, we have performed the three following MCMC analyses:

1. $C_\ell^{\rm th}$ including lensing convergence.
2. $C_\ell^{\rm th}$ neglecting lensing convergence.
3. $C_\ell^{\rm th}$ neglecting lensing convergence, but including only auto-correlations.

We have done these analyses in two ways. First, we assume no previous information and use wide, flat prior distributions for the cosmological parameters. Second, we consider a more realistic scenario where information from a full-sky CMB experiment is provided. In this case we assume a Gaussian prior distribution for the pertinent cosmological parameters; we compute the covariance matrix for a model with varying neutrino mass from information provided by the Planck collaboration. In addition to these two analyses, we do a Fisher matrix analysis no using priors and compare results with the corresponding MCMC analysis. We close this section by estimating the significance of lensing detection with an Euclid-like survey.

2.4.1 MCMC with wide, flat priors

The Figure 2.3 shows two- and 1-D posteriors for the three mentioned analyses using wide, flat priors on the cosmological parameters. The corresponding constraints are shown in Table 2.1. Red contours indicate results for the analysis that consistently includes lensing convergence in the theoretical model fitting the mock data. The analysis neglecting lensing convergence, but including only red-shift bin auto-correlations (i.e. $C_\ell(z,z)$), is depicted in gray. Blue contours show the analysis neglecting lensing, but including all possible red-shift bin correlations (i.e. $C_\ell(z,z')$).

The analysis that consistently includes lensing convergence (red contours in Figure 2.3) should output the fiducial model. The corresponding constraints in Table 2.1 show that the best fitting parameters are indeed very close to the input fiducial parameters (see the amplitude of the shift of the best fit). The amplitude of the shifts of the mean of some parameters (i.e., m_ν, H_0, ω_{cdm}, ω_b) reveal the limitations of our analysis. On the one hand, since the main impact of massive neutrinos occurs on small scales and we treat non-linear scales very conservatively, an improvement on the constraints of the neutrino absolute mass scale is expected in an analysis

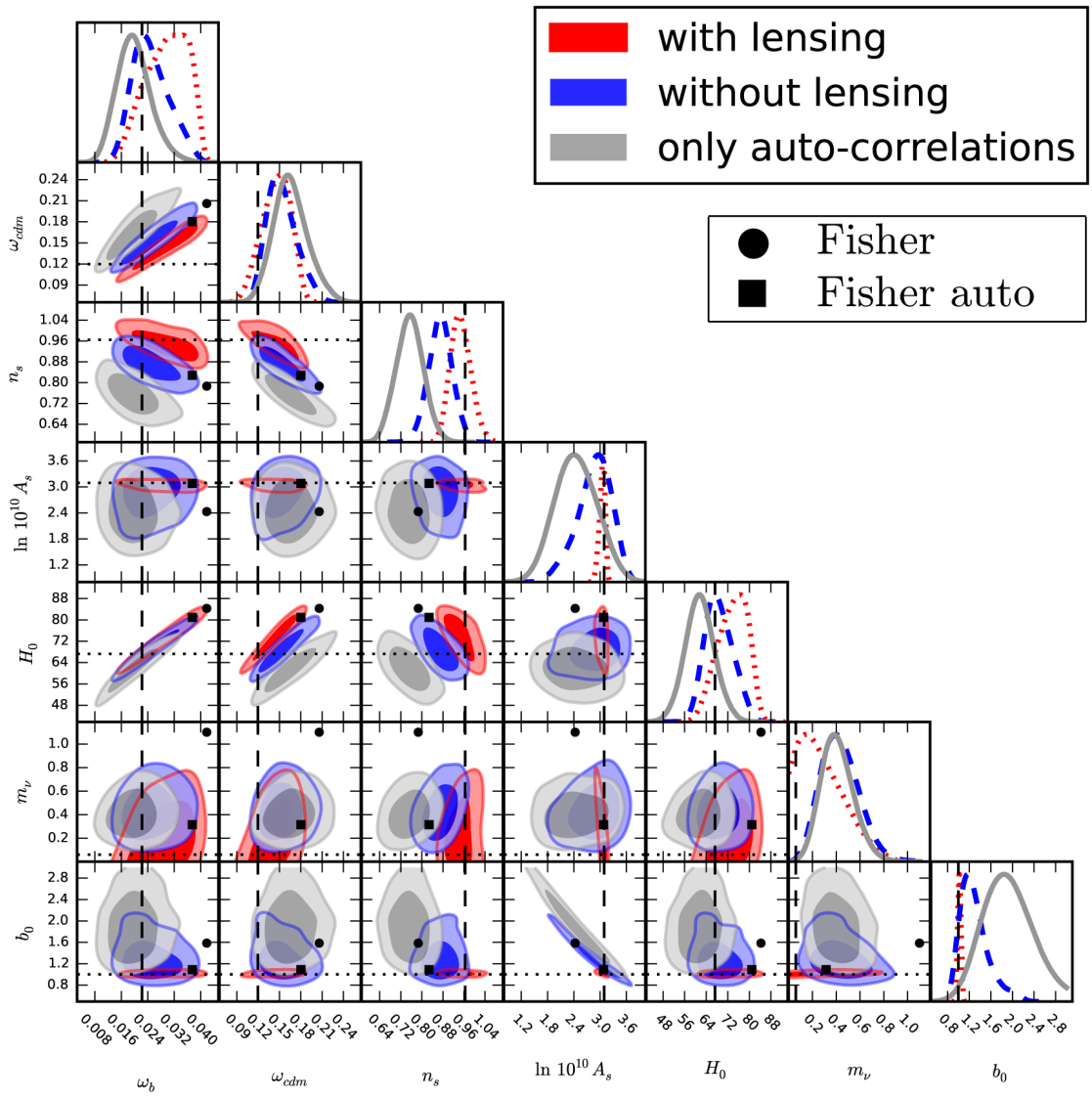

Fig. *2.3: Two- and 1-D posteriors for the cosmological parameters inferred from the full analysis including lensing (red dotted), an analysis neglecting lensing (blue dashed) and considering only auto-correlations (gray solid). The 68% and 95% confidence intervals are shown. Intersections between vertical and horizontal lines denote the fiducial cosmology. In this analysis no significant priors were imposed on the parameters. Circles and squares represent the estimates for the best-fits from a Fisher matrix analysis when neglecting lensing, and for the only auto-correlations case, respectively.*

i) Consistently including lensing: $\Delta\chi^2 = 0$					
Parameter	Mean	best fit	σ	shift: mean	best-fit
ω_b	0.02979	0.02285	0.00624	1.2σ	0.1σ
ω_{cdm}	0.1455	0.1219	0.0200	1.3σ	0.1σ
n_s	0.9476	0.9642	0.0387	0.4σ	$< 0.1\sigma$
$\ln 10^{10} A_s$	3.047	3.097	0.065	0.7σ	$< 0.1\sigma$
$H_0 \left[\frac{\text{km}}{\text{s·Mpc}}\right]$	73.84	67.84	5.48	1.2σ	0.1σ
m_ν [eV]	0.29	0.09	0.19	1.2σ	0.2σ
b_0	1.018	1.000	0.031	0.6σ	$< 0.1\sigma$
ii) Neglecting lensing: $\Delta\chi^2 = 2064$					
Parameter	Mean	best fit	σ	shift: mean	best-fit
ω_b	0.02494	0.02120	0.00556	0.5σ	0.1σ
ω_{cdm}	0.1532	0.1435	0.0208	1.6σ	1.1σ
n_s	0.8702	0.8837	0.0446	2.1σ	1.8σ
$\ln 10^{10} A_s$	2.867	2.965	0.394	0.6σ	0.3σ
$H_0 \left[\frac{\text{km}}{\text{s·Mpc}}\right]$	68.73	66.76	5.14	0.3σ	0.1σ
m_ν [eV]	0.43	0.41	0.16	2.3σ	2.2σ
b_0	1.293	1.200	0.271	1.1σ	0.7σ
iii) Neglecting lensing: $\Delta\chi^2 = 180$ (only auto-correlations)					
Parameter	Mean	best fit	σ	shift: mean	best-fit
ω_b	0.01982	0.01737	0.00520	0.5σ	0.9σ
ω_{cdm}	0.1658	0.1552	0.0242	1.9σ	1.5σ
n_s	0.7539	0.7675	0.0513	4.1σ	3.8σ
$\ln 10^{10} A_s$	2.449	2.719	0.465	1.4σ	0.8σ
$H_0 \left[\frac{\text{km}}{\text{s·Mpc}}\right]$	61.64	59.11	5.43	1σ	1.5σ
m_ν [eV]	0.41	0.41	0.14	2.6σ	2.5σ
b_0	1.888	1.603	0.428	2.1σ	1.4σ

Tab. *2.1: MCMC results (flat prior). We show the mean and best fit values, the standard deviation and the amplitude of the shift of the mean and best-fit w.r.t the fiducial value in units of the standard deviation, σ, of the corresponding analysis. The large value of $\Delta\chi^2$ for case ii) shows that cross-correlations cannot be fitted if lensing is neglected. A shift of less than about 0.2σ is not serious and probably due to the reduced precision used to compute the theoretical spectra.*

including, for instance, scales up to $\ell = 2000$. On the other hand, the universe's expansion rate, the reduced baryon density parameter, and the cold dark matter density parameter are not well constrained due to degeneracies in these parameters

(see Figure 2.3). These degeneracies come from the dominant contributions in the matter transfer function that are basically fixed by the ratio $\omega_b/\omega_{\rm cdm}$ and by the scale of the particle horizon at the radiation-matter equality epoch $z_{\rm eq}$ [105]. The equality scale $k_{\rm eq}$ behaves like

$$k_{\rm eq} \propto \frac{\omega_m}{H_0}, \tag{2.19}$$

where we assume a fixed radiation content and measure $k_{\rm eq}$ in h/Mpc.

Gray contours in Figure 2.3 show the analysis neglecting lensing, but including only red-shift bin auto-correlations. The effective $\Delta\chi^2$ for this case is greater than in the case consistently including lensing, thus suggesting that the model neglecting lensing has difficulties in fitting the mock data. The spectral index and the neutrino mass are significantly biased ($> 2.5\sigma$) from the input fiducial parameters. Moreover, a degeneracy between the bias parameter b_0 and the amplitude of scalar fluctuations A_s appears. This comes from the fact that the product $A_s b_0^2$ determines the overall amplitude of matter fluctuations and therefore its increase (decrease) signifies an enhancement (decrement) of power on all scales. The bias on n_s and m_ν can be understood as follows. Since the magnification bias in $s(z)$ Eq. (2.9) is relatively large (see Figure 2.2), the density-lensing correlation term

$$b(z)(5s(z) - 2)\langle D\kappa\rangle, \tag{2.20}$$

contributes to the power with a positive (negative) sign for red-shift bins with $z > 1$ ($z < 1$). Because correlations of relatively small red-shifts bins probe mainly small scales, the decrement of power on small scales due to lensing convergence must be corrected in a model no including lensing. This correction can be achieved by lowering the spectral index – since $P(k) \propto k^{n_s-1}$ – and increasing the neutrino mass.

Finally, we focus our attention on the analysis that neglects lensing convergence, but includes all red-shift bin correlations (blue contours in Figure 2.3). Although bias on cosmological parameters appear to be smaller in this case – as compared to the gray contours –, this improvement is not significant. Since the lensing term might actually dominate the radial power spectrum at large scales [94], it is even more difficult for a model that neglects lensing and includes cross-correlations to fit the mock data. This is easily seen with the value of the effective $\Delta\chi^2$ in Table 2.1. The $\Delta\chi^2$ increases from $\Delta\chi^2_{\rm auto} \simeq 180$ for the five auto-correlation bins to more than $\Delta\chi^2_{\rm a+c} \gtrsim 2000$ when adding the 10 cross-correlation bins. If one naively gives each bin the same weight, one would expect an increase by a factor 3. We however find an increase $\Delta\chi^2_{\rm a+c}/\Delta\chi^2_{\rm auto} \gtrsim 11$.

Parameter	Shift of best-fit		for MCMC	
ω_b	1.2σ	(0.9σ)	-0.1σ	(-0.9σ)
ω_{cdm}	1.7σ	(1.1σ)	1.1σ	(1.5σ)
n_s	-1.9σ	(-1.3σ)	-1.8σ	(-3.8σ)
$\ln 10^{10} A_s$	-1.1σ	(0.005σ)	-0.3σ	(-0.8σ)
$H_0 \left[\frac{\text{km}}{\text{s·Mpc}}\right]$	1.2σ	(0.9σ)	-0.1σ	(-1.5σ)
m_ν [eV]	3.3σ	(0.6σ)	2.2σ	(2.5σ)
b_0	1.7σ	(0.1σ)	0.7σ	(1.4σ)

***Tab.** 2.2: Fisher matrix results for the shift in the best-fit values due to neglecting lensing, in units of standard deviations (see Figure 2.5). The numbers in parenthesis refer the the case including only bin auto-correlations. For comparison we also give in columns 4 and 5 the corresponding values from the MCMC analysis presented in Table 2.1 and Fig. 2.3. While Fisher matrices give a good qualitative description of parameter degeneracies, estimates of the shifts in the best-fits seriously misestimate the magnitude and direction in parameter space.*

Models with additional parameters, but neglecting lensing convergence are likely to weaken the constraints – introducing new degeneracies – and produce even stronger biases on the cosmological parameters. Therefore, from the analyses presented above, we conclude that to go beyond the current state and derive accurate estimates of the absolute neutrino mass scale with galaxy surveys absolutely requires taking lensing convergence into account. Figure 2.4 shows number counts angular power spectra for analyses including and neglecting lensing computed at the corresponding best fit (see Table 2.1). The thick red lines indicate the model including lensing and the thin blue lines show the model neglecting lensing (including all red-shift bin cross-correlations). For the spectra of the model consistently including lensing, we show 1-σ error bars that were computed by assuming Gaussian spectra (see Eq. (2.13) of [97]). Correlations between the red-shift bins $(ij) = (11)$, (55) and (15) are shown. One can see that when neglecting lensing, the spectrum for the cross-correlation between red-shift bins 1 and 5 lies outside the 1-σ error bars around the fiducial spectrum including lensing. This clearly evidences that a model neglecting lensing convergence cannot fit the mock data.

2.4.2 Fisher analysis without priors

An alternative, widely used approach to make forecasts is the Fisher matrix method [100,101,106,107]. In this subsection, we compare how well a Fisher matrix technique performs as compared to the MCMC method of the precedent subsection. Since we have seen the biases on cosmological parameters might reach several standard deviations when neglecting lensing convergence in the analysis, we expect the Fisher

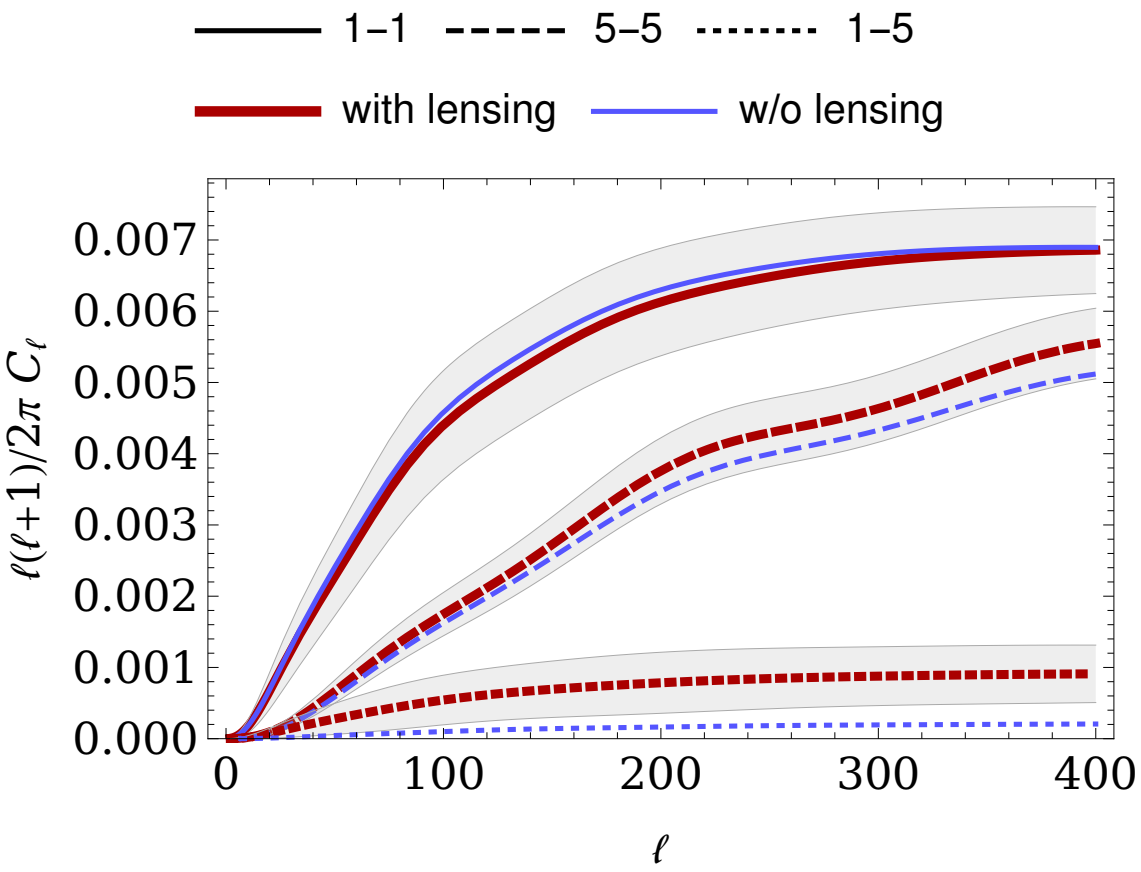

Fig. *2.4: The thick red and the thin blue lines correspond to the spectra at the best-fit values estimated by consistently including lensing and by neglecting it, respectively. Gaussian error bars accounting for cosmic variance and shot-noise for the consistent analysis are shown as gray regions. The indices for the correlated redshift bins are shown in the legend. The model neglecting lensing cannot fit the data, especially due to redshift cross-correlations.*

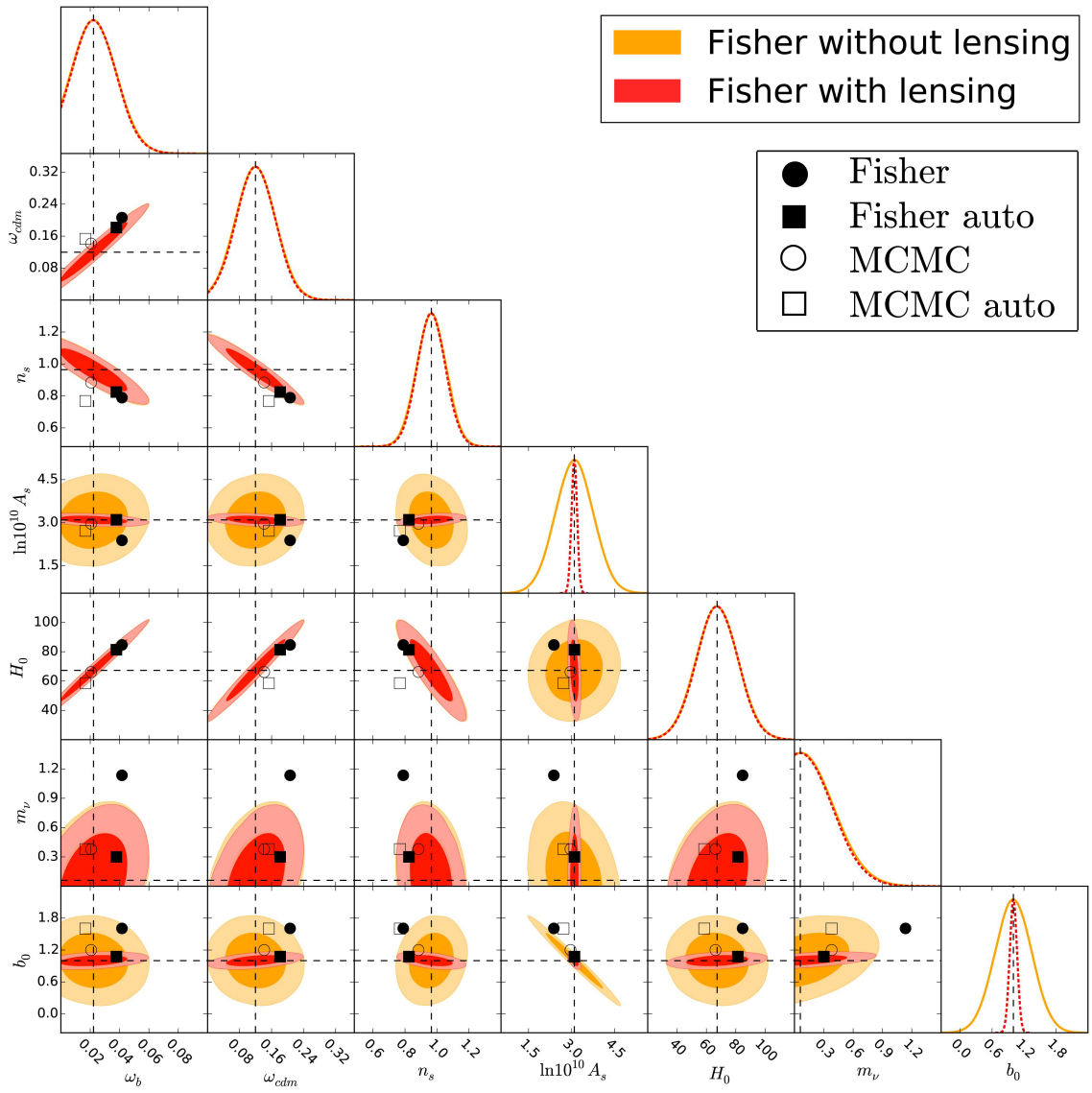

Fig. *2.5: Two- and 1-D posteriors for the cosmological parameters inferred from the Fisher analysis excluding (orange solid) and including lensing (red dotted). We stress that, in the former case, to compute error ellipses within the Fisher formalism we forecast parameter constraints in a Universe where lensing is absent (see the text for more details). The 68% and 95% confidence intervals are shown. Intersections of dashed lines denote the fiducial cosmology. The expected systematic shifts in the best-fit due to neglecting lensing in the theoretical modeling are shown, including all bin correlations (circles), and including only auto-correlations (squares). For comparison, we also show the corresponding results from the MCMC analysis. While the Fisher formalism is reliable for a qualitative understanding of parameter degeneracies, the systematic errors are seriously misestimated. See table 2.2 for more details about statistical quantities.*

matrix forecasts to be not very reliable (see Section 2.3). The basic expressions of the Fisher matrix formalism are explained in the Appendix C.

The figure 2.5 shows two- and 1-D posteriors for two Fisher analyses. Red contours indicate forecasts for an analysis consistently including lensing convergence, whereas yellow contours show results for an analysis where lensing is neglected (not only in the model, but also in the underlying universe). Red contours in both Figure 2.3 and Figure 2.5 can therefore be directly compared. The shifts of the best fit parameters for analyses neglecting lensing are computed as explained in Appendix C and shown in Table 2.2. The standard deviations σ in this Table refer to the model neglecting lensing which provides more conservative information about the importance of the systematic error.

Comparing Figures 2.3 and 2.5, we can see that the Fisher matrix analysis provides a good qualitative description of degeneracy between different parameter constraints. Although the 68% confidence intervals are in disagreement with MCMC results by a factor 2-3, the shape and inclination of the ellipses very roughly follow the MCMC contours. On the other hand, the Fisher matrix analysis badly fails in determining the magnitude and direction of the best-fit shift in parameter space. Indeed, the first-order formalism that we use to estimate the shift in the best-fitting parameters due to a systematic error – neglecting lensing convergence – is valid as long as the shift is small compared to the errors, and it also assumes that the systematic error does not affect the ellipse contours [108]. The results from the MCMC approach in the previous subsection and the contours depicted in Figure 2.5 clearly show that these assumptions are not fulfilled in the present case.

2.4.3 MCMC with Planck Gaussian prior

As discussed above, degeneracies in parameter space limit the constraints from measurements of the galaxy power spectrum. This difficulty is usually tackled by applying a variety of priors or constraints on parameters, and combining the galaxy clustering data with other cosmological measures, such as CMB experiments [24]. We therefore repeat our MCMC analysis using Planck priors for all the cosmological parameters except the bias b_0, which is not measured in *Planck*, and the neutrino mass. The latter is our most interesting parameter and we want to test how strongly it is biased in an analysis which neglects lensing.

Planck chains are publicly available through the *Planck Legacy Archive*. In this paper we use the chain for the extended model with a free neutrino mass based on

the *Planck* TT, TE, EE + lowP likelihoods (Equation [54c] in [21]). We compute the covariance matrix $\mathbf{C}$ for the cosmological parameters $\vec{x} = (\omega_b, \omega_{\rm cdm}, n_s, A_s, H_0)$ and assume a Gaussian distribution for the prior. The χ^2 relative to the fiducial model including the Planck prior is then the $\Delta\chi^2$ in Eq. (2.18) plus

$$\Delta\chi^2_{\rm prior} = \sum_{i,j}(x_i - x_i^{\rm fid})C_{ij}^{-1}(x_j - x_j^{\rm fid}), \tag{2.21}$$

where $\vec{x}^{\rm fid}$ denotes parameters of the fiducial model and $\mathbf{C^{-1}}$ is the inverse of the covariance matrix. In this way we marginalize the Planck prior over the neutrino mass and the optical depth, τ, which are parameters that we want to leave free since we want to determine the first and our survey is not sensitive to the second. The results are shown in Table 2.3 and Fig. 2.6.

Red contours in Figure 2.6 indicate the full analysis including lensing convergence. Adding CMB information clearly helps to remove degeneracies and cosmological parameters are now better determined than for the case with wide, flat priors. Blue and gray contours show analyses neglecting lensing convergence. While the spectral index n_s shows now a smaller relative shift, the neutrino masses and galaxy bias actually acquire larger shifts. Since the model neglecting lensing must correct the number counts angular power spectrum on small scales by increasing neutrino mass and lowering spectral index, the Hubble parameter H_0 is pulled away from the fiducial value by over 4σ in spite of the Planck prior. Hence, while the details of the analysis are important in determining the actual size of error bars and degeneracies in parameter space, a large bias 2σ–9σ in the neutrino masses is a feature that persists in all the analyses here performed. Lensing convergence must be included when analysing data from future galaxy surveys, otherwise constraints on the neutrino mass will be in a high degree biased.

2.4.4 Significance of the lensing detection

We can quantify the strength with which we detect the lensing signal in our setup with the help of Bayesian model probabilities, comparing the case with lensing to the case without lensing. To do this, we introduce formally an extended model $\mathcal{M}_L$ with an additional 'lensing amplitude' parameter A_L that multiplies the lensing contribution in the model. For the 'with lensing' model $\mathcal{M}_1$ we then set $A_L = 1$, while the 'without lensing' case $\mathcal{M}_0$ corresponds to $A_L = 0$. In this way the two models are nested within the extended model and we can use the Savage-Dickey density ratio (SDDR) method to derive model probabilities (see e.g. [109] for an explanation of the

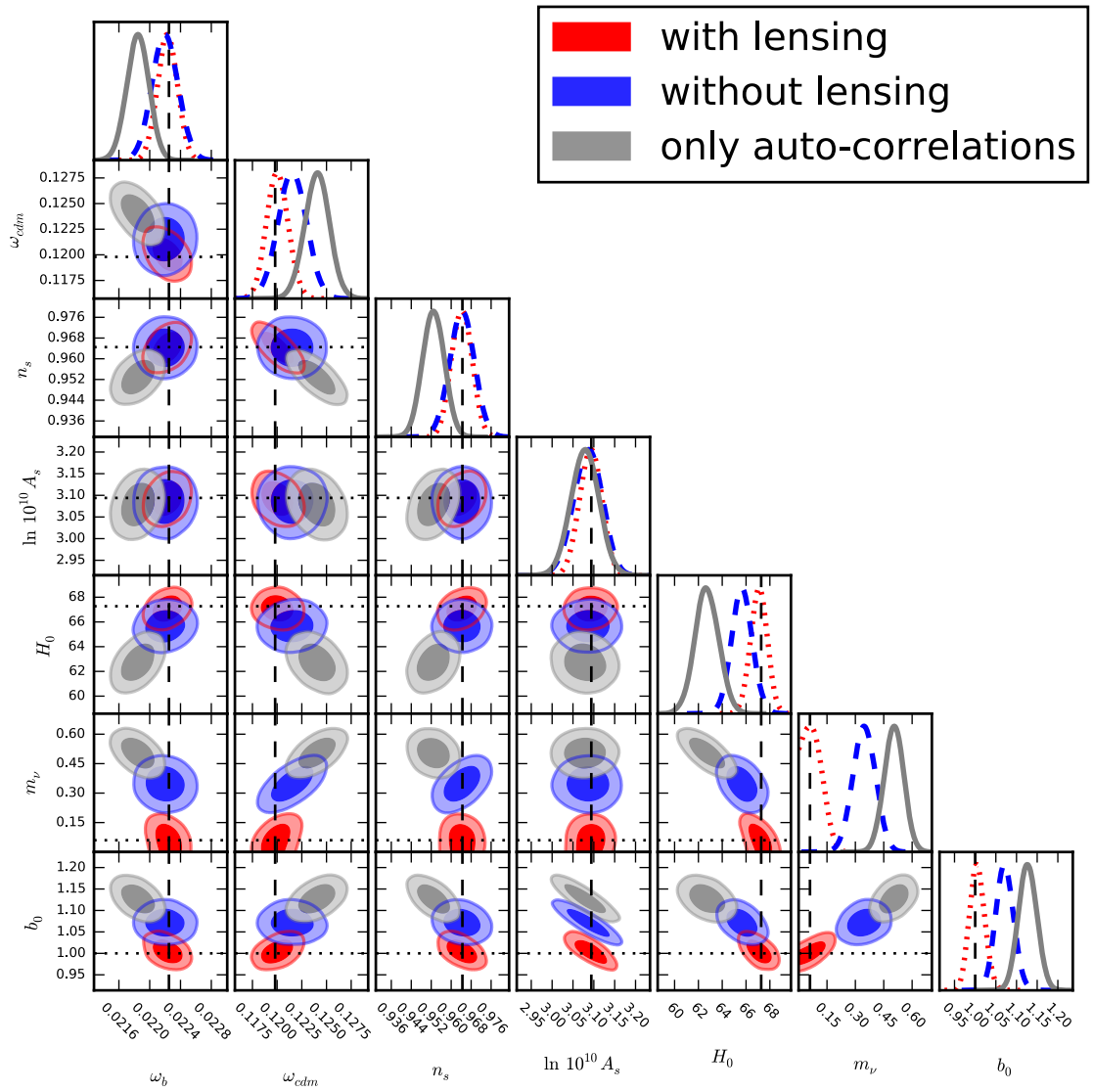

Fig. *2.6: Two- and 1-D posteriors for the cosmological parameters inferred using Planck priors. We show the full analysis including lensing (red dotted), an analysis neglecting lensing (blue dashed) and considering only auto-correlations (gray solid). The 68% and 95% confidence intervals are shown. Intersections between vertical and horizontal lines denote the fiducial cosmology. See Table 2.3 for numerical values of the statistical quantities.*

i) Consistently including lensing: $\Delta\chi^2 = 0$					
Parameter	Mean	best fit	σ	shift: mean	best-fit
ω_b	0.02223	0.02226	0.00013	0.2σ	$< 0.1\sigma$
ω_{cdm}	0.1200	0.1196	0.0011	0.2σ	0.2σ
n_s	0.9642	0.9651	0.0041	0.1σ	0.1σ
$\ln 10^{10} A_s$	3.092	3.098	0.026	0.1σ	0.2σ
$H_0 \left[\frac{\text{km}}{\text{s·Mpc}}\right]$	67.08	67.25	0.70	0.3σ	$< 0.1\sigma$
m_ν [eV]	0.08	0.04	0.05	0.4σ	0.4σ
b_0	1.005	0.994	0.018	0.3σ	0.3σ
ii) Neglecting lensing: $\Delta\chi^2 = 2082$					
Parameter	Mean	best fit	σ	shift: mean	best-fit
ω_b	0.02220	0.02219	0.00017	0.3σ	0.4σ
ω_{cdm}	0.1215	0.1214	0.0014	1.2σ	1.1σ
n_s	0.9643	0.9640	0.0049	$< 0.1\sigma$	0.1σ
$\ln 10^{10} A_s$	3.085	3.090	0.034	0.3σ	0.1σ
$H_0 \left[\frac{\text{km}}{\text{s·Mpc}}\right]$	65.66	65.64	0.87	1.8σ	1.9σ
m_ν [eV]	0.35	0.34	0.06	4.8σ	4.7σ
b_0	1.072	1.070	0.022	3.3σ	3.3σ
iii) Neglecting lensing: $\Delta\chi^2 = 230$ (only auto-correlations)					
Parameter	Mean	best fit	σ	shift: mean	best-fit
ω_b	0.02185	0.02181	0.00014	2.8σ	3σ
ω_{cdm}	0.1240	0.1240	0.0013	3.4σ	3.3σ
n_s	0.9529	0.9536	0.0044	2.7σ	2.5σ
$\ln 10^{10} A_s$	3.079	3.081	0.033	0.5σ	0.4σ
$H_0 \left[\frac{\text{km}}{\text{s·Mpc}}\right]$	62.72	62.71	1.01	4.5σ	4.5σ
m_ν [eV]	0.50	0.52	0.05	8.6σ	8.8σ
b_0	1.127	1.127	0.022	5.7σ	5.7σ

***Tab.** 2.3: MCMC results with Planck priors. We show the mean and best fit values, the standard deviation and the amplitude of the shift of the mean and best-fit w.r.t. the fiducial value in units of the standard deviation, σ, of the corresponding analysis. The large value of $\Delta\chi^2$ for case ii) shows that cross-correlations cannot be fitted if lensing is neglected.*

SDDR, and section 3 of [110] for a more detailed description of the same reasoning as the one used here): with the SDDR, the Bayes factor B between the case with fixed A_L and the general case is given by the posterior for A_L (marginalised over all

other parameters) of the general model divided by prior, both taken at the nested point,

$$B_x \equiv \frac{P(D|\mathcal{M}_x)}{P(D|\mathcal{M}_L)} = \frac{P(A_L = x|D, \mathcal{M}_L)}{P(A_L = x|\mathcal{M}_L)}\,, \tag{2.22}$$

where P denote probabilities, D the data and x is either 0 or 1. The Bayes factor between two models with given fixed values for A_L is then simply the ratio of the Bayes factors relative to the extend model,

$$\begin{aligned} B_{xy} &\equiv \frac{P(D|\mathcal{M}_x)}{P(D|\mathcal{M}_y)} \\ &= \frac{P(D|\mathcal{M}_x)}{P(D|\mathcal{M}_L)}\frac{P(D|\mathcal{M}_L)}{P(D|\mathcal{M}_y)} = \frac{B_x}{B_y} \\ &= \frac{P(A_L = x|D, \mathcal{M}_L)}{P(A_L = y|D, \mathcal{M}_L)}\,, \end{aligned} \tag{2.23}$$

where the last equality holds if $P(A_L = x|\mathcal{M}_L) = P(A_L = y|\mathcal{M}_L)$, e.g. for an uniform prior in A_L, which is what we will use. We see that the only information needed to determine B_{xy} is the relative value of the posterior at $A_L = x$ and at $A_L = y$, and this is approximately given by the χ^2 difference between these cases. As by construction $A_L = 1$ (the case where we include lensing consistently) has $\Delta\chi^2 = 0$, we find simply that $\ln B_{01} \approx -\Delta\chi^2_{\text{no lensing}}/2$. We find thus that $\ln B_{01} \approx -1000$ when using auto- and cross-correlations, and $\ln B_{01} \approx -90$ to -115 when only taking into account autocorrelations. Both Bayes factors are way out on the often-used Jeffreys' scale [111] where anything larger than 5 is considered as strong. In other words, lensing is detected in both cases with an overwhelming evidence.

We can also translate the $\Delta\chi^2$ value into an order-of-magnitude estimate of 'the number of sigmas' with which we detect the lensing signal in our setup. Assuming a Gaussian probability distribution function for A_L so that $\Delta\chi^2 \approx (A_L - 1)^2/\sigma[A_L]^2$, we find that $\sigma[A_L]$ needs to be 0.022 in order to explain the observed $\Delta\chi^2$ values of 2064 and 2082. This implies that the lensing is measured roughly at the 45σ level. Lensing is clearly a strong signal in the photo-z type survey that we have considered here. As also discussed above, most of the lensing signal is contained in the off-diagonal spectra. The $\Delta\chi^2$ values of 180 and 230 when only looking at the auto-correlations correspond to about 13σ to 15σ, roughly comparable to the strength of the lensing detection in the *Planck* temperature power spectrum [21].

This also confirms the result of [97], which found that the lensing amplitude A_L can be determined to an accuracy of the order of (1-2)% with a Euclid like photometric survey, with the constraints coming especially from the off-diagonal (inter-bin) correlations.

2.5 Conclusions

Future galaxy surveys will probe scales comparable to the horizon. The come of all this new data will make necessary very careful analyses and appropriate modelling of the statistical properties of the matter density field. In this chapter we have investigated the impact of lensing convergence on constraints of cosmological parameters. We have utilised both MCMC and Fisher matrix approaches to study the importance of including lensing convergence when analysing galaxy clustering data. Although the Fisher matrix formalism provides qualitative information about degeneracies in the parameter space, it badly fails in determining quantitative estimations of shifts in the best fitting parameters. When performing the analysis with a MCMC approach we have found that biases of best fitting cosmological parameters might reach several standard deviations when lensing convergence is neglected in the analysis. Since the Fisher matrix technique is reliable only for shifts relatively small, this explains why Fisher matrix results wrongly estimate the bias on cosmological parameters: for shifts bigger than 2σ the linear approximation in the Fisher formalism breaks down. A MCMC method is therefore suitable as we have shown.

We have seen that analysis neglecting lensing convergence lead to biased cosmological constraints. The spectral index n_s and the neutrino mass m_ν are particularly affected. When neglecting lensing a degeneracy between the amplitude of scalar fluctuations A_s and the galaxy bias parameter b_0 appears. One understands this by noting that the product $b_0^2 A_s$ determines the amplitude of the matter power spectrum, so $b_0^2 A_s$ increases in analysis neglecting lensing to enhance power on all scales. Since the density-lensing contribution to the number counts angular power spectrum can become negative for small red-shift bins, therefore decreasing power on small scales, its effect can be mimic by changes on n_s and m_ν: decreasing the spectral index and increasing the neutrino mass one obtains a damped matter power spectrum on small scales.

Finally, we conclude by noting that the specific shifts on the best fitting cosmological parameters depend on the details of the survey. Although in this project we have used specifications for an Euclid-like survey, the important point is that a consistent

analysis of galaxy clustering data must take into account the magnification bias defined by

$$s(z) \equiv \frac{\partial \log_{10} N(z, m < m_*)}{\partial m_*}\,, \tag{2.24}$$

where $m_{\rm lim}$ is the limiting magnitude of the survey and $N(z, m)$ is the galaxy luminosity function of the survey at redshift z. Our results show that a correct modelling of number counts might lead to detection of lensing with high significance as in the case of CMB. The fact that deep galaxy surveys are so sensitive to lensing, however, is not only a curse but also a blessing. It means that these surveys will allow us to determine a map of the lensing potential at different redshifts, i.e. perform 'lensing tomography' with galaxy clustering. This will be a very interesting alternative to lensing tomography with shear measurements proposed, e.g. in [112]. Both techniques are challenging but they have different systematic errors and allow valuable cross-checks. So clearly both paths should be pursued.

Chapter 3

Determining H_0 with Bayesian hyper-parameters

3.1 Introduction

Pinning down the Hubble constant H_0 is crucial for the understanding of the standard model of cosmology. It sets the scale for all cosmological times and distances and it allows to tackle cosmological parameters, breaking degeneracies among them (e.g., the equation of state for dark energy and the mass of neutrinos). The expansion rate of the universe can either be directly measured or inferred for a given cosmological model through cosmological probes such as the cosmic microwave background (CMB). Although accurate direct measurements of the Hubble constant have proven to be difficult (e.g., control of systematic errors, relatively small data sets, fully consistency of different methods for measuring distances), significant progress has been achieved over the past decades [113, 114]. The *Hubble Space Telescope (HST)* Key Project made possible to measure H_0 with an accuracy of 10% by significantly improving the control of systematic errors [115]. More recently, in the *HST* Cycle 15, the *Supernovae and H_0 for the Equation of State (SHOES)* project has reported measurements of H_0 accurate to 4.7% ($74.2 \pm 3.6\,\mathrm{km\,s^{-1}\,Mpc^{-1}}$) [116], then to 3.3% ($73.8 \pm 2.4\,\mathrm{km\,s^{-1}\,Mpc^{-1}}$) [78] and very recently to 2.4% ($73.24 \pm 1.74\,\mathrm{km\,s^{-1}\,Mpc^{-1}}$) [32]. This remarkable progress has been achieved thanks to both an enlarged sample of SN Ia having a Cepheid calibrated distance, a reduction in the systematic uncertainty of the maser distance to NGC4258, an increase of infrared observations of Cepheid variables in the Large Magellanic Cloud (LMC).

The 2015 release in temperature, polarization and lensing measurements of the CMB by the *Planck* satellite leads to a present expansion rate of the universe given by $H_0 = 67.81 \pm 0.92\,\mathrm{km\,s^{-1}\,Mpc^{-1}}$ for the base six-parameter ΛCDM model [21]. As it is known, the derived estimation of H_0 from CMB experiments provide indirect and highly model-dependent values of the current expansion rate of the universe (requiring e.g., assumptions about the nature of dark energy, properties of neutrinos, theory of gravity) and therefore do not substitute a direct measurement in the local universe. Moreover, indirect determinations (in a Bayesian approach) rely on prior probability distributions for the cosmological parameters which might have an impact on the results.

The *Planck* Collaboration used a 'conservative' prior on the Hubble constant ($H_0 = 70.6 \pm 3.3\,\mathrm{km\,s^{-1}\,Mpc^{-1}}$) derived from a reanalysis of the Cepheid data used in [78], done by G. Efstathiou in [117]: in this reanalysis, a different rejection algorithm was used (with respect to that in [78]) for outliers in the Cepheid period-luminosity relation (the so-called Leavitt Law); in addition, [117] used the revised geometric maser distance to NGC4258 of [118]. Although consistent with the *Planck* TT estimate at the $1\,\sigma$ level, this determination of H_0 assumes that there is no metallicity dependence in the Leavitt Law. Furthermore, it discards data (i) from both Large Magellanic Cloud (LMC) and Milky Way (MW) Cepheid variables (ii) from the sample of Cepheid variables in [78] using an upper period cut of 60 days.[1]

As discussed in [114], the sensitivity to metallicity of the Leavitt Law is still an open question. In fact, due to changes in the atmospheric metal abundance, a metallicity dependence in the Cepheid period-luminosity is expected. Discarding data involves somehow arbitrary choices (e.g., chauvenet's criterion, period cut, threshold T in [117]) and might hinder our understanding of the physical basis behind the incompatibility of data sets (if any) [119]. Therefore, neither no metallicity dependence in Leavitt Law nor disregarding data seem to be very conservative assumptions.

Once systematics are under control (like the presence of unmodeled systematic errors or biases in the outlier rejection algorithm for Cepheid variables), a reliable estimate of H_0 is very important also on theoretical grounds. Confirmation of significant

[1] In [117] G. Efstathiou also shows results utilizing the rejection algorithm for outliers used in [78], but with the revised geometric maser distance to NGC4258 [118] which is about 4% higher than that adopted by [78] in their analysis. Note that in [78] (see their page 13) the authors provided a recalibration of H_0 for each increase of 1% in the distance to NGC4258 : according to this recalibration and the revised geometric maser distance their measurement would be driven downwards from $H_0 = 74.8\,\mathrm{km\,s^{-1}\,Mpc^{-1}}$ to $H_0 \approx 73.8\,\mathrm{km\,s^{-1}\,Mpc^{-1}}$ which is higher than all the reported values in table A1 of [117] for the R11 rejection algorithm.

discrepancies between direct and indirect estimates of H_0 would suggest evidence of new physics. Discrepancies could arise if the local gravitational potential at the position of the observer is not consistently taken into account when measuring the Hubble constant. Nevertheless, an unlikely fluctuation would be required to explain an offset as big as $2.4\,\sigma$ [120]. Second-order corrections to the background distance-redshift relation could bias estimations of the Hubble constant derived from CMB [121]. However, it was shown in [122] that those corrections are already taken into account in current CMB analyses.

It is clear from [117] that the statistical analysis done when measuring H_0 plays a part in the final result (for instance, through the outlier rejection algorithm, data sets included, anchors distances included, the period cut on the sample of Cepheid variables, the prior on the parameters of the Period-Luminosity relation). Given the relevance of the Hubble constant for our understanding of the universe, it is necessary to confirm previous results and prove them robust against different statistical approaches.

The goal of this project is to determine the Hubble constant H_0 by using Bayesian hyper-parameters to reanalyse the Cepheid data set used in both [78] and [32]. In Section 3.2 we explain both our notation and the statistical method employed. We then apply the method to different data sets and determine H_0 in Section 3.3. We conclude and discuss our results in Section 3.4.

3.2 Notation and formalism

3.2.1 Distances and standard candles

Astrophysical objects with a known luminosity – the so-called standard candles– are used to probe the expansion rate of the universe. In particular, measuring redshifts and apparent luminosities for supernovae type Ia (SNe Ia) one can establish an empirical redshift-distance relation for these objects. In order to estimate distances to SNe Ia one uses the luminosity distance

$$d_L \equiv \left(\frac{L}{4\pi l}\right)^{1/2}, \tag{3.1}$$

where L and l are the absolute luminosity and the apparent luminosity, respectively. For historical reasons the apparent bolometric luminosity l is defined so that

$$l = 10^{-2m/5} \times 2.52 \times 10^{-5}\,\mathrm{erg/cm^2\,s} \tag{3.2}$$

where m is the apparent bolometric magnitude [123]. Similarly, one can define the absolute bolometric magnitude M as the apparent bolometric magnitude a source would have at a distance 10 pc

$$L = 10^{-2M/5} \times 3.02 \times 10^{35}\,\mathrm{erg/s}. \tag{3.3}$$

Combining equations (3.1)-(3.3) it is possible to express the luminosity distance in terms of the distance modulus $m - M$:

$$\mu_0 \equiv m - M = 5\log_{10}\left(\frac{d_L}{1\mathrm{Mpc}}\right) + 25\,. \tag{3.4}$$

One can also estimate the luminosity distance d_L of a light source with redshift z within the context of General Relativity. Assuming a flat FLRW metric, one can compute the luminosity distance

$$d_L(z) = (1+z)c\int_0^z \frac{dz'}{H(z')} \tag{3.5}$$

where c is the speed of light and $H(z)$ is the Hubble function. Since nowadays the empirical curve for $d_L(z)$ is reasonably well known for relatively small redshift, the Hubble function may then be usefully expressed as a power series in Eq. (3.5) leading to

$$d_L(z) \equiv \frac{cz}{H_0}(1+\delta(z)) \approx \frac{cz}{H_0}\left\{1 + \frac{1}{2}[1-q_0]z - \frac{1}{6}[1-q_0-3q_0^2+j_0]z^2 + O(z^3)\right\} \tag{3.6}$$

where H_0 is the Hubble constant, q_0 is the present acceleration parameter, j_0 the present prior deceleration parameter, and $\delta(z)$ defines a function that vanishes as $z \to 0$ and can be approximately expressed as a series expansion in redshift starting with a term linear in z.

Having both an empirical curve and a theoretical estimation of $d_L(z)$ for a given set of astrophysical objects, we can then try to find the parameters which fit the data the best. Equating Eqs. (3.4) and (3.6) we obtain that

$$5\log_{10}(cz(1+\delta(z))) - m_X = 5\log_{10} H_0 - M_X - 25 \equiv 5a_X\,, \tag{3.7}$$

where X denotes the use of wavelength band X (e.g., U for ultraviolet, B for blue, and V for visual) and a_X is a constant which defines the intercept of the $\log_{10} cz - 0.2\, m_X$ relation. Defining $\delta(z)$ through $q_0 = -0.55$ and $j_0 = 1$ [124], Riess et al. [78] used the V wavelength band Hubble diagram for 153 nearby SN-Ia in the red shift range $0.023 < z < 0.1$ (a conservative lower limit in red shift imposed to avoid the possibility of a local, coherent flow biasing the results) to measure the intercept $a_V = 0.697 \pm 0.00201$. Using the Hubble diagram for 217 SNe Ia in the red shift range $0.023 < z < 0.15$, Riess et al. [32] found $a_B = 0.71273 \pm 0.00176$.

From Eqs. (3.4) and (3.7) one can easily express the apparent magnitude $m_X^{\mathrm{SNe\,Ia}}$ of a SNe Ia in terms of its distance modulus μ_0, the Hubble constant H_0, and the intercept a_X as

$$m_X^{\mathrm{SNe\,Ia}} = 5 \log_{10} H_0 + \mu_0 - 5a_X - 25\,. \tag{3.8}$$

At this point (having measured a_X) we are again in a position where we can try to find the parameters H_0 and μ_0 which adjust the best the observed $m_X^{\mathrm{SNe\,Ia}}$. Cepheid variables – another type of standard candle – are stars whose apparent luminosity is observed to vary more or less regularly with time. There exist a few known galaxies (19 up to date [32]) which simultaneously host both SNe Ia and Cepheid variables, thus providing the means to measure the distance parameter $\mu_{0,i}$ for the ith SN Ia through the Leavitt Law [125]. According to the Leavitt Law there is a relation between period and luminosity of Cepheids: in the ith galaxy, the pulsation equation for the jth Cepheid star with apparent magnitude $m_{X,i,j}^{\mathrm{Cepheid}}$ (in the passband X) and period $P_{i,j}$ leads to a relation

$$m_{X,i,j}^{\mathrm{Cepheid}} = \mu_{0,i} + M_X^{\mathrm{Cepheid}} + b_X(\log P_{i,j} - 1) + Z_X \Delta \log[O/H]_{i,j}, \tag{3.9}$$

where Z_X is the metallicity parameter, b_X is the slope of the period-luminosity relation, and M_X^{Cepheid} is the Cepheid zero point. In principle, given an anchor distance, a simultaneous fit of Eqs. (3.8) and (3.9) to observed SNe Ia and Cepheid variables magnitudes would provide constraints for the expansion rate of the universe.

Constraints for the parameters of the period-luminosity relation (3.9) can be improved by adding galaxies containing Cepheid stars and for which a direct measurement of their distance (or the derived distance modulus μ_0) is known. This is the case for the megamaser system NGC4258, LMC, and M31. Although the sample of MW Cepheid variables with parallax measurements is relatively small (15 up to date [32]) and mostly dominated by Cepheid stars with period $P < 10$ days, their inclusion helps to further constrain parameters in the period-luminosity relation. Therefore, the inclusion of any of these anchor distances in a simultaneous fit to Eqs. (3.8)-(3.9)

is required to constrain the distance parameters $\mu_{0,i}$ for the SNe Ia hosts and hence the Hubble constant H_0.

3.2.2 Hyper-parameters

Astrophysical observations are difficult, and it is not easy to estimate and include the associated errors and uncertainties correctly. Often the data sets show outliers with error bars that are much smaller than the standard deviation from the expected fit, for reasons that are not well understood or difficult to quantify. An analysis needs to deal with such outliers, typically by removing them based on some rejection rule. As discussed in [78, 116, 117], the rejection of outliers on the Cepheid period-luminosity relation has a non-negligible effect on the determination of the expansion rate of the universe. One can argue that an outlier rejection criterion: i) involves arbitrary choices (e.g., Chauvenet's criterion, period cut) which might bias the results ii) rejects data, thus increasing error bars and hindering a better understanding of the data sets [119]. The hyper-parameters (HPs, hereafter) method offers a Bayesian alternative to *ad hoc* selection of data points, avoiding problems associated with using incompatible data points [126]. Instead of adopting an a priori rejection criterion (galaxy-by-galaxy basis as in [78, 116] or from a global fit as in [117]), in this work we analyse *all* the available measurements with Bayesian HPs. The latter effectively allow for relative weights in the Cepheid variables, determined on the basis of how good their simultaneous fit to the model is.

HPs allow to check for unrecognised systematic effects by introducing a rescaling of the error bar of data point i, $\sigma_i \to \sigma_i/\sqrt{\alpha_i}$. Here α_i is a HP associated with the data point i [126]. In order to explain how HPs work, we start by assuming a Gaussian likelihood for the datum D_i,

$$P_G(D_i|\vec{w}) = \tilde{N}_i \, \frac{\exp(-\chi_i^2(\vec{w})/2)}{\sqrt{2\pi}}, \tag{3.10}$$

where χ_i^2 and the normalisation constant $\tilde{N}_i$ are given by

$$\chi_i^2 \equiv \frac{\left(x_{\mathrm{obs},i} - x_{\mathrm{pred},i}(\vec{w})\right)^2}{\sigma_i^2}\,, \quad \tilde{N}_i = 1/\sqrt{\sigma_i^2}\,. \tag{3.11}$$

Here for each measurement $x_{\mathrm{obs},i}$ there is a corresponding error σ_i and a prediction $x_{\mathrm{pred},i}(\vec{w})$, ($\vec{w}$ being the parameters of a given model). Suppose that some errors have been wrongly estimated due to unrecognised (or underestimated) systematic effects

and use hyper-parameters [126] to control the relative weight of the data points in the likelihood. For each measurement i we introduce a HP to rescale σ_i as mentioned above. In that case the Gaussian likelihood becomes [126]

$$P(D_i|\vec{w},\alpha_i) = \tilde{N}_i\,\alpha_i^{1/2}\,\frac{\exp(-\alpha_i\chi_i^2(\vec{w})/2)}{\sqrt{2\pi}}. \tag{3.12}$$

However, in general we do not know what value of α_i is correct. In order to circumvent this problem, we follow a Bayesian approach, introducing the α_i as nuisance parameters and marginalising over them. Given a set of data points $\{D_i\}$, we can write the probability for the parameters $\vec{w}$ as

$$P(\vec{w}|\{D_i\}) = \int\ldots\int P(\vec{w},\{\alpha_i\}|\{D_i\})\,d\alpha_1\ldots d\alpha_N, \tag{3.13}$$

where N is the total number of measurements. Bayes' theorem allows us to write

$$P(\vec{w},\{\alpha_i\}|\{D_i\}) = \frac{P(\{D_i\}|\vec{w},\{\alpha_i\})\,P(\vec{w},\{\alpha_i\})}{P(D_1,\ldots,D_N)} \tag{3.14}$$

and

$$P(\vec{w},\{\alpha_i\}) = P(\vec{w}|\{\alpha_i\})\,P(\{\alpha_i\}). \tag{3.15}$$

As in [126] we assume:

$$P(\{D_i\}|\vec{w},\{\alpha_i\}) = P(D_1|\vec{w},\alpha_1)\ldots P(D_N|\vec{w},\alpha_N), \tag{3.16a}$$

$$P(\vec{w}|\{\alpha_i\}) = \text{constant}, \tag{3.16b}$$

$$P(\{\alpha_i\}) = P(\alpha_1)\ldots P(\alpha_N). \tag{3.16c}$$

Thus far the formalism is fairly general and it contains two unspecified functions: probability distributions for both data points and HPs. In this work we will assume uniform priors for HPs ($P(\alpha_i) = 1$) and that errors never become smaller than their reported value ($\alpha_i \in [0,1]$).[2] A low posterior value of the HP indicates that the point has less weight within the fit. This may indicate the presence of systematic

[2]We have examined the more general case of an improper Jeffrey's prior (allowing decreasing as well as increasing error bars). This works well when many data points are associated to the same HP so that the χ^2 never vanishes. But when each data point has its own associated HP then the model curve can pass through that data point so that $\chi_i^2 = 0$. In this case the likelihood grows without bounds as $\alpha_i \to 0$, in other words the HP-marginalised likelihood is singular when at least one of the points has $\chi^2 = 0$ as can also be seen from Eq. (16) in [126].

effects or the requirement for better modelling. With these assumptions Eq. (3.13) now becomes:

$$P(\vec{w}, \{D_i\}) = \frac{P(D_1|\vec{w}) \dots P(D_N|\vec{w})}{P(D_1, \dots, D_N)}, \tag{3.17}$$

where

$$P(D_i|\vec{w}) \equiv \int_0^1 P(D_i|\vec{w}, \alpha_i)\, d\alpha_i. \tag{3.18}$$

The integral in Eq. (3.18) can be explicitly evaluated for the Gaussian HP likelihood (3.12), it gives, for each data point,

$$P(D_i|\vec{w}\,) = \tilde{N}_i \left(\frac{\mathrm{Erf}\left(\frac{\chi_i(\vec{w})}{\sqrt{2}}\right) - \sqrt{\frac{2}{\pi}}\chi_i(\vec{w}) \exp(-\chi_i^2(\vec{w})/2)}{\chi_i^3(\vec{w})} \right). \tag{3.19}$$

We can now rewrite Eq. (3.17) as

$$\ln P(\vec{w}, \{D_i\}) = \sum_i \ln \tilde{N}_i + \ln \tilde{\chi}_i^2, \tag{3.20}$$

where constant terms have been omitted and where

$$\tilde{\chi}_i^2(\chi_i^2(\vec{w})) \equiv \frac{\mathrm{Erf}\left(\frac{\chi_i(\vec{w})}{\sqrt{2}}\right) - \sqrt{\frac{2}{\pi}}\chi_i(\vec{w}) \exp(-\chi_i^2(\vec{w})/2)}{\chi_i^3(\vec{w})}. \tag{3.21}$$

One can easily obtain the most likely value for each HP by maximizing (3.12) w.r.t HPs at a given set of best fit parameters $\vec{w}$. We find that for each data point the effective HP is given by:

$$\alpha_i^{\mathrm{eff}} = 1, \quad \text{if} \quad \chi_i^2 \leq 1 \tag{3.22a}$$

$$\alpha_i^{\mathrm{eff}} = \frac{1}{\chi_i^2}, \quad \text{if} \quad \chi_i^2 > 1. \tag{3.22b}$$

We will now apply HPs to combine Cepheid variable measurements and determine the current expansion rate of the universe. We explore the parameter space $\vec{w}$ with the help of a Markov Chain Monte Carlo (MCMC) approach using flat priors if not specified differently.

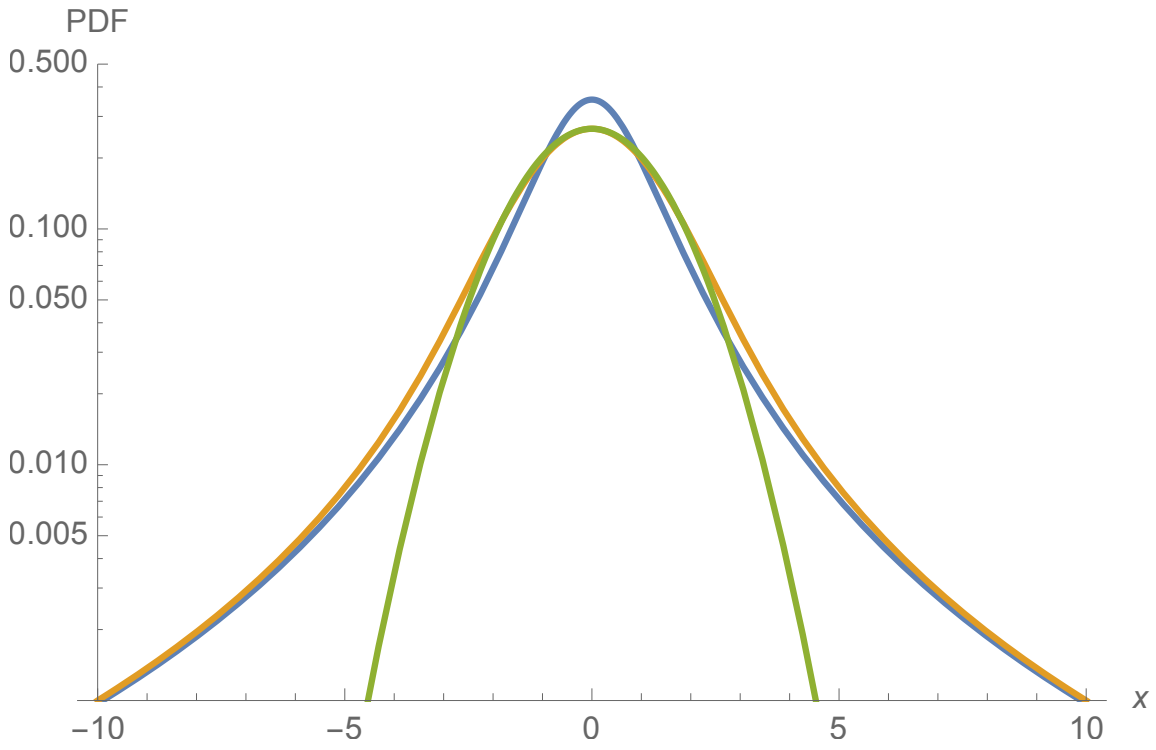

Fig. *3.1: The hyper-parameter-marginalized probability distribution function (pdf) of Eq. (3.19) in yellow. Close to the origin, $x = 0$, it is similar to a Gaussian pdf with $\sigma = (5/2)^{1/3}$ (green), except that its amplitude at the peak is 10.5% lower than a normalised Gaussian. Asymptotically for $|x| \to \infty$ it decreases as $1/x^3$ and looks like a student's t distribution with 2 degrees of freedom (blue), but the latter is narrower at small x.*

3.3 Applying hyper-parameters

In this section we will apply HPs to determine the Hubble constant. First, we will illustrate how the method works by fitting the period-luminosity relation of Cepheid variables in the LMC, the MW, and the megamaser system NGC4258. This will allow us to compare with results in [117]. Then, in Subsection 3.3.5 we determine H_0 with the Cepheid sample and SNe hosts in [78] (hereafter, R11). When this work was about to finish a new enlarged and improved sample of Cepheid variables and SNe hosts came out [32] (hereafter, R16); we determine the expansion rate of the universe with this data set in Subsection 3.3.6.

3.3.1 The LMC Cepheid variables

We start out our analysis by applying HPs to the set of 53 LMC Cepheid variables with H-band magnitudes, m_H, listed in Table 3 of [127] and V, I band magnitudes, m_V, m_I, listed in Table 4 of [128]. Following [32], we rely primarily on (near-infrared) NIR 'Wesenheit reddening-free' magnitudes, defined as

$$m_{W,i} = m_{H,i} - R\,(m_{V,i} - m_{I,i}), \tag{3.23}$$

where R is a constant defining the reddening law; in Subsections 3.3.1–3.3.5, where R11 data set is used, we set $R = 0.410$ as G. Efstathiou did [117]; when utilising R16 data set, we analyse the sensitivity of H_0 to variations in R. For the purpose of comparing with [117] we neglect for now metallicity dependence and fit the data with a period-luminosity relation

$$m_W^P = A + b_W(\log P - 1), \tag{3.24}$$

where $A = \mu_{0,\mathrm{LMC}} + M_W$ in notation of Eq. (3.9) and P is the period.[3] In order to apply HPs we define

$$\chi_i^{2,\mathrm{LMC}} = \frac{(m_{W,i} - m_W^P)^2}{\sigma_i^2 + \sigma_{\mathrm{int}}^{2,\mathrm{LMC}}}, \tag{3.25}$$

where σ_i is the observational error on $m_{W,i}$ and $\sigma_{\mathrm{int}}^{\mathrm{LMC}}$ is what is referred to as 'internal scatter' in [117]. The internal scatter is a common additional dispersion of the data points that is independent of the measurement error and due to variations in the physical mechanism behind the period-luminosity relation. As we do not know the

[3] We have dropped the label 'Cepheid' in the magnitudes for sake of simplicity.

LMC Cepheid variables				
Fit	A	b_W	$\sigma_{\rm int}^{\rm LMC}$	Period cut
a	12.570 (0.035)	−3.32 (0.10)	0.06	$10 < P < 60$
b	12.562 (0.016)	−3.30 (0.05)	0.06	$P < 60$
c	12.562 (0.016)	−3.31 (0.05)	0.06	$P < 205$
d	12.555 (0.019)	−3.24 (0.06)	0.12	$P < 205$

Tab. *3.1: Mean value and standard deviation (in brackets) for the parameters in the period-luminosity relation. Fits (a), (b), and (c) use HPs whereas fit (d) is a standard χ^2 minimization as done in [117].*

origin and magnitude of the internal scatter precisely, we add it as an additional random variable and marginalise over it.[4] More precisely, we sample in $\log \sigma_{\rm int}$ with a flat prior $\ln \sigma_{\rm int} \in [-3, -0.7]$. Maximizing

$$\ln P^{\rm LMC}(A, b_W, \{D_i\}) = \sum_i \ln \tilde{\chi}_i^2(\chi_i^{2,\rm LMC}) + \ln \tilde{N}_i^{\rm LMC}, \tag{3.26}$$

where

$$\tilde{N}_i^{\rm LMC} = \frac{1}{\sqrt{\sigma_i^2 + \sigma_{\rm int}^{2,\rm LMC}}}, \tag{3.27}$$

we find the best-fitting parameters of the period-luminosity relation (3.24). Table 3.1 shows results for different period cuts. Figure 3.2 shows the period-luminosity relation for the LMC Cepheid variables and the best fit of cases (c) and (d) in Table 3.1. We also show in Figure. 3.3 the posterior probability distribution function (pdf) of $\sigma_{\rm int}$ for the fits (c) and (d) of Table 3.1.

The LMC Cepheids are also treated as illustrative example in section 2 of [117]. This allows us to compare the approach used there, which does not use hyper-parameters, with the results found here. In our approach, the posterior mean values of A and b_W always lie in between the values given in [117]. They do also not depend significantly on the period cut (except that the error becomes larger for the most restrictive cut, $10 < P < 60$. We conclude that our treatment performs reasonably well when compared to the standard χ^2 approach, and also that the hyper-parameters allow to use all the available data without significant bias. We will investigate this conclusion further as we add more data.

In Figure 3.2 we also show the colour-coded effective HP value for all the data points in the LMC Cepheid sample, based on (3.22a) and (3.22b). Especially the lower

[4]Note that in R16 data set this intrinsic dispersion is already included in the total statistical uncertainty reported in their table 4 [32]. Consequently, when analysing the R16 data set we do not include an additional $\sigma_{\rm int}$.

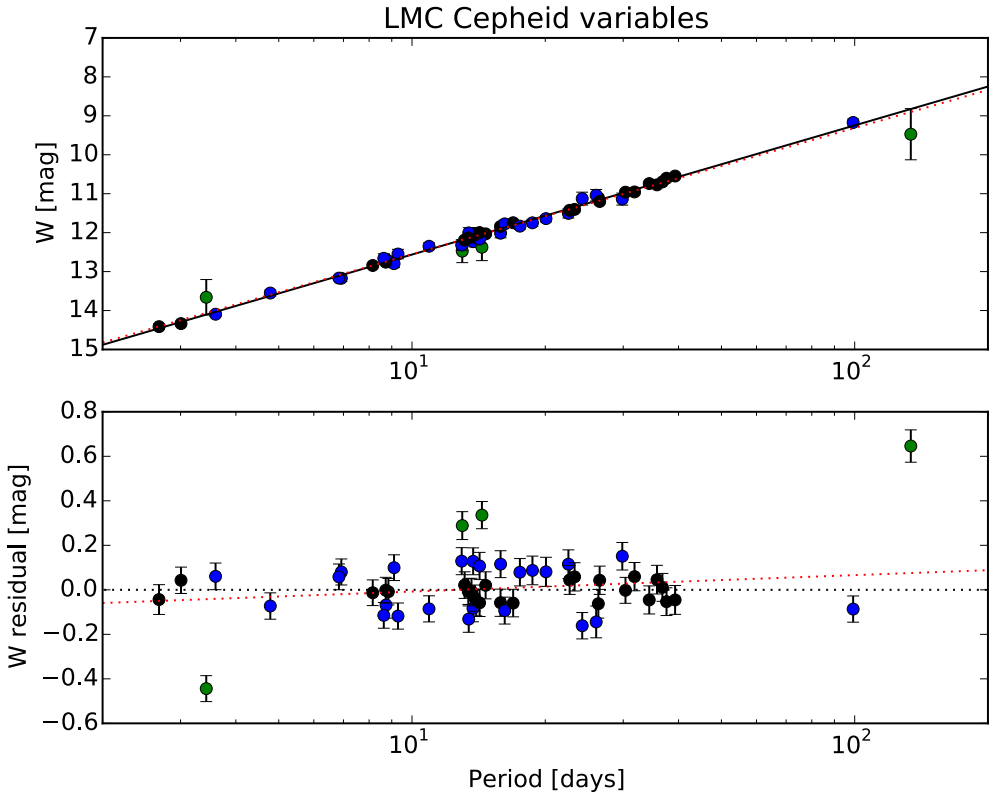

Fig. *3.2: Period-luminosity relation for the LMC Cepheid variables. The upper panel shows the best fit of both the case (c) (solid black line) and case (d) (red dotted line) in Table 3.1. Error bars have been rescaled with corresponding effective HPs which are colour-coded as follows: black if* $\alpha_{\text{eff}} = 1$*, blue if* $10^{-1} \leq \alpha_{\text{eff}} < 1$*, green if* $10^{-2} \leq \alpha_{\text{eff}} < 10^{-1}$*, red if* $10^{-3} \leq \alpha_{\text{eff}} < 10^{-2}$ *and yellow if* $\alpha_{\text{eff}} < 10^{-3}$*. Lower panel shows magnitude residuals; error bars are not rescaled and colours correspond to those in upper panel. The red dotted line in the lower panel shows the difference between the best fits in the upper panel.*

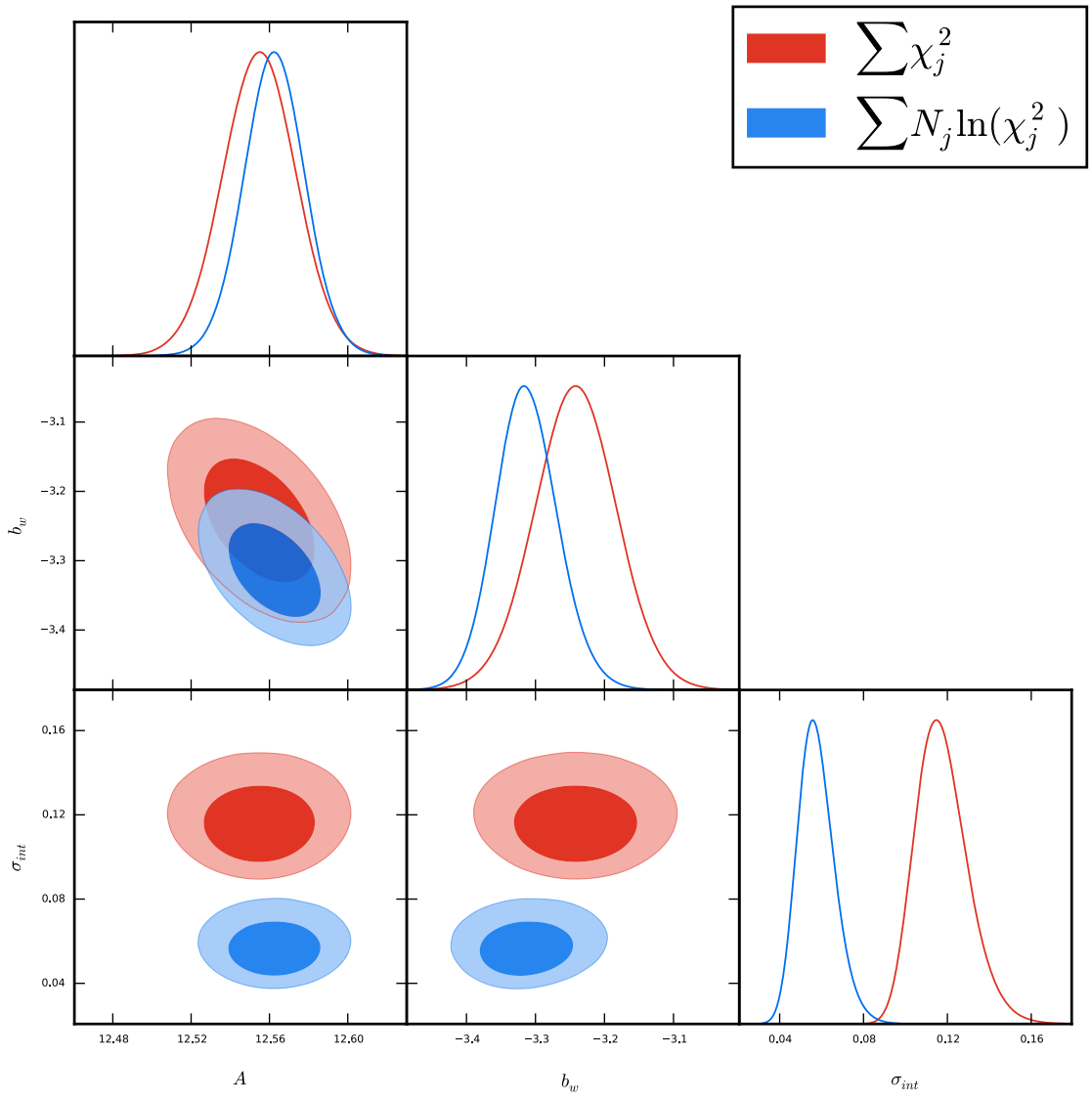

Fig. *3.3: Two- and 1D posteriors for the parameters in the period-luminosity relation. Red shows a standard* χ^2 *minimisation and blue uses HPs.*

panel, where we plot the residuals with respect to the best fit, shows clearly how outliers have a lower effective hyper- parameter and thus less weight. If instead we used a standard χ^2 fit to all of these points (i.e. without period cut) then the fit would be pulled towards a steeper slow (higher b_W) by the green points near the extrema of P as shown by the red dotted line in the upper panel of Figure 3.2.

The LMC distance modulus derived from observations of eclipsing binaries [129] is

$$\mu_{0,\mathrm{LMC}}^{\mathrm{obs}} = 18.49 \pm 0.05\,\mathrm{mag}, \tag{3.28}$$

that together with A from Table 3.1 for fit (c) gives a Cepheid zero point

$$M_W = -5.93 \pm 0.07\,\mathrm{mag}. \tag{3.29}$$

3.3.2 The MW Cepheid variables

Next, we discuss the set of 13 MW Cepheid stars with parallax measurements listed in Table 2 of [130] (eliminating Polaris as in [117] and correcting for Lutz-Kelker bias). We consider the MW Cepheids separately here because, as we will see, the MW data pushes the inferred value of H_0 to higher values, and it is thus important to check whether there is a reason to discard this data set or not.

The period-luminosity relation for those Cepheid stars is given by

$$M_W^P = M_W + b_W(\log P - 1), \tag{3.30}$$

where $Z_W = 0$ in Eq. (3.9), $M_W^P = m_W^P - \mu_\pi$ and μ_π is the distance modulus derived from parallaxes. Here we define

$$\chi_i^{2,\mathrm{MW}} = \frac{(M_{W,i} - M_W^P)^2}{\sigma_i^2 + \sigma_{\mathrm{int}}^{2,\mathrm{MW}}}, \tag{3.31}$$

where σ_i is the observational error on $M_{W,i}$ and $\sigma_{\mathrm{int}}^{\mathrm{MW}}$ is once more the internal dispersion (that we again include as a free, marginalised parameter as in the previous section on LMC Cepheids). Maximizing

$$\ln P^{\mathrm{MW}}(M_W, b_W, \{D_i\}) = \sum_i \ln \tilde{\chi}_i^2(\chi_i^{2,\mathrm{MW}}) + \ln \tilde{N}_i^{\mathrm{MW}}, \tag{3.32}$$

where

$$\tilde{N}_i^{\mathrm{MW}} = \frac{1}{\sqrt{\sigma_i^2 + \sigma_{\mathrm{int}}^{2,\mathrm{MW}}}}, \tag{3.33}$$

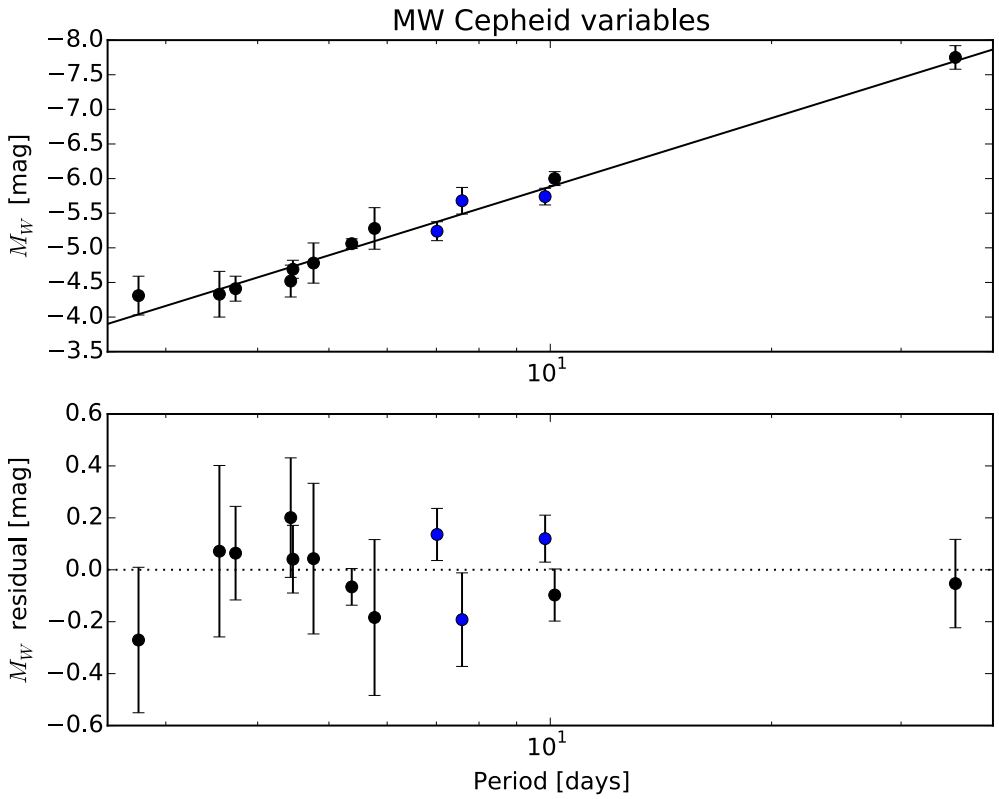

***Fig.** 3.4: Period-luminosity relation for the MW Cepheid variables. Upper panel shows the best fit. Error bars have been rescaled with corresponding effective HPs which are colour-coded as in Figure 3.2. Lower panel shows magnitude residuals; error bars are not rescaled and colours correspond to those in upper panel.*

we find the best-fitting parameters of the period-luminosity relation (3.30). They are

$$M_W = -5.88 \pm 0.07\,\text{mag}, \qquad b_W = -3.30 \pm 0.26, \qquad \sigma_{\text{int}}^{\text{MW}} = 0.02, \tag{3.34}$$

in good agreement with fits in Table 3.1 and with [117]. Figure 3.4 shows the period-luminosity relation for the MW Cepheid variables and best fit in Eq. (3.34).

The consistency in both the Cepheid zero point M_W (see Eq. (3.29)) and the slope b_W between the MW and the LMC Cepheid data, as well as the lack of marked outliers visible in Figure 3.4 provides no argument for excluding the MW data, at least based on the Cepheid stars. For this reason, we will include the MW data in our 'standard analysis' discussed in Section 3.3.5. We also note that our tests have

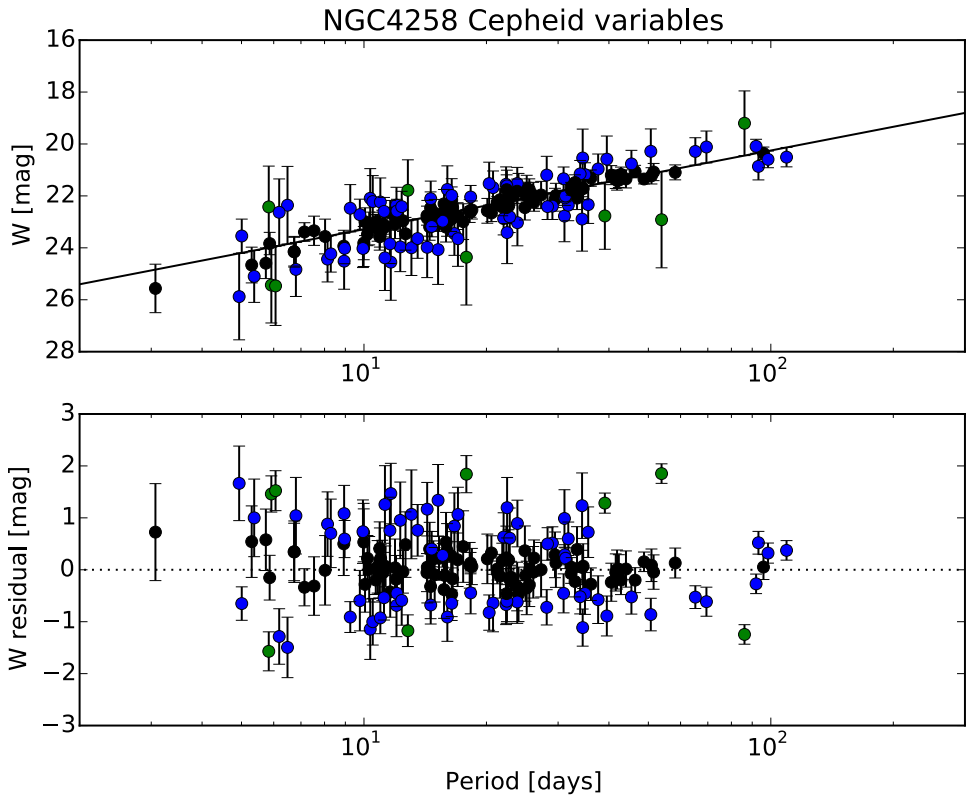

Fig. *3.5: Period-luminosity relation for the* NGC4258 *Cepheid variables. Upper panel shows the best fit; error bars have been rescaled with corresponding effective HPs which are colour-coded as in Figure 3.2. Lower panel shows magnitude residuals; error bars are not rescaled and colours correspond to those in upper panel.*

shown that the MW Cepheid data have no preference for a non-zero $\sigma_{\rm int}^{\rm MW}$, although including it does not change the fit significantly.

3.3.3 Cepheid variables in the megamaser system NGC4258

In this subsection we use the set of NGC4258 Cepheid variables included in the sample of [78] to fit the period-luminosity relation (3.24) setting now $A = \mu_{0,\rm NGC4258} + M_W$ and neglecting metallicity dependence. We find

$$A = 23.281 \pm 0.078\,\mathrm{mag}, \qquad b_W = -3.02 \pm 0.17, \qquad \sigma_{\rm int}^{\rm NGC4258} = 0.12. \tag{3.35}$$

Figure 3.5 shows period-luminosity relation and residuals for the NGC4258 Cepheid variables. Note that the slope b_W for the fit (3.35) is about 1.7σ away from the fit (c) in Table 3.1 and the internal scatter $\sigma_{\rm int}^{\rm NGC4258} = 2\sigma_{\rm int}^{\rm LMC}$. The NGC4258 distance modulus derived from the geometric maser distance estimate to the active galaxy NGC4258 [118] is

$$\mu_{0,\rm NGC4258}^{\rm obs} = 29.40 \pm 0.07\,\mathrm{mag}, \tag{3.36}$$

which leads to a Cepheid zero point $M_W = -6.12 \pm 0.15\,\mathrm{mag}$, a value about 1.6σ away from that in Eq. (3.34).[5] In the next subsection we explore the possibility of whether or not a metallicity dependence in the period-luminosity relation may improve the agreement in both the Cepheid zero point M_W and the slope b_W.

3.3.4 Metallicity dependence in the period-luminosity relation

Although the Leavitt law is expected to depend at some level on the Cepheids metal abundance [114], thus far we have neglected this effect. Here we will study how an additional degree of freedom in the period-luminosity relation (i.e., $Z_W \neq 0$) impacts the fits we have presented. As in [117] we consider a mean metallicity $\Delta\log[O/H] = 8.5$ for the LMC and $\Delta\log[O/H] = 8.9$ for the MW. For all other galaxies we use the metallicity reported in Table 2 of [78]; Cepheid variables in those galaxies have a mean metallicity close to that of the Cepheid variables in the MW, $\Delta\log[O/H] \approx 8.9$.

Table 3.2 shows the fit for the period-luminosity relation (3.9) (setting $A = \mu_{0,i} + M_W$) for all the galaxies containing Cepheid variables. We notice that the effect of metallicity on both the slope b_W and the Cepheid zero point M_W (through its dependence on A) is never greater than 4.3% (n3021) and 8.1% (NGC4028), respectively. The metallicity parameter Z_W is compatible with zero in all galaxies, its main effect being a small shift and a potentially large increase in the standard deviation of the Cepheid zero point due to a degeneracy between these two parameters (see Figure 3.6).

[5] The standardised candle method for type IIP SNe [131] provides an alternative determination of the NGC4258 distance modulus: $\mu_{0,\rm NGC4258} = 29.25 \pm 0.26\,\mathrm{mag}$. Although compatible with (3.36), it is much less precise and therefore we do not include it in our analysis.

Another point worth noting from the results in Table 3.2 is the fact that the slope b_W of about half of the host galaxies in the sample of [78] is less steep than the one of the LMC Cepheid variables, the shift being $\gtrsim 2\sigma$ for n4536, n4639, n1309, n4038, and n5584. This difference in the slope is however not improved by leaving more freedom in the metallicity dependence.

Cepheid zero point M_W derived from MW Cepheids is insensitive to including metallicity dependence in the period-luminosity relation. For both LMC and NGC4258 Cepheid variables, a small dependence on metallicity (strong prior) brings the Cepheid zero point in slightly better agreement with that derived from MW Cepheids. In particular, for the NGC4258 distance modulus in Eq. (3.36) and using a strong prior on Z_W, we obtain $M_W = -6.11 \pm 0.26$.

Because of the M_W-Z_W degeneracy, and since the additional freedom in the metallicity dependence does not bring the different Cepheid data sets into better agreement, we will use the 'strong' prior on the metallicity, $Z_W = 0 \pm 0.02$, as our default choice.

3.3.5 Determining H_0 with Bayesian hyper-parameters (R11 data set)

We have seen that the period-luminosity parameters independently derived from LMC, MW, and NGC4258 Cepheid variables are in good agreement. We therefore do not see any reason to discard any of the data sets when determining the Hubble constant with hyper-parameters. In this section we use the sample of Cepheid variables for the SNe Ia hosts from [78], the set of LMC Cepheid variables used in Section 3.3.1 and the set of MW Cepheid variables used in Section 3.3.2 (we call these three sets of Cepheid variables, R11 Cepheid sample or R11 data set). As for sources of calibration of the absolute distance scale, we utilize both the revised NGC4258 geometric maser distance from [118] and the distance to LMC derived from observations of eclipsing binaries from [129].

We use hyper-parameters for all Cepheid fits as there are outliers in most of the data sets (except possibly the MW Cepheids, see Figure 3.7). Although trigonometric parallaxes to MW Cepheid variables are one of most direct source of geometric calibration for those stars, we have included them with HPs because there exists an ongoing discussion about their parallax uncertainties (see Section 3.1.1 of [32]).

We find that the sample of SNe Ia hosts now shows inconsistencies (see Figure 3.8

Sample of Cepheid variables				
galaxy	A	b_W	Z_W	$\sigma_{\rm int}$
LMC	12.699 (2.139)	−3.31 (0.05)	−0.016 (0.252) $[W]$	0.06
LMC	12.562 (0.170)	−3.31 (0.05)	0.000 (0.020) $[S]$	0.06
MW	−5.88 (2.23)	−3.30 (0.26)	0.000 (0.250) $[W]$	0.02
MW	−5.88 (0.19)	−3.30 (0.26)	0.000 (0.020) $[S]$	0.02
NGC4258	25.175 (1.957)	−3.00 (0.17)	−0.214 (0.221) $[W]$	0.12
NGC4258	23.293 (0.193)	−3.02 (0.17)	−0.001 (0.020) $[S]$	0.12
n4536	24.620 (1.866)	−2.85 (0.17)	0.021 (0.214) $[W]$	0.07
n4536	24.803 (0.207)	−2.84 (0.17)	0.000 (0.020) $[S]$	0.07
n4639	26.572 (1.846)	−2.46 (0.42)	−0.147 (0.210) $[W]$	0.03
n4639	25.303 (0.302)	−2.49 (0.42)	−0.001 (0.020) $[S]$	0.04
n3982	26.591 (1.724)	−3.28 (0.42)	−0.083 (0.200) $[W]$	0.03
n3982	25.888 (0.283)	−3.27 (0.42)	0.000 (0.020) $[S]$	0.03
n3370	28.317 (1.696)	−2.99 (0.20)	−0.260 (0.196) $[W]$	0.02
n3370	26.098 (0.224)	−3.03 (0.20)	−0.003 (0.020) $[S]$	0.02
n3021	28.226 (1.983)	−2.86 (0.51)	−0.239 (0.231) $[W]$	0.03
n3021	26.211 (0.325)	−2.99 (0.50)	−0.002 (0.020) $[S]$	0.03
n1309	26.788 (2.032)	−2.09 (0.42)	−0.105 (0.225) $[W]$	0.03
n1309	25.857 (0.354)	−2.08 (0.42)	−0.000 (0.020) $[S]$	0.03
n4038	24.200 (2.171)	−2.47 (0.27)	0.092 (0.243) $[W]$	0.03
n4038	25.011 (0.291)	−2.45 (0.27)	0.000 (0.020) $[S]$	0.03
n5584	25.428 (1.782)	−2.83 (0.24)	0.013 (0.204) $[W]$	0.03
n5584	25.541 (0.240)	−2.83 (0.24)	0.000 (0.020) $[S]$	0.03

Tab. *3.2: Mean values and standard deviation (in brackets) in the period-luminosity relation parameters for the sample of Cepheid variables used in this work. The period range used to fit the data is the same used in fit (c) of Table 3.1 ($P < 205$ days). $[W]$ stands for a Gaussian prior with mean $\overline{Z_W} = 0$ and standard deviation $\sigma_{Z_W} = 0.25$. $[S]$ stands for a Gaussian prior with $\overline{Z_W} = 0$ and $\sigma_{Z_W} = 0.02$. The internal dispersion for each galaxy is shown in the last column.*

and Table 3.5 below), so we include it also with hyper-parameters in our analysis. We have however included a few cases where SNe Ia magnitudes are analysed without HPs; in these cases SNe Ia measured magnitudes are assumed being drawn from a Gaussian distribution.

We include the available distance modulus to both NGC4258 and LMC with hyper-parameters (especially when combining these two anchor distances in the same fit), but run a few cases including them without HPs. Note that the inclusion of these distance calibrators in our approach can be viewed as the introduction of priors on $\mu_{0,\mathrm{NGC4258}}$ and $\mu_{0,\mathrm{LMC}}$. For anchor distances and SNe Ia magnitudes we then assume a Gaussian HP likelihood as in Eq. (3.19).

Hence, in order to find the best-fitting parameters $\vec{w}$ we maximize

$$\ln P(\vec{w}, \{D_i\}) = \ln P^{\mathrm{Cepheid}} + \ln P^{\mathrm{SNe\,Ia}} + \ln P^{\mathrm{Anchors}}. \tag{3.37}$$

For Cepheid variables we have, as in Subsections 3.3.1–3.3.4,

$$\ln P^{\mathrm{Cepheid}} = \sum_{ij} \ln \tilde{\chi}^2(\chi^{2,\mathrm{Cepheid}}_{ij}) + \ln \tilde{N}^{\mathrm{Cepheid}}_{ij}, \tag{3.38a}$$

where

$$\tilde{N}^{\mathrm{Cepheid}}_{ij} = \frac{1}{\sqrt{\sigma^2_{e,ij} + \sigma^2_{\mathrm{int},i}}}, \tag{3.38b}$$

$$\chi^{2,\mathrm{Cepheid}}_{ij} = \frac{(m_{W,ij} - m^P_{W,i,j})^2}{\sigma^2_{e,ij} + \sigma^2_{\mathrm{int},i}}, \tag{3.38c}$$

and the Cepheid magnitude is modelled as in Eq. (3.9) for the passband W and utilizing the 'Wesenheit reddening-free' magnitudes

$$m_{W,ij} = m_{H,ij} - R\,(m_{V,ij} - m_{I,ij}) \tag{3.38d}$$

and $\sigma_{\mathrm{int},i}$, as in Subsections 3.3.1-3.3.4, is the internal scatter for the ith galaxy (i.e., ith = LMC, MW, NGC4258, ...), j being the index of the Cepheid belonging to the ith galaxy. In this section we set $R = 0.410$, but when analysing the R16 data set we study the impact of different values of R in our analysis.

For SNe Ia magnitudes we use the likelihood

$$\ln P^{\mathrm{SNe\,Ia}} = \sum_i \ln \tilde{\chi}^2(\chi^{2,\mathrm{SNe\,Ia}}_i) + \ln \tilde{N}^{\mathrm{SNe\,Ia}}_i - \frac{(a_V^{\mathrm{R11}} - a_V)^2}{2\sigma^2_{a_V}} - \frac{\ln(2\pi\sigma^2_{a_V})}{2} - \frac{(a_{\mathrm{cal}})^2}{2\sigma^2_{a_{\mathrm{cal}}}} - \frac{\ln(2\pi\sigma^2_{a_{\mathrm{cal}}})}{2} \tag{3.39}$$

where

$$\tilde{N}_i^{\text{SNe Ia}} = \frac{1}{\sqrt{\sigma_i^2}}, \tag{3.40}$$

$$\chi_i^{2,\text{SNe Ia}} = \frac{(m_{X,i}^0 - m_{X,i}^{\text{th}})^2}{\sigma_i^2}, \tag{3.41}$$

$$m_{X,i}^{\text{th}} = \mu_{0,i} + 5\log H_0 - 25 - 5a_X \tag{3.42}$$

is the SNe Ia apparent magnitude (3.8), and both $m_{X,i}^0$ and σ_i are taken from the table 3 in [78]. Here a_X is the intercept of the SNe Ia magnitude-redshift relation, and [78] gives its value as $a_V = 0.697 \pm 0.00201$ (using wavelength V). We call the mean value in the above expression for the likelihood $a_V^{\text{R11}} = 0.697$ and the uncertainty $\sigma_{a_V} = 0.00201$, and assume that a_V itself has a Gaussian pdf given by these quantities. If we were dealing with Gaussian likelihood for $m_{V,i}^0$ then we could marginalize analytically over a_V, which would then contribute a fully correlated error to the covariance matrix for the $m_{V,i}^0$. But as we are using HPs, we instead add a_V as an explicit (nuisance) parameter in Eq. (3.39), together with its associated Gaussian likelihood, and sample from it numerically. Similarly, we take into account the calibration error, $\sigma_{a_{\text{cal}}}$, between the ground based and the WFC3 photometry by introducing a nuisance parameter a_{cal}. We assume it has a Gaussian pdf with zero mean and $\sigma_{a_{\text{cal}}} = 0.04$.

Finally, motivated by the inconsistencies of distance anchors found by G. Efstathiou in [117], we include the available distance modulus as

$$\ln P^{\text{Anchors}} = \sum_i \ln \tilde{\chi}^2\left(\chi_i^{2,\text{Anchors}}\right) + \ln \tilde{N}_i^{\text{Anchors}}, \tag{3.43}$$

where

$$\tilde{N}_i^{\text{Anchors}} = \frac{1}{\sqrt{\sigma_i^2}}, \tag{3.44}$$

$$\chi_i^{2,\text{Anchors}} = \frac{(\mu_{0,i} - \mu_{0,i}^{\text{obs}})^2}{\sigma_i^2}, \tag{3.45}$$

where $i = \text{LMC}$, NGC4258 and $\mu_{0,\text{LMC}}^{\text{obs}}$ and $\mu_{0,\text{NGC4258}}^{\text{obs}}$ are given by Eqs. (3.28) and (3.36) respectively.

At this point we have assembled all ingredients necessary to determine the Hubble parameter, using HPs rather than a rejection algorithm. We have performed several variants (see Table 3.3) of the analysis that are shown in Table 3.4.

Fit	α^{Cepheid}	$\alpha^{\text{SNe Ia}}$	α^{Anchors}	P	R	σ_{Z_W}	$\sigma_{\text{int},i}$	$\sigma_{\text{int}}^{\text{LMC}}$	$\sigma_{\text{int}}^{\text{MW}}$	CS	$\mu_{0,\text{NGC4258}}^{\text{obs}}$	$\mu_{0,\text{LMC}}^{\text{obs}}$	$\mu_{0,\text{M31}}^{\text{obs}}$	MW
1	Y	Y	Y	205	0.410	-	V	V	-	R11	[118]	-	-	-
2	Y	Y	Y	60	0.410	-	V	V	-	R11	[118]	-	-	-
3	Y	Y	Y	205	0.410	0.02	V	V	-	R11	[118]	-	-	-
4	Y	Y	N	205	0.410	0.02	V	V	-	R11	[118]	-	-	-
5	Y	Y	Y	60	0.410	0.02	V	V	-	R11	[118]	-	-	-
6	Y	Y	N	60	0.410	0.02	V	V	-	R11	[118]	-	-	-
7	Y	Y	Y	205	0.410	-	V	V	-	R11	-	[129]	-	-
8	Y	Y	Y	60	0.410	-	V	V	-	R11	-	[129]	-	-
9	Y	Y	Y	205	0.410	0.02	V	V	-	R11	-	[129]	-	-
10	Y	Y	N	205	0.410	0.02	V	V	-	R11	-	[129]	-	-
11	Y	Y	Y	60	0.410	0.02	V	V	-	R11	-	[129]	-	-
12	Y	Y	N	60	0.410	0.02	V	V	-	R11	-	[129]	-	-
13	Y	Y	-	205	0.410	-	V	V	V	R11	-	-	-	[130]
14	Y	Y	-	60	0.410	-	V	V	V	R11	-	-	-	[130]
15	Y	Y	-	205	0.410	0.02	V	V	V	R11	-	-	-	[130]
16	Y	Y	-	60	0.410	0.02	V	V	V	R11	-	-	-	[130]
17	Y	Y	Y	205	0.410	-	V	V	-	R11	[118]	[129]	-	-
18	Y	Y	Y	60	0.410	-	V	V	-	R11	[118]	[129]	-	-
19	Y	Y	Y	205	0.410	0.02	V	V	-	R11	[118]	[129]	-	-
20	Y	Y	Y	60	0.410	0.02	V	V	-	R11	[118]	[129]	-	-
21	Y	Y	Y	205	0.410	-	V	V	V	R11	[118]	-	-	[130]
22	Y	Y	Y	60	0.410	-	V	V	V	R11	[118]	-	-	[130]
23	Y	Y	Y	205	0.410	0.02	V	V	V	R11	[118]	-	-	[130]
24	Y	Y	Y	60	0.410	0.02	V	V	V	R11	[118]	-	-	[130]
25	Y	Y	Y	205	0.410	-	V	V	V	R11	-	[129]	-	[130]
26	Y	Y	Y	60	0.410	-	V	V	V	R11	-	[129]	-	[130]
27	Y	Y	Y	205	0.410	0.02	V	V	V	R11	-	[129]	-	[130]
28	Y	Y	Y	60	0.410	0.02	V	V	V	R11	-	[129]	-	[130]
29	Y	Y	Y	205	0.410	0.02	V	V	V	R11	[118]	[129]	-	[130]
31	Y	N	Y	205	0.410	0.02	V	V	V	R11	[118]	[129]	-	[130]
32	Y	Y	N	205	0.410	0.02	V	V	V	R11	[118]	[129]	-	[130]
33	Y	N	N	205	0.410	0.02	V	V	V	R11	[118]	[129]	-	[130]
34	Y	Y	Y	60	0.410	0.02	V	V	V	R11	[118]	[129]	-	[130]
35	Y	N	N	60	0.410	0.02	0.30	0.113	0.10	R11	[118]	[129]	-	[130]
36	Y	Y	Y	205	0.410	0.25	V	V	V	R11	[118]	[129]	-	[130]
37	Y	Y	Y	60	0.410	0.25	V	V	V	R11	[118]	[129]	-	[130]
38	Y	Y	Y	205	0.410	-	V	V	V	R11	[118]	[129]	-	[130]
39	Y	Y	Y	60	0.410	-	V	V	V	R11	[118]	[129]	-	[130]
40	Y	Y	Y	205	0.31	0.25	-	-	-	R16	[32]	[129]	[32]	[32]
41	Y	Y	Y	205	0.31	0.02	-	-	-	R16	[32]	[129]	[32]	[32]
42	Y	Y	Y	205	0.35	0.25	-	-	-	R16	[32]	[129]	[32]	[32]
43	Y	Y	Y	205	0.39	0.25	-	-	-	R16	[32]	[129]	[32]	[32]
44	Y	Y	Y	205	0.47	0.25	-	-	-	R16	[32]	[129]	[32]	[32]
45	Y	Y	Y	205	0.35	0.02	-	-	-	R16	[32]	[129]	[32]	[32]
46	Y	Y	Y	205	0.39	0.02	-	-	-	R16	[32]	[129]	[32]	[32]
47	Y	Y	Y	205	0.47	0.02	-	-	-	R16	[32]	[129]	[32]	[32]
48	Y	Y	Y	60	0.31	0.25	-	-	-	R16	[32]	[129]	[32]	[32]
49	Y	Y	Y	60	0.31	0.02	-	-	-	R16	[32]	[129]	[32]	[32]
50	Y	Y	Y	60	0.35	0.25	-	-	-	R16	[32]	[129]	[32]	[32]
51	Y	Y	Y	60	0.39	0.25	-	-	-	R16	[32]	[129]	[32]	[32]
52	Y	Y	Y	60	0.47	0.25	-	-	-	R16	[32]	[129]	[32]	[32]
53	Y	Y	Y	60	0.35	0.02	-	-	-	R16	[32]	[129]	[32]	[32]
54	Y	Y	Y	60	0.39	0.02	-	-	-	R16	[32]	[129]	[32]	[32]
55	Y	Y	Y	60	0.47	0.02	-	-	-	R16	[32]	[129]	[32]	[32]

Tab. *3.3:* α^{Cepheid}*: Cepheid stars included with HPs.* $\alpha^{\text{SNe Ia}}$*:* SNe Ia *magnitudes included with HPs.* α^{Anchors}*: distance moduli of anchors included with HPs; '-' stands for no distance moduli included in the fit. In columns* 2–4 *'Y' stands for 'Yes' and 'N' stands for 'No'. P: upper period cutoff. R: reddening law.* σ_{Z_W}*: standard deviation of the Gaussian prior on the metallicity parameter* Z_W*; '-' stands for a flat, wide prior.* $\sigma_{\text{int},i}$*: internal dispersion for* SNe Ia *hosts; 'V' stands for varying and marginalised; when the numerical value is given it means fixed internal dispersion was used; '-' stands for no internal dispersion included in the fit.* $\sigma_{\text{int}}^{\text{LMC}}$*:* LMC *internal dispersion.* $\sigma_{\text{int}}^{\text{MW}}$*:* MW *internal dispersion. CS: Cepheid sample. Columns* $\mu_{0,\text{NGC4258}}^{\text{obs}}$*,* $\mu_{0,\text{LMC}}^{\text{obs}}$*, and* $\mu_{0,\text{M31}}^{\text{obs}}$ *indicate the references from which these quantities were taken; '-' means that the data was not used in the fit.* MW *refers to the reference for* MW *Cepheid stars; '-' means that the data was not used in the fit.*

Fit	H_0	M_W	b_W	Z_W	$\|\|\alpha^{\text{Cepheid}}\|\|$	$\|\|\alpha^{\text{SNe Ia}}\|\|$	$\|\|\alpha^{\text{Anchors}}\|\|$
1	71.2 (5.4)	−3.54 (1.24)	−3.15 (0.06)	−0.285 (0.140)	0.72	0.81	1
2	72.5 (5.4)	−1.99 (1.33)	−3.25 (0.05)	−0.457 (0.150)	0.72	0.82	1
3	71.1 (5.5)	−6.00 (0.22)	−3.17 (0.06)	−0.006 (0.020)	0.72	0.73	1
4	70.8 (4.2)	−6.01 (0.19)	−3.17 (0.06)	−0.006 (0.020)	0.72	0.72	-
5	72.7 (5.7)	−5.94 (0.22)	−3.26 (0.05)	−0.008 (0.020)	0.72	0.71	1
6	72.1 (4.2)	−5.95 (0.19)	−3.26 (0.05)	−0.008 (0.020)	0.72	0.75	-
7	71.3 (4.9)	−3.48 (1.16)	−3.15 (0.06)	−0.291 (0.136)	0.72	0.77	1
8	70.1 (4.5)	−2.11 (1.28)	−3.26 (0.05)	−0.450 (0.150)	0.72	0.87	1
9	74.5 (4.9)	−5.90 (0.20)	−3.17 (0.06)	−0.006 (0.020)	0.72	0.75	1
10	74.4 (4.0)	−5.90 (0.18)	−3.17 (0.06)	−0.006 (0.020)	0.72	0.78	-
11	75.0 (4.8)	−5.87 (0.20)	−3.26 (0.05)	−0.008 (0.020)	0.72	0.78	1
12	74.7 (3.8)	−5.87 (0.18)	−3.26 (0.05)	−0.008 (0.020)	0.72	0.73	-
13	78.1 (4.4)	−3.44 (1.25)	−3.16 (0.06)	−0.272 (0.140)	0.73	0.82	-
14	78.3 (4.2)	−2.08 (1.19)	−3.26 (0.05)	−0.426 (0.133)	0.72	0.72	-
15	77.4 (4.4)	−5.81 (0.18)	−3.17 (0.06)	−0.006 (0.020)	0.72	0.64	-
16	77.1 (4.1)	−5.81 (0.18)	−3.26 (0.05)	−0.008 (0.020)	0.74	0.77	-
17	71.1 (4.0)	−3.47 (1.10)	−3.15 (0.06)	−0.293 (0.128)	0.72	0.81	1
18	71.2 (4.0)	−2.27 (1.16)	−3.25 (0.05)	−0.428 (0.135)	0.71	0.68	1
19	73.0 (4.1)	−5.93 (0.18)	−3.17 (0.06)	−0.007 (0.020)	0.72	0.75	0.84
20	73.9 (4.0)	−5.89 (0.18)	−3.26 (0.05)	−0.008 (0.020)	0.72	0.78	1
21	76.4 (4.2)	−3.44 (1.27)	−3.18 (0.06)	−0.277 (0.142)	0.73	0.80	0.21
22	76.9 (4.0)	−2.13 (1.27)	−3.27 (0.04)	−0.425 (0.143)	0.73	0.70	0.48
23	75.6 (4.2)	−5.85 (0.18)	−3.20 (0.05)	−0.006 (0.020)	0.72	0.73	0.41
24	75.8 (3.9)	−5.84 (0.18)	−3.27 (0.04)	−0.008 (0.020)	0.72	0.74	0.35
25	76.0 (4.2)	−4.33 (1.16)	−3.18 (0.06)	−0.178 (0.131)	0.73	0.75	0.12
26	76.2 (4.1)	−3.10 (1.31)	−3.27 (0.05)	−0.318 (0.147)	0.72	0.83	0.11
27	76.0 (4.0)	−5.86 (0.18)	−3.19 (0.05)	−0.004 (0.020)	0.72	0.74	0.60
28	76.1 (3.8)	−5.84 (0.18)	−3.27 (0.04)	−0.007 (0.020)	0.72	0.71	1
29	75.0 (3.9)	−5.88 (0.18)	−3.20 (0.05)	−0.005 (0.020)	0.72	0.74	0.79
31	73.2 (2.5)	−5.89 (0.18)	−3.19 (0.05)	−0.004 (0.020)	0.72	-	0.92
32	74.1 (3.7)	−5.89 (0.18)	−3.21 (0.05)	−0.005 (0.020)	0.72	0.81	-
33	72.4 (2.2)	−5.90 (0.17)	−3.20 (0.05)	−0.004 (0.020)	0.71	-	-
34	75.4 (3.7)	−5.85 (0.18)	−3.27 (0.04)	−0.007 (0.020)	0.72	0.73	0.64
35	72.6 (2.4)	−5.90 (0.18)	−3.26 (0.07)	−0.005 (0.020)	0.99	-	-
36	74.7 (3.9)	−4.68 (0.97)	−3.20 (0.05)	−0.141 (0.110)	0.72	0.76	0.55
37	75.2 (3.8)	−3.62 (1.07)	−3.27 (0.04)	−0.261 (0.121)	0.72	0.71	0.60
38	74.7 (3.9)	−4.34 (1.11)	−3.20 (0.05)	−0.179 (0.125)	0.72	0.79	0.64
39	75.2 (3.9)	−3.09 (1.39)	−3.27 (0.04)	−0.321 (0.157)	0.72	0.76	0.58
40	74.20 (2.18)	−4.98 (0.90)	−3.23 (0.02)	−0.09 (0.10)	0.86	0.85	0.95
41	74.21 (2.16)	−5.78 (0.17)	−3.23 (0.02)	−0.00 (0.02)	0.86	0.86	0.81
42	74.11 (2.17)	−4.89 (0.84)	−3.24 (0.01)	−0.11 (0.10)	0.86	0.80	1
43	73.88 (2.15)	−4.96 (0.69)	−3.25 (0.01)	−0.11 (0.08)	0.86	0.80	1
44	73.76 (2.16)	−5.08 (0.93)	−3.28 (0.01)	−0.10 (0.11)	0.85	0.79	0.78
45	74.06 (2.12)	−5.83 (0.18)	−3.24 (0.01)	−0.00 (0.02)	0.86	0.80	0.76
46	73.91 (2.13)	−5.86 (0.17)	−3.25 (0.01)	−0.01 (0.02)	0.86	0.74	0.78
47	73.76 (2.09)	−5.94 (0.18)	−3.28 (0.01)	−0.00 (0.02)	0.86	0.81	0.78
48	73.98 (2.21)	−4.92 (0.71)	−3.23 (0.02)	−0.10 (0.08)	0.86	0.83	0.62
49	73.83 (2.17)	−5.79 (0.18)	−3.23 (0.02)	−0.00 (0.02)	0.86	0.88	0.86
50	74.03 (2.24)	−5.00 (1.01)	−3.24 (0.02)	−0.10 (0.11)	0.86	0.78	0.80
51	73.72 (2.19)	−4.79 (0.75)	−3.25 (0.02)	−0.13 (0.09)	0.86	0.81	0.62
52	73.70 (2.20)	−4.83 (0.92)	−3.28 (0.02)	−0.13 (0.10)	0.86	0.79	0.9
53	73.78 (2.18)	−5.81 (0.18)	−3.24 (0.02)	−0.01 (0.02)	0.86	0.84	0.75
54	73.71 (2.19)	−5.86 (0.18)	−3.25 (0.02)	−0.00 (0.02)	0.86	0.79	0.78
55	73.49 (2.20)	−5.95 (0.18)	−3.28 (0.02)	−0.00 (0.02)	0.86	0.79	0.79

Tab. *3.4: Constraints for fits in Table 3.3. Numbers in brackets indicate the standard deviation.*

Distance parameters					
Host	SN Ia	$\mu_{0,i} - \mu_{0,4258}$	$\mu_{0,i}$ best	α_{eff}	$\sigma_{\text{int},i}$
n4536	SN 1981B	1.620 (0.071)	30.91 (0.08)	1	0.1
n4639	SN 1990N	2.325 (0.085)	31.61 (0.09)	1	0.03
n3370	SN 1994ae	2.805 (0.063)	32.09 (0.07)	1	0.02
n3982	SN 1998aq	2.502 (0.081)	31.79 (0.08)	0.23	0.03
n3021	SN 1995al	2.964 (0.110)	32.25 (0.11)	1	0.03
n1309	SN 2002fk	3.255 (0.079)	32.54 (0.08)	0.28	0.03
n5584	SN 2007af	2.399 (0.064)	31.69 (0.07)	0.43	0.03
n4038	SN 2007sr	2.304 (0.099)	31.59 (0.11)	1	0.03

Tab. *3.5: Distance parameters for the* SNe Ia *hosts corresponding to our primary fit for the R11 data set (fit* (29)*). Numbers in brackets indicate the standard deviation. The last two columns correspond to the effective HP for each* SNe Ia *host and the corresponding internal scatter, respectively.*

Discarding data might hinder our understanding of the physical basis behind the incompatibility of data sets (if any) [119], and for that reason our best estimate of the universe's expansion rate uses no period cut-off in the sample of Cepheid stars and includes the three distance calibrators. As discussed in Subsection 3.3.1, we see no significant trend for the LMC Cepheid stars that would justify a tighter cut. We also performed the analysis for a tighter period cut-off, and report the results in Table 3.4 (see details of fits (29), (34), (36)–(39) in Table 3.3). The difference between the two is never larger than $0.5\,\text{kms}^{-1}\text{Mpc}^{-1}$ in H_0 (with a somewhat larger impact on b_W).

Fits (29), (34), (36)–(39) use different prior on the metallicity parameter Z_W (e.g., Gaussian with zero mean, or top-hat around zero). As discussed in Subsection 3.3.4, this question remains open. The combined Cepheid data used here is unable to significantly constrain Z_W, instead we find a strong degeneracy with M_W (see Figure 3.6). From a Bayesian model comparison point of view, there is no significant preference for specific prior or $Z_W = 0$. However, looking again at Table 3.4 we see that also this choice has no significant impact on H_0. From theoretical arguments there is probably some dependence on metallicity, but as we cannot strongly constrain it, we have decided to use the 'strong' prior of [117], $Z_W = 0 \pm 0.02$, as our baseline model.

Fit (29) uses both strong prior on Z_W and no period cut-off in the Cepheid variables sample; it also includes Cepheid stars, SNe Ia magnitudes, and distance moduli to anchor galaxies with HPs. We show the parameter constraints for this case in Figure 3.6. The resulting constraint on the Hubble parameter, which is also our primary fit

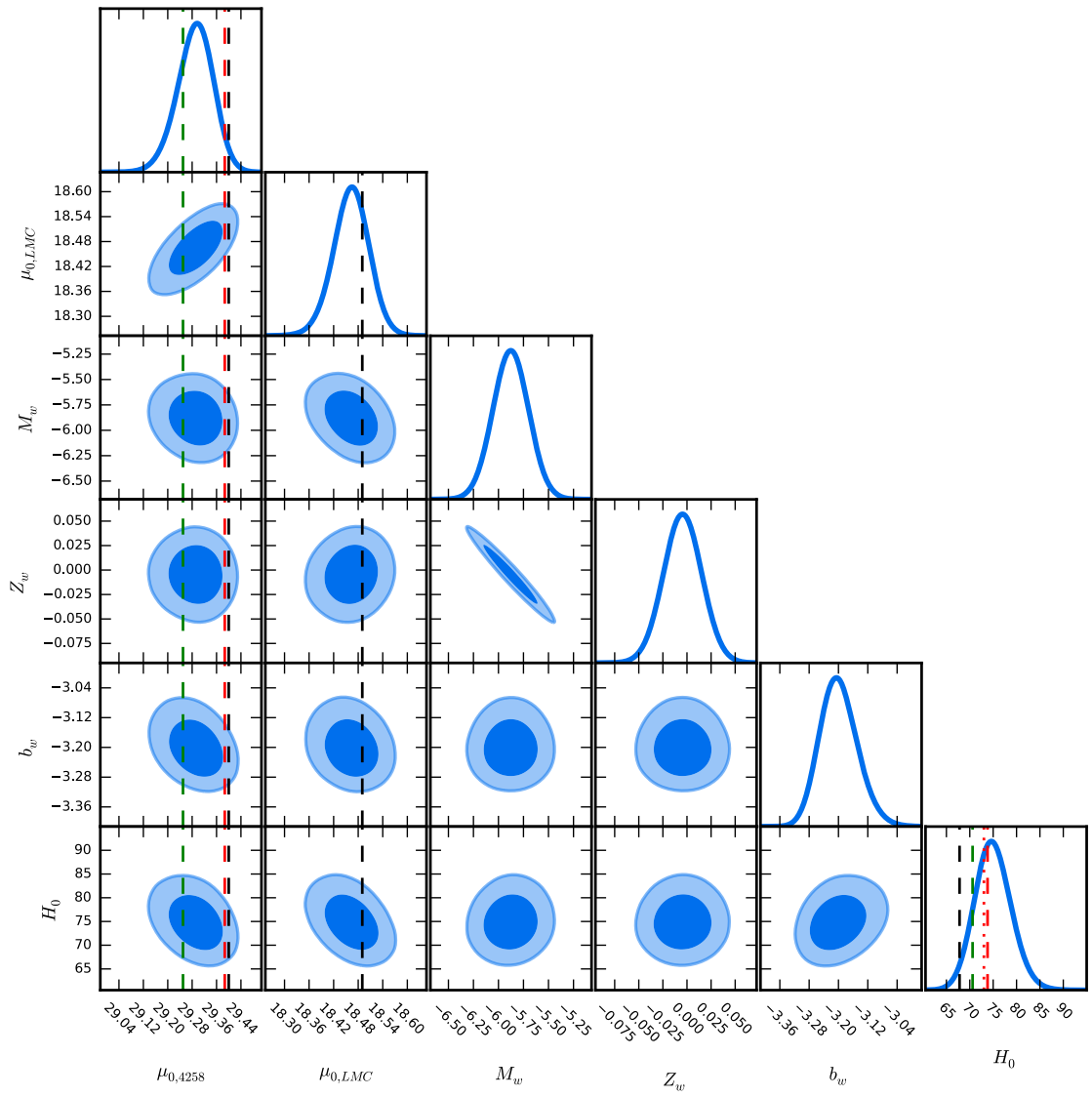

Fig. *3.6: Posterior constraints for fit* (29) *in Table 3.4. Green, red and black vertical dashed lines in* $\mu_{0,4258}$ *column indicate* NGC4258 *distance modulus from [131], [32] and [118], respectively. Black dashed vertical line in* $\mu_{0,\mathrm{LMC}}$ *column shows LMC distance modulus from [129]. Black, green, and red dashed vertical lines in* H_0 *column respectively indicate the values derived by the Planck collaboration for the base six-parameter* ΛCDM *model [21], Efstathiou's value [117] used by Planck collaboration as a prior, and the* 3% *measurement reported by [78]; the red dotted vertical line indicates the best estimate from the analysis in [32].*

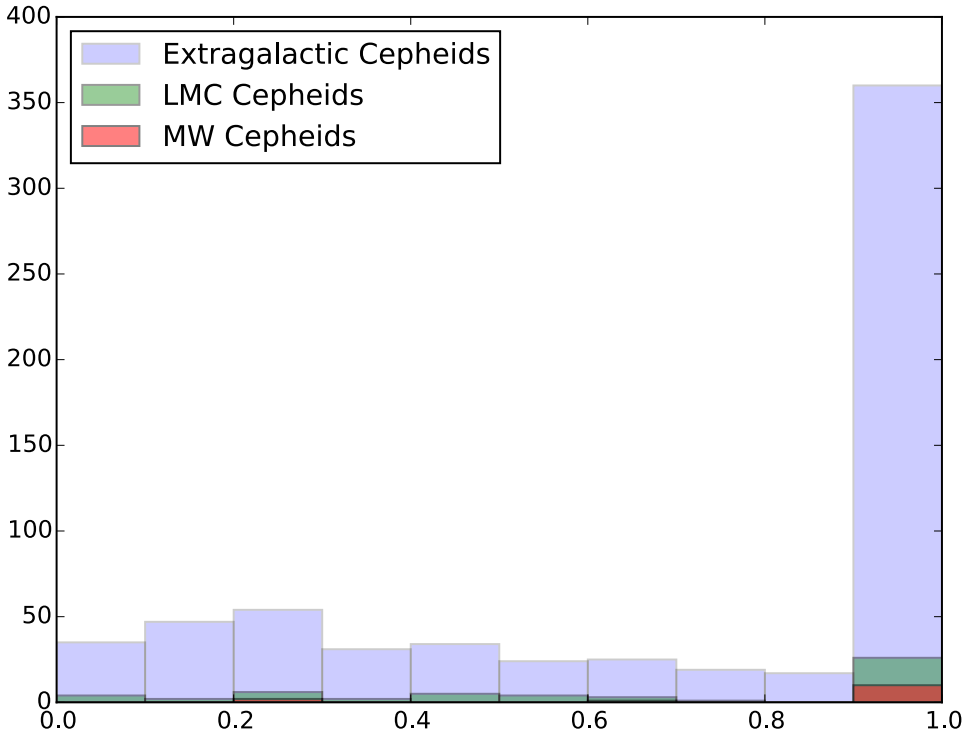

Fig. *3.7: Effective hyper-parameters for the R11 Cepheid sample used in fit* (29)*. From the 646 Cepheid variables in the sample of [78], 348 have* $\alpha_{\rm eff} = 1$*, 263* $10^{-1} \leq \alpha_{\rm eff} < 1$*, 34* $10^{-2} \leq \alpha_{\rm eff} < 10^{-1}$*, and 1* $10^{-3} \leq \alpha_{\rm eff} < 10^{-2}$*. For the 53 LMC Cepheid variables, the analysis outputs 25* $\alpha_{\rm eff} = 1$*, 24* $10^{-1} \leq \alpha_{\rm eff} < 1$*, 4* $10^{-2} \leq \alpha_{\rm eff} < 10^{-1}$*. Finally, as for the analysis shown in Figure 3.4, the set of MW Cepheid variables has 10 stars with* $\alpha_{\rm eff} = 1$ *and 3 stars with* $10^{-1} \leq \alpha_{\rm eff} < 1$*. Overall,* 23% *of the MW Cepheids are down-weighted. The fraction raises* 46% *for R11 Cepheids in [78]. As for the LMC Cepheid variables, the analysis down-weights* 53% *of the stars.*

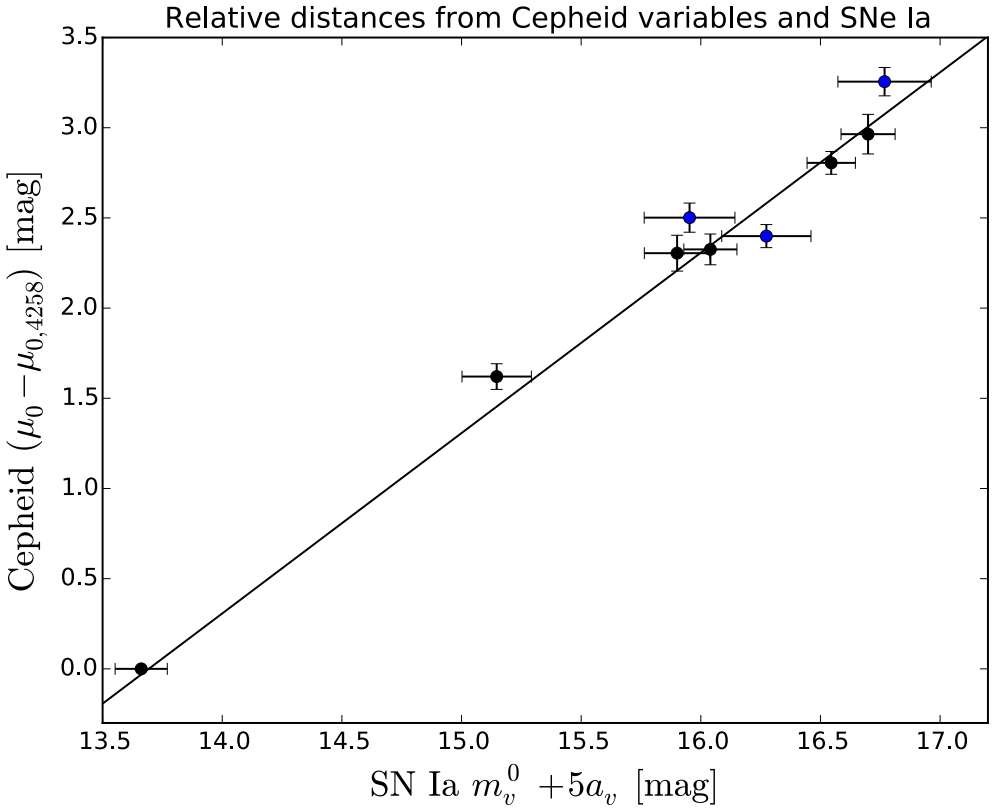

Fig. *3.8: Relative distances from Cepheids and* SNe Ia*. We plot the peak apparent visual magnitudes of each* SNe Ia *(from Table 3 in [78]) with error bars rescaled by HPs (colour code is the same as in Figure 3.2) against the relative distances between hosts determined from fit* (29) *in Table 3.4. The solid line shows the corresponding best fit. The first point on the left corresponds to the expected reddening-free, peak magnitude of an* SNe Ia *appearing in the megamaser system* NGC4258 *which is derived from the fit* (29)*.*

of the expansion rate derived with the R11 sample of Cepheids, is

$$H_0 = 75.0 \pm 3.9\,\mathrm{km\,s^{-1}\,Mpc^{-1}}\,. \tag{3.46}$$

The dashed vertical lines in the 1D marginal posterior for H_0 of Figure 3.6 give (from left to right) the mean values of the Planck ΛCDM determination of H_0 ($67.8 \pm 0.9\,\mathrm{km\,s^{-1}\,Mpc^{-1}}$ from Planck temperature and lensing data [21]) and of the analyses of [117] ($70.6 \pm 3.3\,\mathrm{km\,s^{-1}\,Mpc^{-1}}$), [32] ($73.0 \pm 1.8\,\mathrm{km\,s^{-1}\,Mpc^{-1}}$), and [78] ($73.8 \pm 2.4\,\mathrm{km\,s^{-1}\,Mpc^{-1}}$). Our result here agrees best with the latter two (although our width is somewhat larger due to the use of hyper-parameters), but even the Planck value lies within our 95% credible interval. Note that as the HP likelihoods have wide wings and are very non-Gaussian, one could expect that also the likelihood for H_0 is very non-Gaussian. We found however that it is relatively close to a normal pdf.

Figure 3.7 shows a histogram for HPs in the sample of Cepheid variables used in our primary fit for the R11 data set (fit (29)). Whereas in [78] about 20% of the Cepheids are rejected by the Chauvenet's criterion (this would be equivalent to $\alpha_{\mathrm{eff}} = 0$ in our analysis), our analysis finds that about 46% of the Cepheid variables in [78] are down-weighted ($\alpha_{\mathrm{eff}} < 1$). The analysis in [32], also using a Chauvenet's criterion, finds an outlier fraction of 2% in a larger sample of Cepheid variables. In the next Subsection 3.3.6 we analyse this enlarged Cepheid sample by using HPs.

Figure 3.8 and Table 3.5 bring about the presence of possible outliers among the sample of SNe Ia hosts, thus justifying our use of HPs in the apparent visual magnitudes of each SNe Ia. This could be a hint of unaccounted systematics in the light-curve fits for those SNe Ia. Note that [32] has used a different light-curve fitting algorithm (SALT-II) to that utilised in [78] (MLCS2k2) finding no evidence for any of their 19 SNe Ia hosts to be an outlier. We will investigate this claim further in Subsection 3.3.6.

As mentioned above, the available distance moduli are included with HPs in our primary fit. The resulting effective HPs are: $\alpha^{\mathrm{eff}}_{\mathrm{LMC}} = 1$, $\alpha^{\mathrm{eff}}_{\mathrm{NGC4258}} = 0.58$. This shows that the geometric maser distance estimate to the active galaxy NGC4258 from [118] is slightly down-weighted in our analysis. As can be seen from the vertical, red, dashed line in Figure 3.6, the revised maser distance to NGC4258 from [32] is now closer to our 68% confidence region.

We also note that it is not least the difference between the supernova distance [131] and the maser distance [118] to NGC4258 that limits the precision on H_0 as can be seen from the vertical dashed lines for $\mu_{0,\mathrm{NGC4258}}$ in Figure 3.6. Especially the very

recent supernova distance prefers a higher H_0 as can be seen from the marginal 2D likelihood for $\mu_{0,\mathrm{NGC4258}}$ and H_0. An improvement in the anchors is thus important for future improvements in the direct determination of the local expansion rate H_0.

The last three columns in Table 3.4 show the normalised weight of jth kind of data defined as

$$||\alpha^j|| \equiv \frac{\sum_{i=1}^{K_j} \alpha_{i,j}}{K_j}, \tag{3.47}$$

where $\alpha_{i,j}$ denotes ith HP of kind of data j (j = Cepheid, SNe Ia, Anchors), and K_j stands for the number of objects of kind j. When the normalised weight of a given kind of data equals one, it means their reported error bars are all 'reliable' in the sense they do not require to be rescaled by HPs (given the best fit parameters). In other words, it gives an idea of how compatible both model and data are. We could also use these normalised weights to asses compatibility of the whole data set. For our particular case of three kinds of data, and as long as $\sum_j ||\alpha^j|| \neq 3$, the most compatible fit would be that with $max(\sum_j ||\alpha^j||)$. This happens to be the case for our primary fit (29), for which $\sum_j ||\alpha^j|| = 2.25$.

We have also considered variants of the general analysis presented thus far in this section including the three anchor distances available in the R11 data set. They correspond to fits (31)–(33) and fit (35) in Tables 3.3–3.4. Differently to fit (34), where we use internal scatter nuisance parameters σ_{int} for each galaxy containing Cepheid variables, in fit (35) we have fixed those nuisance parameters to the values in fit (75) of [117] and used HPs only for the Cepheid variables. The constraints output by two analyses agree within error bars; in particular, the values of H_0 agree pretty well. Because the role of σ_{int} is a common increment of the error bars in the magnitudes of Cepheid variables, a big internal scatter σ_{int} would mean no Cepheid variables down-weighted by HPs. In fit (35) the internal scatter is five times greater than in fit (34) and as a result all HPs equal 1. The use of HPs does not weaken the quality of the data as a whole, instead the method is able to identify and down-weight only inconsistent data points.

In Figure 3.9 we show our primary fit (29) along with fits (31)–(33) and different measurements of the Hubble parameter which use three anchor distances done by other groups. The precision of the measurement using HPs depends on the assumptions made (e.g., including SNe Ia with HPs, including distance moduli with HPs). The normalised weights for fits including three anchor distances do not suggest dropping the HPs in any kind of data as they never equal 1 in the fits (29), (34), (36)–(39). Our primary fit and its variants agree with previous measurements [78] and [117]

using the same data set. While analyses using HPs agree with both most recent direct local measurement of H_0 [32] and the WMAP 2009 indirect determination [132], our result is in disagreement with the indirect determination by the Planck collaboration [21]. The fact that three different analyses converge at similar values for H_0 nicely shows that the result is robust.

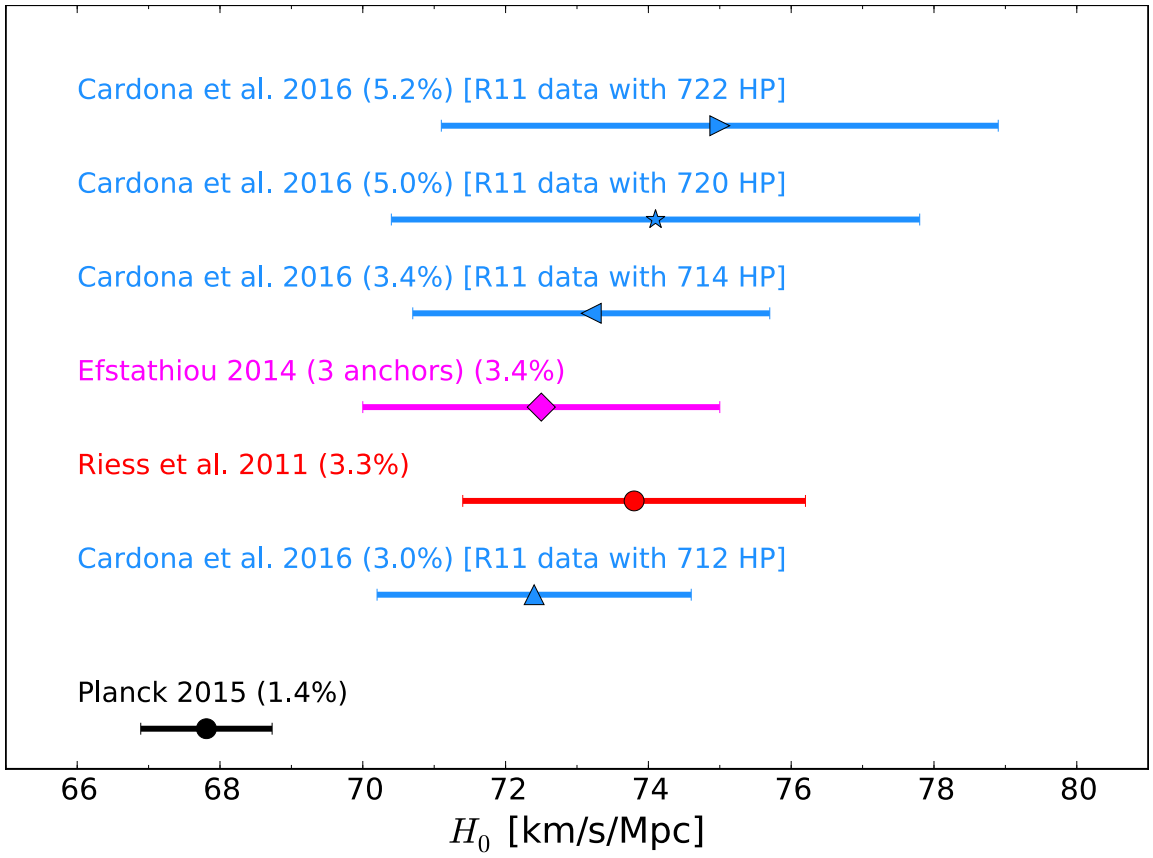

Fig. *3.9: Different determinations of the Hubble constant. Blue and black show the indirect determinations by the WMAP team [132] and by the Planck collaboration [21], respectively. Direct measurements using NGC 4258 distance modulus, LMC distance modulus and MW Cepheid variables as anchor distances are shown in red, magenta, green, and dodger blue. Red corresponds to measurement by Riess et al. [78], magenta shows Efstathiou's measurement [117] which uses a* 60 *days period cut, green is the Riess et al. measurement [32], and dodger blue points correspond from top to bottom to fits* (29),(31),(32), (33) *in Table 3.4.*

Although we have found no reasons to discard any of the data sets, we have carried out analyses simultaneously including only one or two anchors. The cases shown in Table 3.3–3.4 suggest that i) inclusion of MW Cepheid variables drives H_0 to higher values independently of both prior on the metallicity parameter and period cut for period-luminosity relation ii) a strong prior on the metallicity parameter when in-

cluding distance modulus to LMC also drives H_0 to higher values. Figure 3.10 shows the most compatible fits according to the corresponding normalised weights.

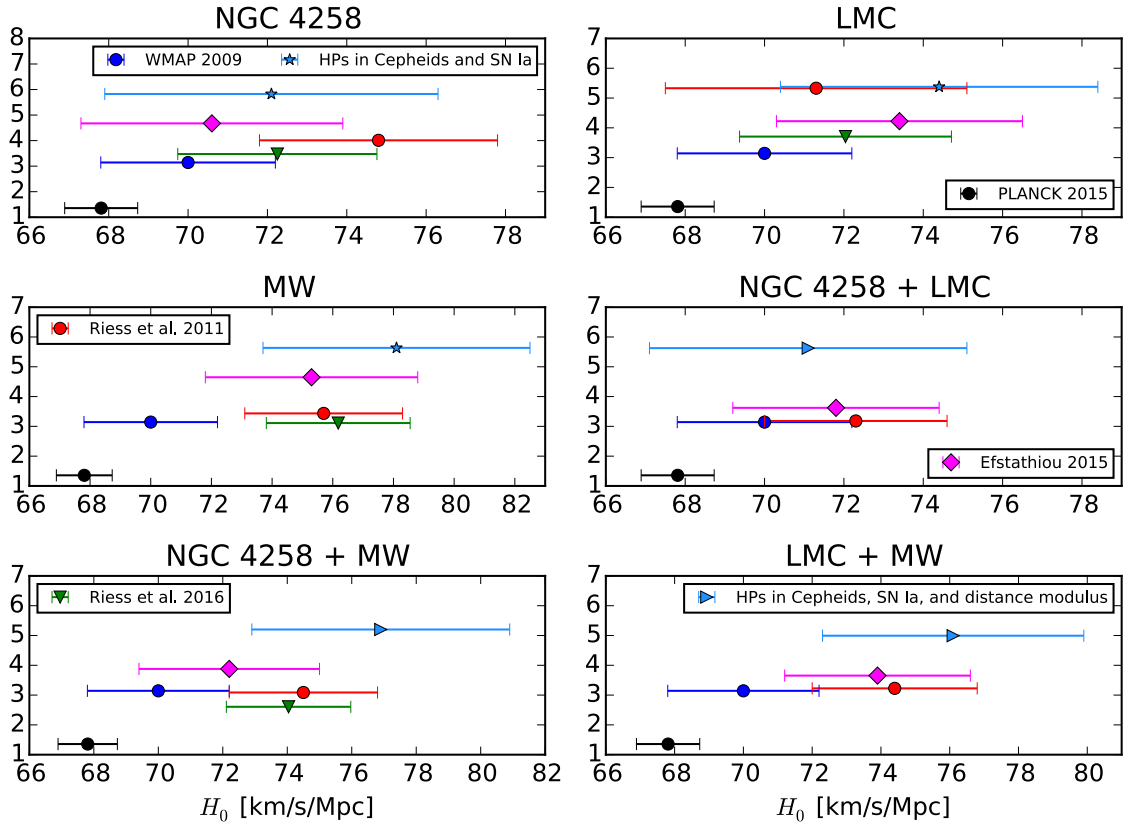

Fig. *3.10: Different measurements of the Hubble constant using different combinations of anchor distances. Colours and symbols are as in Figure 3.9. Fits shown are:* (6) NGC4258, (10) LMC, (13) MW, (17) NGC4258 + LMC, (22) NGC4258 + MW, (28) LMC + MW.

3.3.6 Determining H_0 with Bayesian hyper-parameters (R16 data set)

We now apply HPs to measure the current expansion rate of the universe H_0 by using the R16 data set. It comprehends: a larger sample of Cepheids in the LMC (775 compared to 53 in R11 data set); 2 new *HST*-based trigonometric parallaxes for the MW Cepheids (a total of 15 MW parallaxes, taking into account the 13 included in the R11 data set); 11 new SNe Ia host galaxies (for a total of 19, taking

into account the 8 in the R11 data set); *HST* observations of 372 Cepheid variables in M31 (which were not in the R11 Cepheid sample); the possibility to use M31 as an anchor distance taking advantage of the two detached eclipsing binaries based distances to M31; NGC4258 Cepheid stars observed with the same instrument as those in the 19 SNe Ia host galaxies, thus reducing the cross-instrument zeropoint errors.

As we have seen in the previous sections, we do not find any evident reason to discard any of the data sets. In this section we will utilise all available Cepheid data in the R16 data set (including MW Cepheid stars) along with LMC distance modulus in Eq. (3.28), M31 distance modulus [32] given by

$$\mu_{0,\mathrm{M31}}^{\mathrm{obs}} = 24.36 \pm 0.08\,\mathrm{mag}, \tag{3.48}$$

and the improved NGC4258 distance modulus [32]

$$\mu_{0,\mathrm{NGC4258}}^{\mathrm{obs}} = 29.387 \pm 0.0568\,\mathrm{mag}. \tag{3.49}$$

We have performed the same analysis as for primary best fit with the R11 data set (fit (29) in Table 3.3), but also some variants to estimate the impact of used reddening law, period cut-off, metallicity dependence in the R11 data set. Different variants are specified in fits (40)–(55) of Table 3.3 and the corresponding constraints are shown in Table 3.4. Changes on the Hubble constant H_0 due to different reddening law (different R in Eq. (3.23)) range from 0.33 up to $0.45\,\mathrm{km\,s^{-1}\,Mpc^{-1}}$. Differences in the period cut-off produce changes on H_0 ranging from 0.06 to $0.38\,\mathrm{km\,s^{-1}\,Mpc^{-1}}$. Allowing for a strong or weak metallicity dependence in the period-luminosity relation we find differences in H_0 which range from 0 to $0.25\,\mathrm{km\,s^{-1}\,Mpc^{-1}}$. The standard deviation for measurements of H_0 in fits (40)–(55) is $\sigma_{\mathrm{syst}} = 0.20\,\mathrm{km\,s^{-1}\,Mpc^{-1}}$ which we consider as a systematic error due to changes on the reddening law, period cut-off, and metallicity dependence.

According to the normalised weight criterion discussed in Section 3.3.5, the most compatible fits for the R16 data set are fits (40), (42)–(43) having $\sum_j ||\alpha^j|| = 2.66$ which is higher than that for the R11 data set. For sake of comparison with the best estimate of H_0 in [32], we choose fit (43), which uses the same reddening law as best estimate in [32], as our primary fit for the R16 data set. Adding in quadrature the statistical error (quoted in Table 3.4) and the systematic error estimated above, we find

$$H_0 = 73.88 \pm 2.16\,\mathrm{km\,s^{-1}\,Mpc^{-1}}, \tag{3.50}$$

which is a 2.9% measurement of the Hubble constant. The small change in the uncertainty due to inclusion of systematic error shows that HPs are already taking into account most of this contribution to the error budget.

Figures 3.11–3.14 show the period-luminosity relation for the best fit of our primary fit (43) for Cepheid stars in galaxies LMC, MW, NGC4258, and M31. Note that no outliers were released in the R16 data set. We find, however, that several Cepheid stars which passed the 2.7σ outlier rejection criterion in the analysis of [32] are down-weighted in our approach. In Figure 3.15 we show a histogram for HPs in the R16 Cepheid sample used in fit (43). Differently to our analysis in Section 3.3.5, which used the R11 data set and included outliers (Cepheid stars which did not pass the 2.5σ outlier criterion in [78]), there are no Cepheid stars with $\alpha_{\text{eff}} < 0.1$ in the analysis in this section using the R16 data set. Although in the Riess et al. analysis [32] outliers were not released, we find that about 30% of the Cepheid stars in the R16 sample are down-weighted in our analysis. The fraction of down-weighted Cepheid variables was about 46% in our analysis using the R11 data set. Note that the normalised weight for Cepheids increases from 0.72 for the primary best fit (29) (with the R11 data set) to 0.86 for the primary best fit (43) (with the R16 data set), which shows that there is an improvement in the compatibility of the data set and therefore a reduction in the fraction of down-weighted stars.

Riess et al. [32] used the SALT-II light curve fitter and found no outlier in the SNe Ia hosts. Although we cannot claim the opposite, we do find that some of the SNe Ia are down-weighted in our analysis. In Figure 3.16 we compare the SNe Ia distances to the approximate, independent Cepheid distances from our primary fit (43). In Table 3.6 we show the distance parameters and the HPs for the SNe Ia hosts in the R16 data set. The down-weighted SNe Ia hosts might indicate the presence of unaccounted (or underestimated) systematics in the R16 data set. Whereas our analysis in Section 3.3.5 using the R11 data set showed that three out of the eight host galaxies are down-weighted in the fit, the primary fit (43) using the R16 data set down-weights eight SNe Ia host galaxies. The two host galaxies n3982 and n5584 are down-weighted in both fit (29) and fit (43). From Table 3.4 we see that the normalised weight for SNe Ia data is slightly higher for the R16 data set (0.80) in comparison to the R11 data set (0.74). This indicates an improvement in the compatibility of this kind of data in the R16 sample.

If we compare the normalised weight of anchors in Table 3.4 for fits (29) and (43) (0.79 and 1, respectively), we can also see an improvement in the compatibility of this kind of data in the R16 data set. Although this would suggest not to include distance moduli with HPs in the fit (since the HP Gaussian likelihood would add

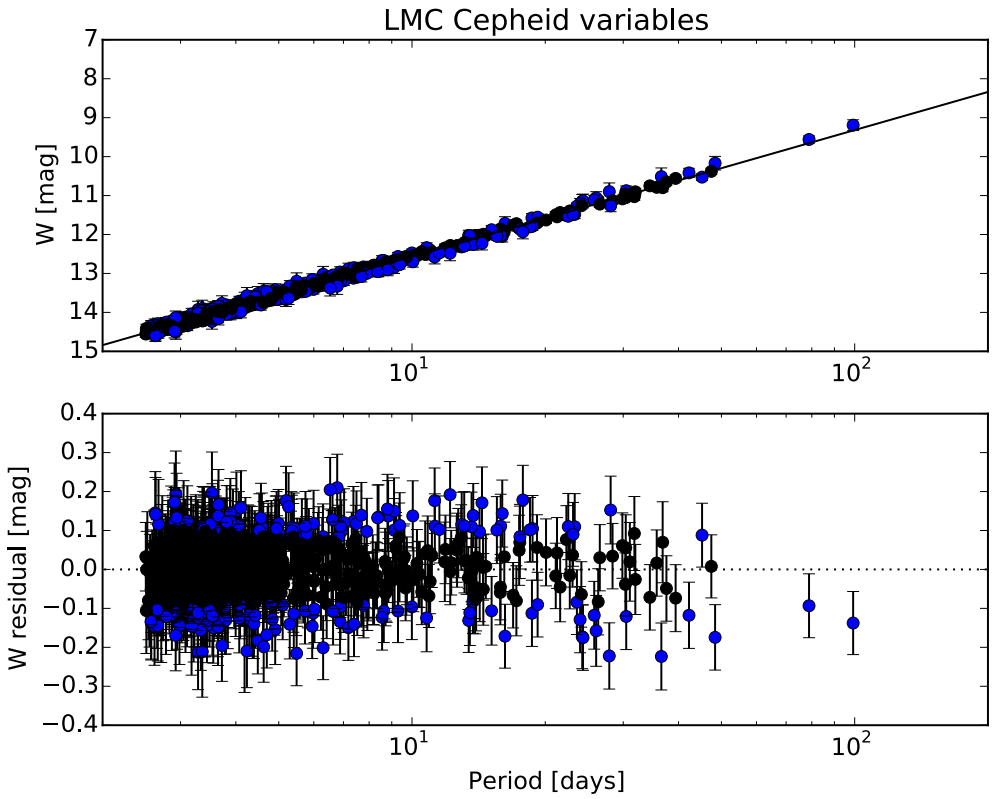

Fig. *3.11: Period-luminosity relation (upper panel) and magnitude residuals for the* LMC *Cepheid variables in the R16 data set. The solid line shows the best fit of fit* (43)*. In the upper panel we rescale error bars with HPs, in the lower panel we do not. Data are colour-coded as explained in Figure 3.2.*

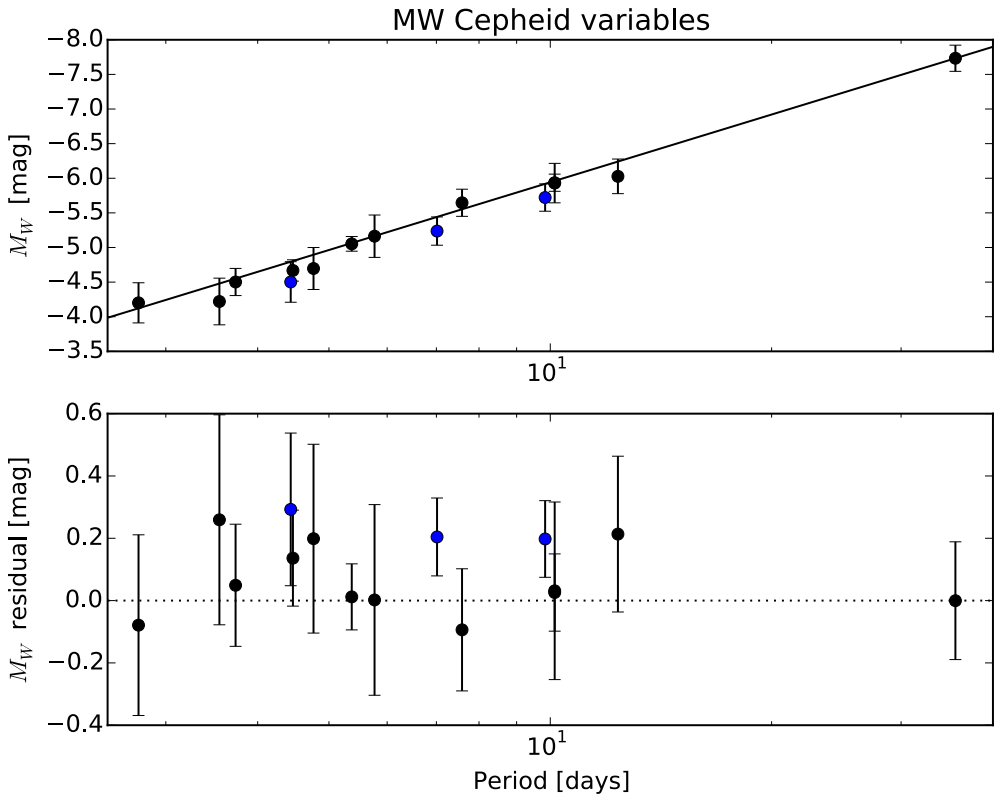

Fig. *3.12: Period-luminosity relation (upper panel) and magnitude residuals for the* MW *Cepheid variables in the R16 data set. The solid line shows the best fit of fit* (43)*. In the upper panel we rescale error bars with HPs, in the lower panel we do not. Data are colour-coded as explained in Figure 3.2.*

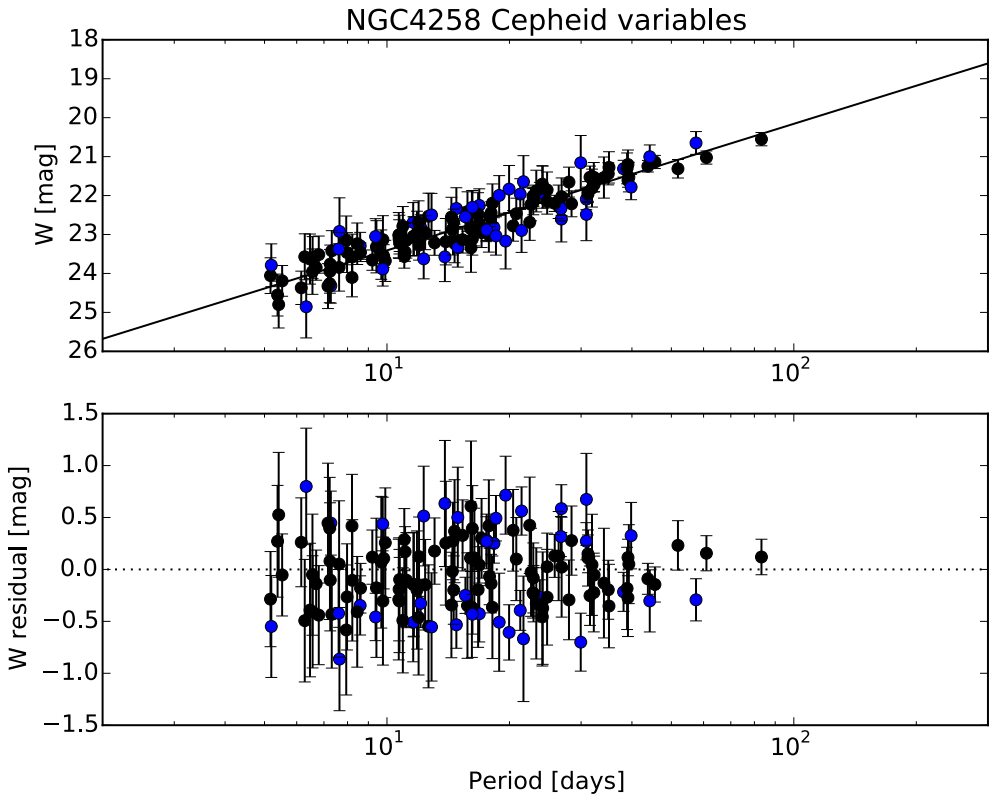

Fig. *3.13: Period-luminosity relation (upper panel) and magnitude residuals for the* NGC4258 *Cepheid variables in the R16 data set. The solid line shows the best fit of fit* (43)*. In the upper panel we rescale error bars with HPs, in the lower panel we do not. Data are colour-coded as explained in Figure 3.2.*

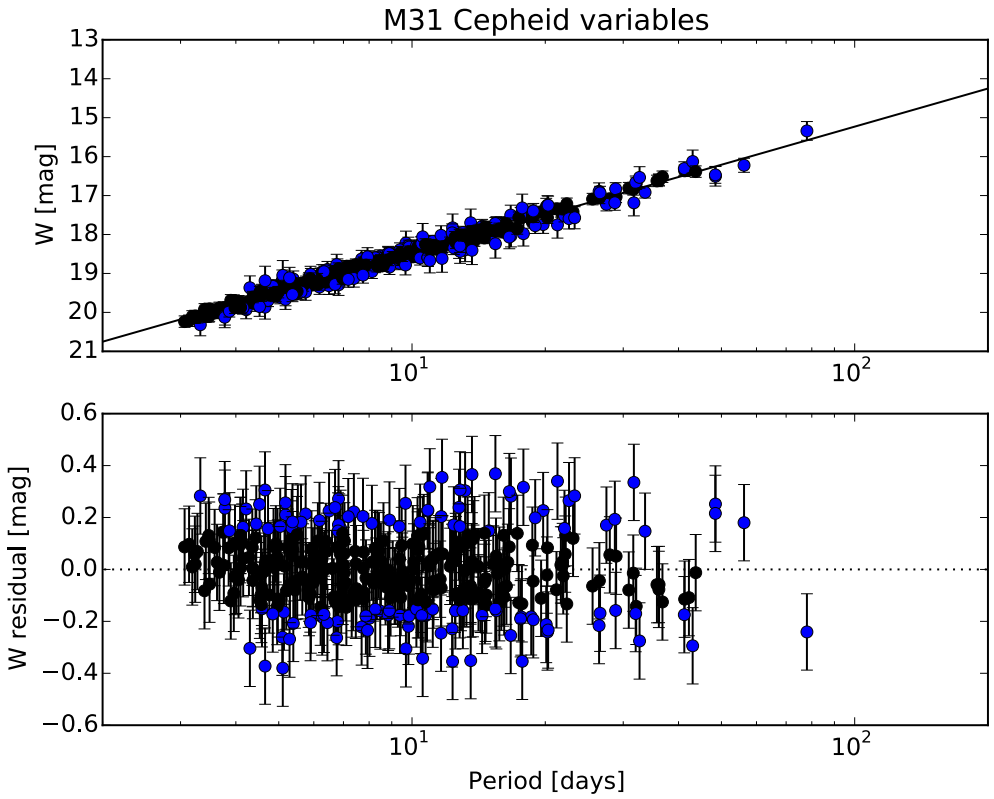

Fig. *3.14: Period-luminosity relation (upper panel) and magnitude residuals for the* M31 *Cepheid variables in the R16 data set. The solid line shows the best fit of fit* (43)*. In the upper panel we rescale error bars with HPs, in the lower panel we do not. Data are colour-coded as explained in Figure 3.2.*

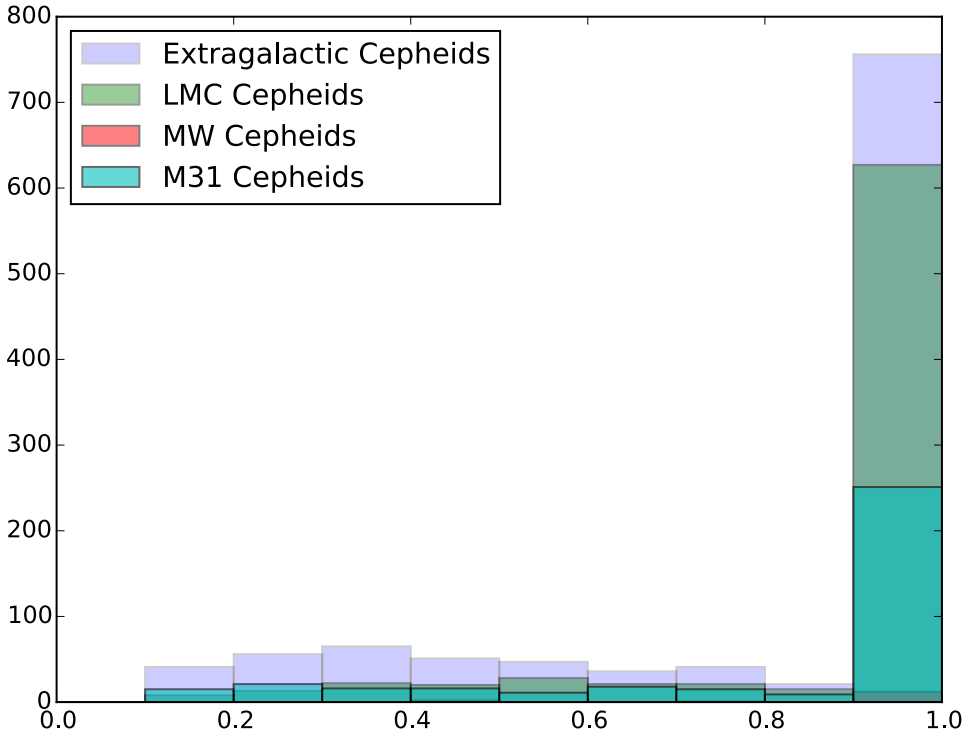

Fig. *3.15: Effective hyper-parameters for the R16 Cepheid sample used in fit* (43)*. Out of the* 1114 *Cepheid variables in the* 19 SNe Ia *host galaxies and in the* NGC4258 *megamaser system,* 733 *have* $\alpha_{\rm eff} = 1$ *and the remaining* 381 *have* $10^{-1} \leq \alpha_{\rm eff} < 1$ *(none have* $\alpha_{\rm eff} < 10^{-1}$*). Out of the* 775 LMC *Cepheid variables,* 601 *have* $\alpha_{\rm eff} = 1$ *and the remaining* 174 *have* $10^{-1} \leq \alpha_{\rm eff} < 1$ *(while none have* $\alpha_{\rm eff} < 10^{-1}$*). Out of the* 15 MW *Cepheid stars,* 12 *have* $\alpha_{\rm eff} = 1$ *and the remaining* 3 *have* $10^{-1} \leq \alpha_{\rm eff} < 1$ *(compare with Figure 3.4). Out of the* 372 M31 *Cepheid stars,* 249 *have* $\alpha_{\rm eff} = 1$ *and the remaining* 123 *have* $10^{-1} \leq \alpha_{\rm eff} < 1$ *(none have* $\alpha_{\rm eff} < 10^{-1}$*). Overall,* 20% *of the* MW *Cepheids are down-weighted; this fraction reaches* 22% *and* 33% *for* LMC *Cepheids and* M31 *Cepheids, respectively; as for the Cepheid variables in the* 19 SNe Ia *hosts and the* NGC4258 *system the fraction is* 34%*.*

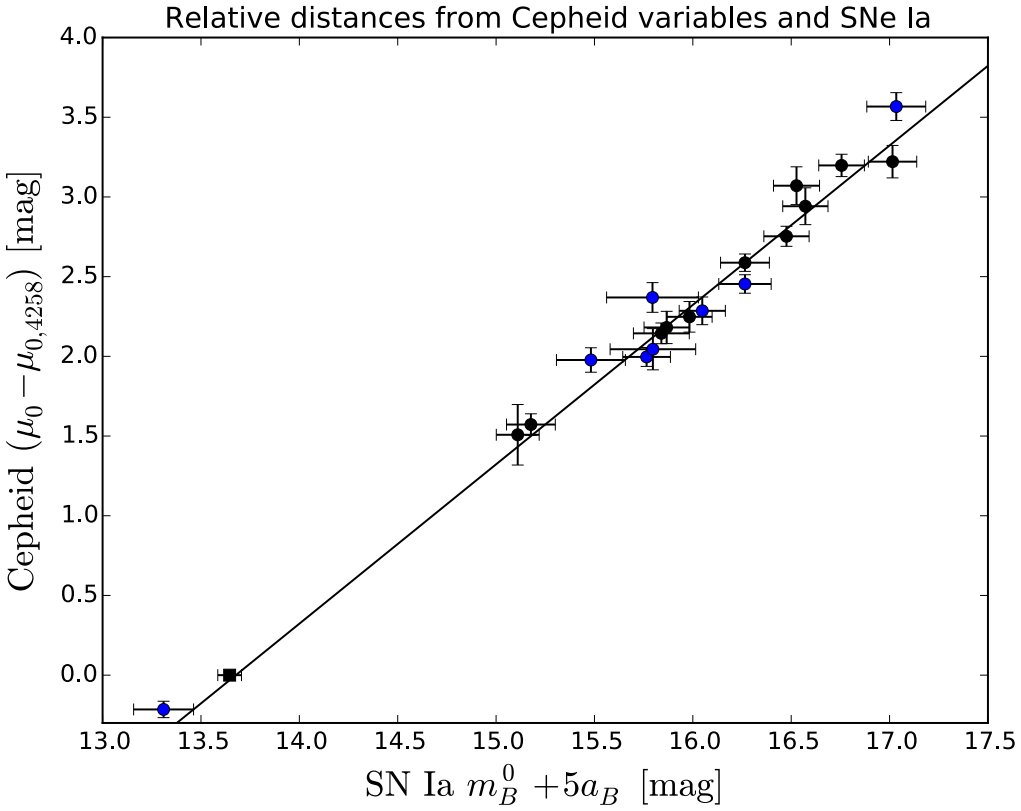

Fig. *3.16: Relative distances from Cepheids and* SNe Ia*. We plot the peak apparent visual magnitudes of each* SNe Ia *(from Table 5 in [32]) with error bars rescaled by HPs (colour code is the same as in Figure 3.2) against the relative distances between hosts determined from fit* (43) *in Table 3.4. The solid line shows the corresponding best fit. The black square on the left corresponds to the expected reddening-free, peak magnitude of an* SNe Ia *appearing in the megamaser system* NGC4258 *which is derived from the fit* (43)*.*

Distance parameters				
Host	SNe Ia	$\mu_{0,i} - \mu_{0,4258}$	$\mu_{0,i}$ best	α_{eff}
m101	2011fe	−0.215 (0.049)	29.09 (0.05)	1
n1015	2009ig	3.216 (0.100)	32.53 (0.10)	1
n1309	2002fk	3.190 (0.070)	32.50 (0.07)	1
n1365	2012fr	1.968 (0.076)	31.28 (0.08)	1
n1448	2001el	1.981 (0.059)	31.29 (0.06)	0.52
n2442	2015F	2.171 (0.065)	31.48 (0.07)	1
n3021	1995al	3.058 (0.117)	32.37 (0.12)	0.86
n3370	1994ae	2.746 (0.063)	32.06 (0.07)	1
n3447	2012ht	2.572 (0.054)	31.88 (0.06)	1
n3972	2011by	2.285 (0.087)	31.59 (0.09)	0.60
n3982	1998aq	2.356 (0.093)	31.67 (0.09)	0.23
n4038	2007sr	2.048 (0.125)	31.36 (0.13)	0.39
n4424	2012cg	1.497 (0.182)	30.81 (0.18)	1
n4536	1981B	1.564 (0.067)	30.87 (0.07)	1
n4639	1990N	2.235 (0.097)	31.55 (0.10)	0.75
n5584	2007af	2.446 (0.058)	31.76 (0.06)	0.37
n5917	2005cf	2.939 (0.115)	32.25 (0.11)	1
n7250	2013dy	2.185 (0.102)	31.50 (0.10)	1
u9391	2003du	3.555 (0.087)	32.87 (0.09)	0.48

Tab. *3.6: Distance parameters for the* SNe Ia *hosts corresponding to our primary fit [fit* (43)*] for the R16 data set. Numbers in brackets indicate the standard deviation. The last column contains the effective HP for each* SNe Ia *host.*

uncertainty because of its slightly wider wings), the normalised weight of anchors depends on the variants of the analysis (R, period cut-off, metallicity prior) ranging from 0.62 to 1. Hence, there is no strong reason to exclude the use of HPs in this kind of data.

Figure 3.17 shows the best estimates of H_0 by G. Efstathiou [117], Riess et al. [78], Riess et al. [32], and those in this work, fits (29) and (43), along with the indirect determinations of H_0 by the WMAP team [132] and by the Planck collaboration [21]. Our best estimate using the R11 data set, fit (29), is the most uncertain (a 5.2% measurement) of all presented measurements, but it agrees with all previous direct determinations of H_0 and differs by 1.8σ from the Planck value. Note that because G. Efstathiou considered only NGC4258 as an anchor and set a period cut-off of 60 days, his determination is more uncertain than that of Riess et al. [78] which used three anchors and no period cut-off. As illustrated in the figure, our best estimate using the R16 data set, fit (43), also agrees with the previous determinations of H_0, while its uncertainty is smaller (a 2.9% measurement) than the one of fit (29). Concerning the indirect determinations of H_0, we see that our best estimate, fit (43), agrees within 1σ with WMAP 2009, but it is in 2.6σ disagreement with the Planck value. This tension could be an indicator of unresolved systematics in CMB data [32].

3.4 Discussion and Conclusions

In the previous Section we presented a statistical method which allows a comprehensive treatment of available data in order to determine the universe's current expansion H_0. The use of Bayesian hyper-parameters avoids the arbitrary discard of data which is implicit in outlier rejection algorithms. Such algorithms have been used in [116], [78], [117] and in some cases a dependence of the results with the applied statistical method utilised has been found. The determination of the Hubble constant with Bayesian hyper-parameters is robust against different assumptions in the analysis (e.g., period cut in the Cepheid variables data, prior on the metallicity parameter Z_W of the period-luminosity relation, reddening law) as listed in Table 3.4. In addition, since the method uses all available data sets, it allows to check how consistent with each other they are and how much weight they are assigned in the fit. Low values of HPs might be due to unrecognised (or underestimated) systematics in the data sets and/or might be a calling for better modelling.

We have shown that, contrary to the usual χ^2 approach, when Cepheid variables are

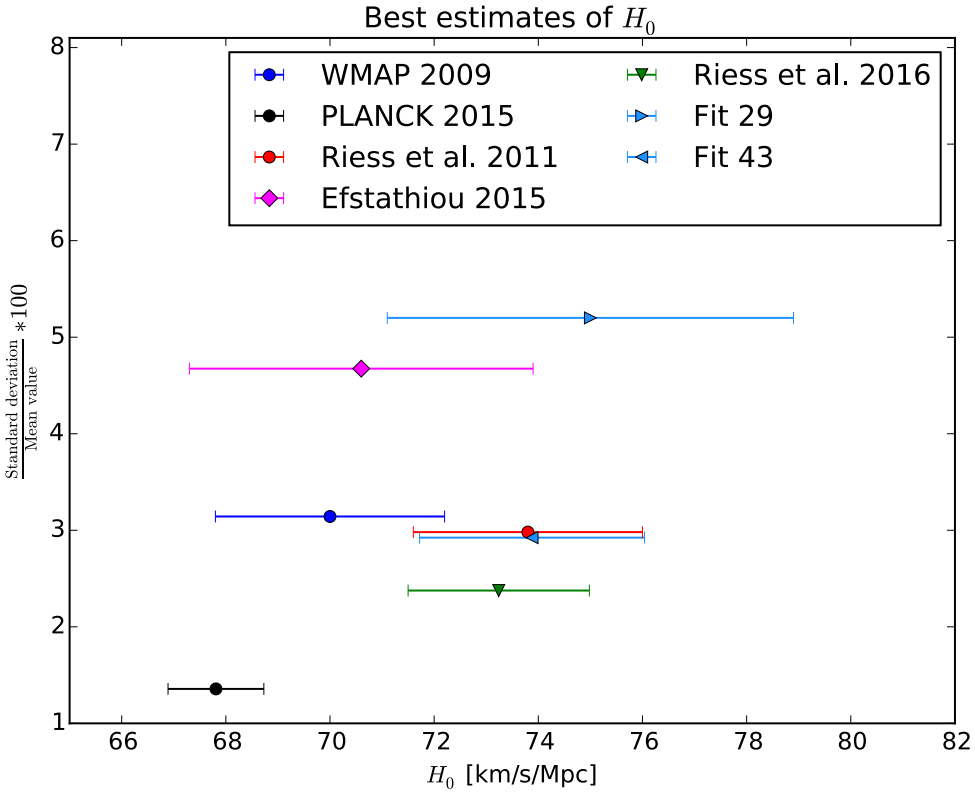

Fig. *3.17: Best estimates of the Hubble constant. Blue and black show the indirect determinations by the WMAP team [132] and by the Planck collaboration [21], respectively. Direct measurements using* NGC4258 *distance modulus,* LMC *distance modulus and* MW *Cepheid variables as anchor distances are shown in red and green; red corresponds to measurement by Riess et al. [78], whereas green shows measurement by Riess et al. [32]. Magenta shows Efstathiou's measurement [117] which uses only* NGC4258 *as anchor distance and a* 60 *days period cut-off. In dodger blue we show best estimates for both R11 and R16 data sets, fits* (29) *and* (43) *in Table 3.4, respectively.*

fitted using HPs, the down-weighted data (outlier candidates in an outlier rejection algorithm) do not significantly bias the slope b_W in the period-luminosity relation (see Figure 3.2 and Table 3.1). Note that due to degeneracies in the parameters (e.g., H_0, M_W, b_W, $Z_W, \dots$), this could also lead to a bias in the determination of the Hubble constant H_0 in the usual χ^2 analysis. Moreover, a decrement of the data set might lead to unnecessary increase of the error bars in the fitting parameters (compare, for instance, Efstathiou [117] and Riess et al. [78] H_0 values in Figure 3.17).

From Subsections 3.3.1–3.3.3 it becomes clear that the three sets of Cepheid variables in the galaxies LMC, MW, and NGC 4258 are consistent with each other (b_W and M_W agree within error bars), thus providing no argument to exclude any of them from the main analysis. In Subsection 3.3.4 we have studied the period-luminosity relation – allowing for a metallicity dependence – of each one of the galaxies in the R11 data set containing Cepheid variables. Table 3.2 shows that at least five galaxies have a slope b_W which differs from that of LMC Cepheid variables by about 2σ. A statistical method combining these data sets without taking those inconsistencies into account could lead to biased results (compare, for instance, b_W for our fits in Table 3.4 with the corresponding fits in Appendix A of [117] which are driven upwards). Our method is able to deal with those data sets without biasing our constraints in the period-luminosity parameters.

One of the advantages of using HPs to determine the Hubble constant is that one can assess the compatibility of different data sets. Our best estimates, fits (29) and (43), include with HPs available Cepheid variables (i.e., no period cut), available independent measurements of distance modulus to NGC4258, LMC, and M31 [only in fit (43)], and available SNe Ia apparent magnitudes, but we have also performed several variants which are shown in Table 3.4. We have estimated the degree of agreement for different kinds of data in our fits through the normalised weights (3.47) and found that fits (29) and (43) provide the best solution for R11 and R16 data sets, respectively. Although no outliers were released in the R16 data set, the HP analysis down-weights some of the Cepheid stars which passed the outlier rejection algorithm in [32]. Our analysis also suggests possible underestimated uncertainties in the SNe Ia magnitudes of both R11 and R16 data sets.

Since our analysis shows down-weighted datums in available data sets, we think an analysis with HPs is appropriate. The analysis is safe because it does not bias the results in the presence of datums with unreliable error bars. The use of HPs is conservative because it does underestimate the error bars on the constraints. Moreover, HPs are useful because they suggest the presence of possible underestimated system-

atics in the data. We conclude that as long as the sum of normalised weights (3.47) for the three kinds of data $\sum_j ||\alpha^j|| \neq 3$, HPs offer a reliable approach to measure the universe's expansion rate. In a fully compatible case for which $\sum_j ||\alpha^j|| = 3$ the usual χ^2 approach could be adopted and find constraints with smaller error bars than those in a HP approach.

Chapter 4

Testing isotropy and Gaussianity in the *Planck* CMB estimates (preliminary results)

4.1 Introduction

The cosmological principle – the assumption that the universe at sufficiently large scales is homogeneous and isotropic – is one of the cornerstones of the standard model of cosmology (see, e.g., [9, 10, 133]). Any significant indication of its violation would mean a serious caveat in our cosmological paradigm. Therefore, to examine the validity of these assumptions is crucial.

Recently, the *Planck* collaboration has measured the anisotropies in the CMB with a much better precision than the *Wilkinson Microwave Anisotropy Probe* (hereafter, *WMAP*) (see, e.g., [134]). According to the inflationary paradigm, at very early times the universe was filled with a hypothetical scalar field, the inflaton, whose fluctuations produced curvature perturbations distributed as a homogeneous and isotropic Gaussian random field. Cosmological perturbation theory establishes a relation between those primordial fluctuations and the CMB anisotropies, hence offering a unique probe to test models of the early universe. This relation implies that, in the framework of the cosmological principle, the CMB anisotropies are statistically isotropic and Gaussian. Thence, testing the statistical properties of the CMB anisotropies allows us to examine basic assumptions of the standard model of cos-

mology. In this chapter we will apply a statistical method different to those used by the *Planck* team in [135] to look for possible deviations of Gaussianity and isotropy in the *Planck* data.

The *WMAP* team [134] and other groups found some unexpected features – anomalous properties in the CMB anisotropies which are statistically inconsistent with a best-fit ΛCDM model – especially on large angular scales ($\ell < 600$). The list of anomalies includes lack of power on large angular scales [136], alignment of low-order multipoles [137–140], north-south asymmetry in both power spectra [141, 142] and several measures of non-Gaussianity [143–146], the cold spot [147, 148], and parity asymmetry in the power spectrum [149]. Not long ago, the *Planck* team has confirmed the observation of those large scale anomalies. Bearing in mind that both *Planck* and *WMAP* are cosmic variance limited, the presence of those unexpected features in the *WMAP* and *Planck* data could be, in principle, due to unaccounted systematic errors, non-subtracted foreground contamination, or more interestingly, it could have a cosmological origin. On the one hand, the fact that two independent experiments have observed the same features reduces drastically the possibility that systematics errors be the source of these anomalies [150]. On the other hand, unresolved foreground and the more appealing cosmological origin need to be studied further.

In [135] the *Plank* team tested the Gaussianity and isotropy of the CMB anisotropies and determined the statistical significance of their findings with a set of Gaussian, isotropic simulations of the CMB sky, namely, the "Full Focal Plane" (FFP6) simulations. They used several statistical methods including the study of one-dimensional moments, N-point correlation functions, Minkowski functionals, wavelet, bispectrum and phase correlations. Several of those statistical methods (e.g., N-point correlation functions, the Minkowski functionals, and the bispectrum) show consistency with Gaussianity and isotropy regardless of the mask, the component separation and the resolution of the CMB maps (i.e., N_{side}). Nevertheless, there is inconsistency with the FFP6 simulations when other methods are utilised. In their one-dimensional moments analysis they found that the variance is anomalously low at all considered resolutions ($N_{side} = 2048$, 512, 64, 32, 16) and that the skewness (kurtosis) is anomalously low (high) at low resolutions ($N_{side} = 64$, 32, 16). When using the wavelet statistics they also found inconsistencies. In particular, they report skewness (kurtosis) at small (intermediate) scales significantly lower (greater) than in the simulations. Finally, the most important discrepancy between data and simulations appears when analysing the data with the method of surrogates. The *Planck* team found presence of pronounced anisotropy and also correlations between the low-ℓ

Fourier phases in the analysed CMB maps, findings which turn out to be robust regardless of reference frame and component separation method. Similar results were obtained previously in *WMAP* data [146].

It is of great importance for the standard model of cosmology to clarify these discrepancies between the isotropic, Gaussian simulations and the *Planck* data. In this chapter we use the VSK method to test isotropy and Gaussianity with a set of Gaussian, isotropic simulations of the CMB sky. The VSK method consists of a set of statistical estimators which measure variance, skewness, and kurtosis in patches of the sky. The VSK method is similar to the wavelet statistics employed by the *Planck* collaboration but, since our analysis works in real space, it localizes possible non-subtracted foregrounds and may provide the angular scale of possible deviations of Gaussianity and isotropy in the CMB anisotropies. Recently, a similar approach was used in [151] and in [152] to study the north-south asymmetry phenomenon and non-Gaussianity in CMB anisotropies, respectively. However, the authors used overlapping patches of the sky when defining their estimators, possibly introducing spurious correlations in their estimations. Moreover, they did not use CMB maps in the full *Planck* resolution ($N_{side} = 2048$); even though this reduces the noise in the data (dominant at small scales), it also increases the error in the estimations. Using maps with lower resolution could make the error bars larger.

In the present chapter, we start out giving a brief description of the data (Section 4.2) and then present the VSK method for non-overlapping patches of the sky (Section 4.3). The VSK method is subsequently applied to both *Planck* data and Gaussian, isotropic simulations of the CMB sky and our results are discussed in Section 4.4. We conclude in Section 4.5.

4.2 Data

Here we analyse of part of the 2013 *Planck* data release corresponding to the nominal period of the *Planck* mission. We utilise some of the available masks, the two available inpainted CMB maps, and the nearly full-sky foreground cleaned CMB maps resulting from four component separation algorithms applied by the *Planck* team [153], viz., `Commander-Ruler, NILC, SEVEM` and `SMICA`. The maps and masks were provided in HEALPix[1] format, with a pixel size defined by the N_{side} parameter.

[1] http://healpix.sourceforge.net

Throughout the paper we use the standardized common mask U73 (sky coverage $f_{sky} = 73$ per cent). However, when studying the mask dependence of our analysis we use the confidence mask VALMASK ($f_{sky} = 89$ per cent) and the mask of the inpainted regions INP_MASK ($f_{sky} = 97$ per cent) of the `SMICA` CMB estimate. Where appropriate, we have changed the resolution of the mask and maps, originally having $N_{side} = 2048$. In particular, we have degraded the data to have $N_{side} = 1024$, 512, and 256. When degrading the mask we have followed a conservative approach: after degrading the mask to the final resolution using the UD_GRADE HEALPix routine, any pixel having a value lower than 0.9 has been set to zero.

Finally, in order to assess the significance of any anisotropic or non-Gaussian signal in the data, we resort to a set of 2000 simulated Gaussian, isotropic CMB maps. The Monte Carlo simulations were generated using the SYNFAST HEALPix routine based on the *Planck* best-fit power spectrum and having an effective Gaussian beam `FWHM` = 5 arcmin.

4.3 VSK Method

The method, which in the scope of this study will be referred to as VSK method, was first introduced and applied to *WMAP* data in [154] (see also [155, 156]). However, as originally proposed, the method uses overlapping patches in the sky that, as mentioned earlier, might introduce spurious correlations in the data. The VSK method was modified to employ non-overlapping patches of the sky and applied to *WMAP* data in [157] and simulations in [158]. Given a full-sky CMB map in HEALPix format with parameter N_{side}, the construction of the estimators in the VSK method proceeds as follows.

1. We remove both monopole and dipole with the REMOVE_DIPOLE HEALPix routine
2. We superimpose on the original CMB map a HEALPix grid with much lower resolution N'_{side} than that of the CMB map (e.g., $N'_{side} = 2, 4, 8, \dots$). Thus, we have a set of $12 \times N'^2_{side}$ non-overlapping patches in the sky, each patch having equal number N_p of pixels belonging to the initial CMB map[2].

[2]For a full-sky CMB map with parameter N_{side} the number of pixels is given by $12 \times N^2_{side}$. Then, the number of pixels per patch is given by $(N_{side}/N'_{side})^2$.

3. For each patch we compute sample variance,

$$V_j = \frac{1}{N_p - 1} \sum_{i=1}^{N_p} (T_i - \bar{T})^2 = \frac{N_p}{N_p - 1} \sigma_j^2, \tag{4.1}$$

sample skewness,

$$S_j = \frac{1}{N_p \sigma_j^3} \sum_{i=1}^{N_p} (T_i - \bar{T})^3, \tag{4.2}$$

and sample kurtosis,

$$K_j = \frac{1}{N_p \sigma_j^4} \sum_{i=1}^{N_p} (T_i - \bar{T})^4 - 3, \tag{4.3}$$

where j numbers the non-overlapping patches, T_i is the temperature at the i^{th} pixel in the j^{th} patch, $\bar{T}$ is the CMB mean temperature in the j^{th} patch, and σ_j denotes the standard deviation of the CMB data in the j^{th} patch. We compute sample variance, sample skewness, and sample kurtosis including only unmasked pixels; any patch for which more than 20 per cent of the area is masked is set to zero.

4. The result of computing V_j, S_j, and K_j for all the patches is three different maps, namely, one map of sample variance, one map of sample skewness and one map of sample kurtosis.

5. We repeat the four items above for the set of 2000 Gaussian, isotropic simulations CMB maps and compute zero mean sample variance maps, zero mean sample skewness maps, and zero mean sample kurtosis maps. Henceforward, we will refer to a given zero mean map as V-map, S-map and K-map, respectively.

6. Since the V-map, S-map, and the K-map are signals on the sphere, they can be written in terms of a spectral representation. For instance, for the V-map we have

$$V(\mathbf{x}) = \sum_{\ell=0}^{\infty} \sum_{m=-\ell}^{\ell} v_{\ell m} Y_{\ell m}(\mathbf{x}) \tag{4.4}$$

where $\mathbf{x}$ is a unit direction vector, $Y_{\ell m}$ the spherical harmonics and

$$v_{\ell m} = \int d\mathbf{x} V(\mathbf{x}) Y^*_{\ell m}(\mathbf{x}), \tag{4.5}$$

$m = 0, \pm 1, \ldots, \pm\ell$, $\ell = 0, 1, 2, \ldots$. Similar expressions are satisfied by both S-map and K-map.

7. Finally, we perform the harmonic analysis of the V-map, S-map, and K-map with the help of the ANAFAST HEALPIX routine with maximum spherical harmonic order given by $\ell_{max} = 3 \times N'_{side} - 1$. Taking as an example the $V(\mathbf{x})$ signal again, we have

$$V_\ell = \frac{1}{2\ell + 1} \sum_m |v_{\ell m}|^2, \tag{4.6}$$

where V_ℓ is the angular power spectrum of the V-map. Similar expressions S_ℓ and K_ℓ apply for S-map and K-map, respectively.

Throughout this chapter we quantify the degree of agreement between the Gaussian, isotropic simulations and the observations by a simple χ^2 test which has been performed separately for the V, S, and K estimators. For instance, for the V estimator we define χ^2_V as

$$\chi^2_V = \sum_{\ell\ell'} \left(V_\ell - \langle V_\ell \rangle_G\right) C^{-1}_{\ell\ell'} \left(V_{\ell'} - \langle V_{\ell'} \rangle_G\right), \tag{4.7}$$

with analogous expressions for S and K estimators. In equation (4.7) V_ℓ is the angular power spectrum of a V-map computed out of a given full-sky CMB map, $\langle V_\ell \rangle_G$ the corresponding average from the first 1000 Gaussian, isotropic simulations, and

$$C_{\ell\ell'} = \langle \left(V_\ell - \langle V_\ell \rangle_G\right) \left(V_{\ell'} - \langle V_{\ell'} \rangle_G\right) \rangle_G \tag{4.8}$$

the covariance matrix from the remaining 1000 Gaussian, isotropic simulations.

4.4 Results

We now apply the VSK method to the *Planck* data. We start by examining how the method works when using full-sky ($f_{sky} = 100$ per cent) CMB maps. In particular, we use the two inpainted CMB estimates released by the *Planck* collaboration, namely, the $N_{side} = 2048$ inpainted `SMICA` and `NILC`.

Figures 4.1–4.3 show V-map, S-map, and K-map for the inpainted `SMICA`. In Figures 4.4–4.6 we plot angular power spectra for the V-map, S-map, and the K-map computed for both inpainted `SMICA` and `NILC` CMB estimates, as well as for 1000 Gaussian, isotropic simulations using $N'_{side} = 2$. The mean angular power spectra for the simulations do not exhibit any strong scale dependence. The angular power

Tab. *4.1: Lower-tail probability for the V, S, K estimators, for the $N_{side} = 2048$ inpainted* `SMICA` *and* `NILC`*.*

	Probability		
CMB estimate	V	S	K
		$N'_{side} = 2$	
`SMICA`	0.939	0.388	0.096
`NILC`	0.939	0.022	1.0
		$N'_{side} = 4$	
`SMICA`	0.969	0.727	0.521
`NILC`	0.943	0.761	1.0
		$N'_{side} = 8$	
`SMICA`	1	0.551	0.581
`NILC`	0.964	0.474	1

spectrum of the variance maps, V_ℓ, for the two considered CMB estimates show no departure from the null hypothesis. The VSK method does not bring about any dipolar structure in the inpainted CMB estimates; this so-called north-south asymmetry, was found in *WMAP* and *Planck* data [135, 141, 142, 159]. Using different values of the parameter N'_{side}, we are verifying the robustness of this result for the inpainted CMB maps. The angular power spectra of the corresponding S-maps, S_ℓ, is consistent with the null hypothesis. The most remarkable difference between the two CMB estimates is brought out when looking at the corresponding K_ℓ. The inpainting technique applied to the `NILC` CMB estimate seems to induce kurtosis at all considered scales. We checked that this contribution vanishes when the inpainted region is masked (see Figure 4.15). In Figures 4.7–4.9 we show the χ^2 analyses for the spectra in Figures 4.4–4.6. Note that due to the discrepancy in the inpainted `NILC`, we do not show its χ^2 value for K_ℓ. In Table 4.1 we show the lower-tail probability computed out of N-pdf χ^2 for different values of the parameter N'_{side}. The V, S, and K estimators give consistent results for the two CMB estimates and we are studying whether or not the results depend on the N'_{side} parameter. The only discrepancy appears for the K-map inpainted `NILC` that is fully inconsistent with the Gaussian, isotropic simulations.

According to the previous analysis the inpainting technique applied to `NILC` might induce deviations of the null hypothesis. We now apply the VSK method to the almost full-sky $N_{side} = 2048$ CMB estimates; we examine the four component separation methods mentioned above and use the U73 mask. In Figures 4.10–4.12 we illustrate, as an example, the V-map, S-map, and the K-map for the `SMICA` estimate. In Figures 4.13–4.15 we plot the corresponding angular power spectra V_ℓ, S_ℓ, and

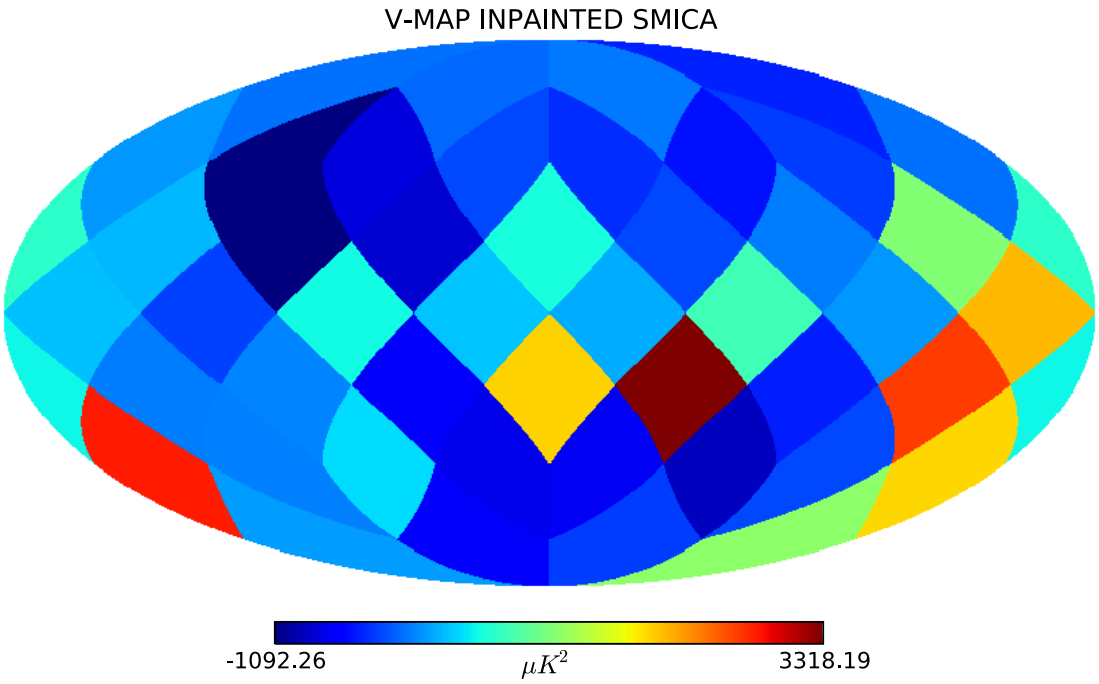

Fig. *4.1:* $N'_{side=2}$ *V-map for the* $N_{side} = 2048$ *inpainted SMICA CMB estimate.*

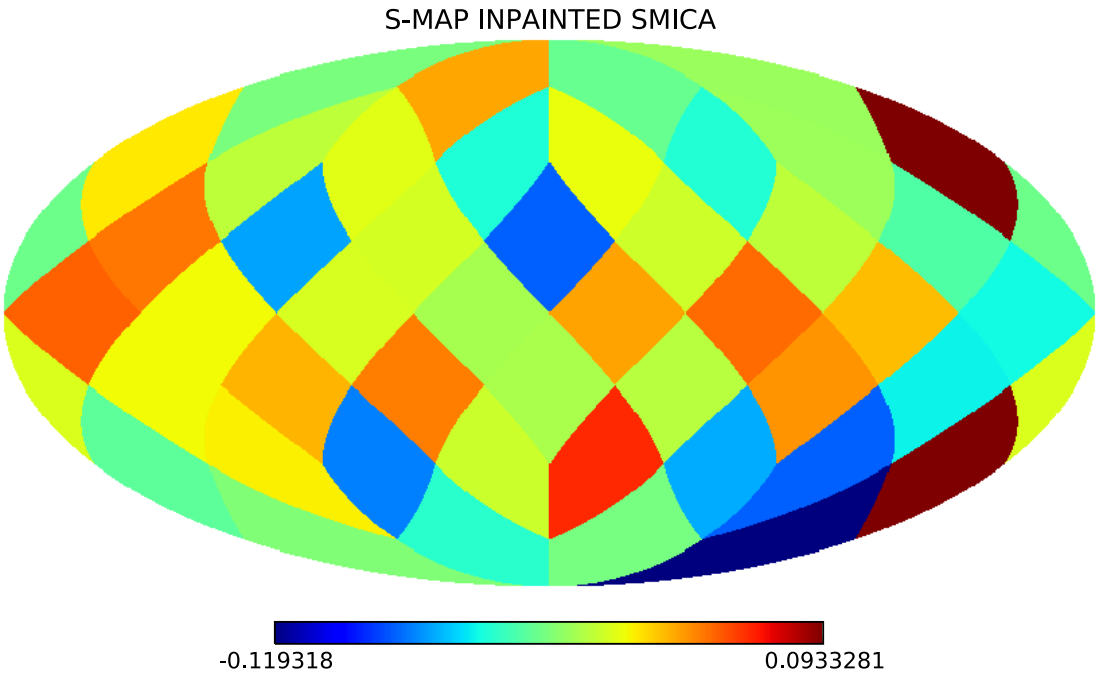

Fig. *4.2:* $N'_{side=2}$ *S-map for the* $N_{side} = 2048$ *inpainted SMICA CMB estimate.*

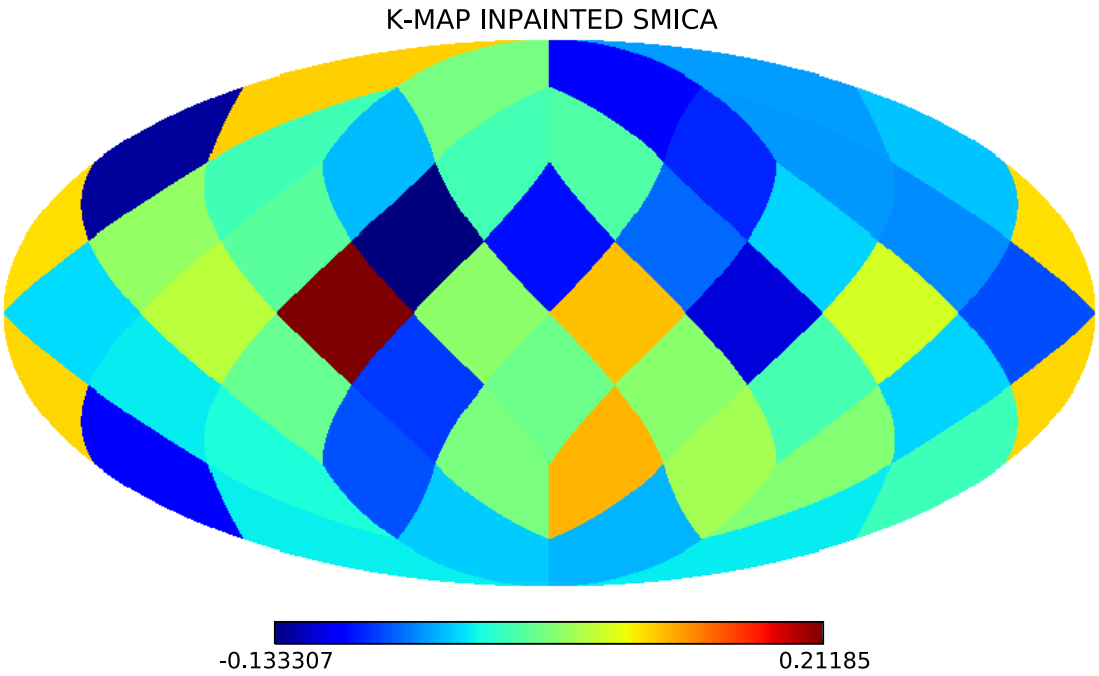

Fig. *4.3:* $N'_{side=2}$ *K-map for the* $N_{side} = 2048$ *inpainted SMICA CMB estimate.*

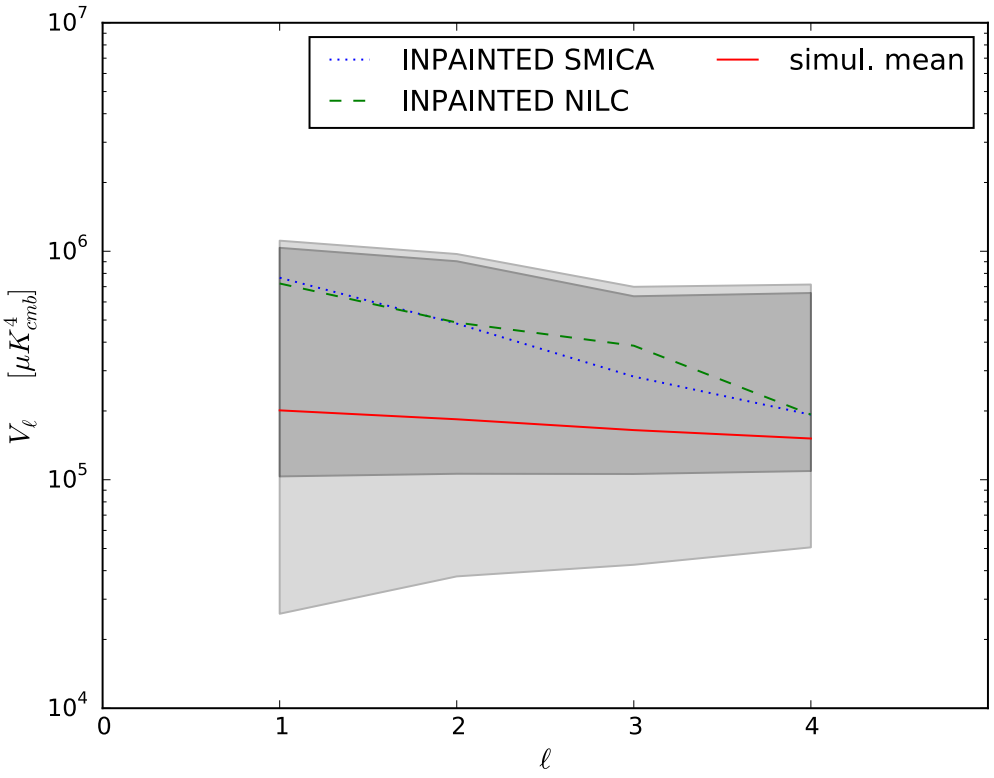

Fig. *4.4: Angular power spectra for the $N'_{side} = 2$ V-map computed out of the full-sky $N_{side} = 2048$ inpainted CMB estimates. The red solid line indicates the mean for 1000 Monte Carlo simulations and the shaded dark and light gray regions indicate the 68 per cent and 95 per cent confidence regions, respectively.*

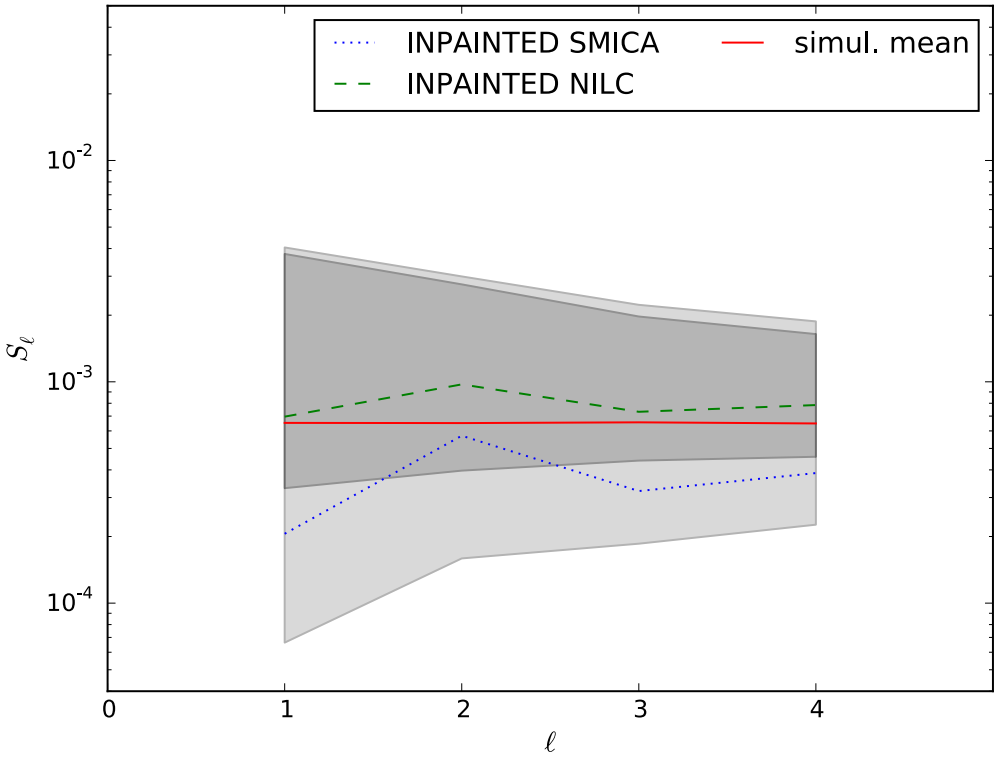

Fig. *4.5: Angular power spectra for the $N'_{side} = 2$ S-map computed out of the full-sky $N_{side} = 2048$ inpainted CMB estimates. The red solid line indicates the mean for 1000 Monte Carlo simulations and the shaded dark and light gray regions indicate the 68 per cent and 95 per cent confidence regions, respectively.*

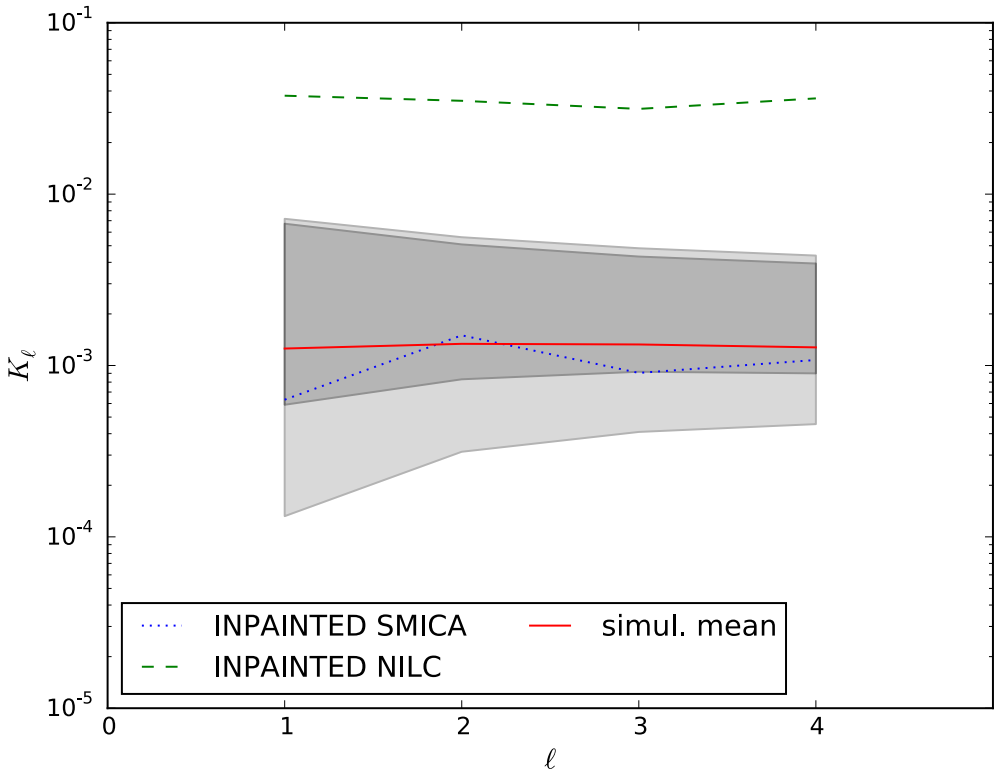

Fig. *4.6: Angular power spectra for the $N'_{side} = 2$ K-map computed out of the full-sky $N_{side} = 2048$ inpainted CMB estimates. The red solid line indicates the mean for* 1000 *Monte Carlo simulations and the shaded dark and light gray regions indicate the* 68 *per cent and* 95 *per cent confidence regions, respectively.*

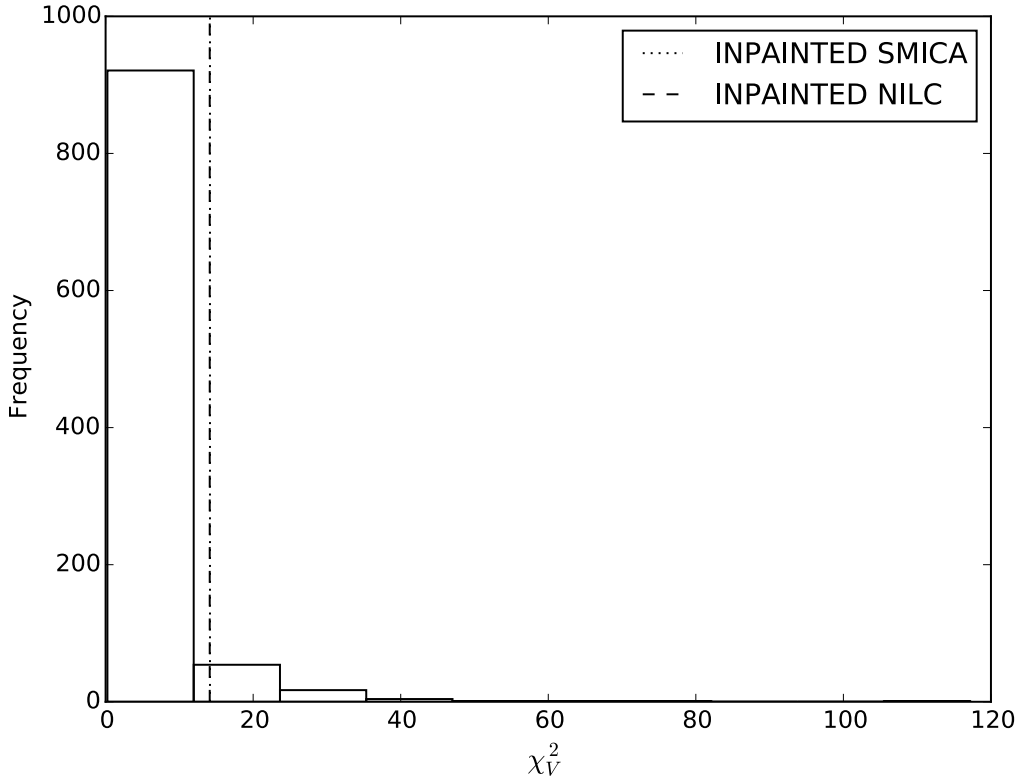

Fig. *4.7: N-pdf χ^2 for the angular power spectra shown in Figure 4.4. The vertical lines show values for the corresponding CMB estimates.*

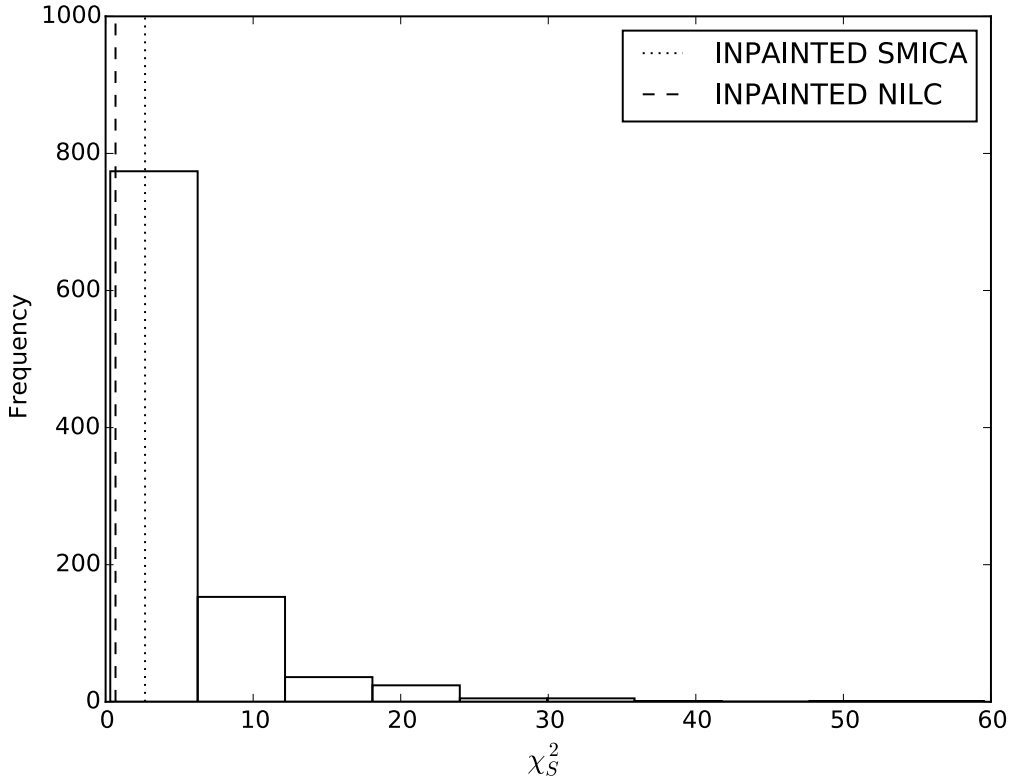

Fig. *4.8: N-pdf χ^2 for the angular power spectra shown in Figure 4.5. The vertical lines show values for the corresponding CMB estimates.*

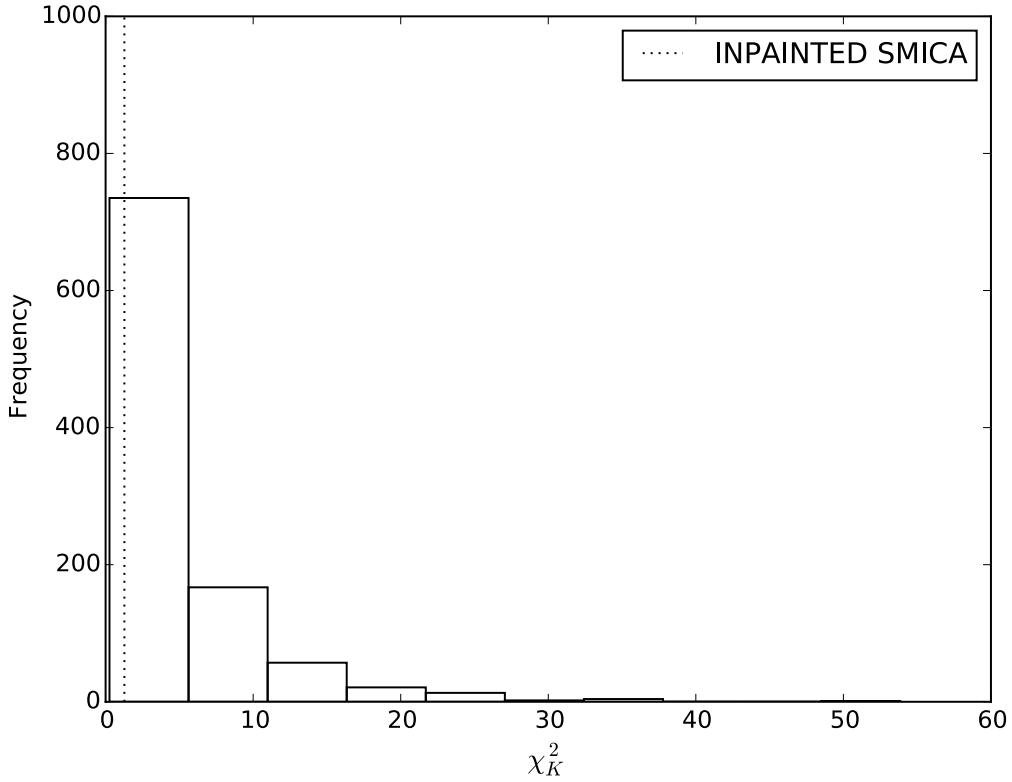

Fig. *4.9: N-pdf χ^2 for the angular power spectra shown in Figure 4.6. The vertical lines show values for the corresponding CMB estimates.*

K_ℓ computed for the four component separation CMB estimates. Since all the four CMB estimates are consistent with the null hypothesis, we conclude the inpainting technique applied to the `NILC` CMB map causes the discrepancy we noted before (see Figure 4.6).

A modification in the VSK method to include only unmasked regions in the computation of the angular power spectrum would be necessary. This would allow to know the true shape of the angular power spectra and avoid spurious features possibly induced by the masked region. Nevertheless, since in this work we want to test whether or not the *Planck* data are consistent with the null hypothesis, we will not include this modification in the present chapter. Such a modification would require to adapt the VSK method as explained in [160] and [161]. The code PolSpice can analyse functions on the cut-sky, correcting the effects of the masks. An adaptation of the VSK method using PolSpice is under development.

None of the four component separation methods exhibits a dipole in the V-maps outside the 95 per cent confidence region for $N'_{side} = 2$. Since all the four component separation methods give pretty similar results and to avoid circumlocution, in Table 4.2 we present the lower-tail probabilities only for the `SMICA` CMB estimate masked with the U73 mask. We are examining the dependence of our results on the parameters N_{side} and N'_{side}. Thus far, we do not see significant deviation of the null hypothesis for almost all the possible combinations of parameters considered.

Since discrepancies might arise due to unresolved foregrounds, we are also investigating how our results depend on the masked region. The results for both the confidence mask and the mask of inpainted regions for `SMICA` are shown in Table 4.3. In order to facilitate the comparison, some of the results for the mask U73 are repeated.

4.5 Conclusions

In this chapter we carried out a non-parametric analysis, the VSK method, to test for possible departures from the cosmological principle in the CMB anisotropies measured by the *Planck* satellite. We used the available full-sky maps (inpainted `SMICA` and `NILC`) and the four almost full-sky CMB estimates released in 2013 by the *Planck* collaboration (`SMICA, NILC, Commander-Ruler,` and `SEVEM`). We investigated possible anomalous angular variations of the variance, skewness, and kurtosis in the CMB anisotropies and determined the statistical significance of our results by using a set of Gaussian, isotropic simulations of the CMB sky seeded by the *Planck* best-fit

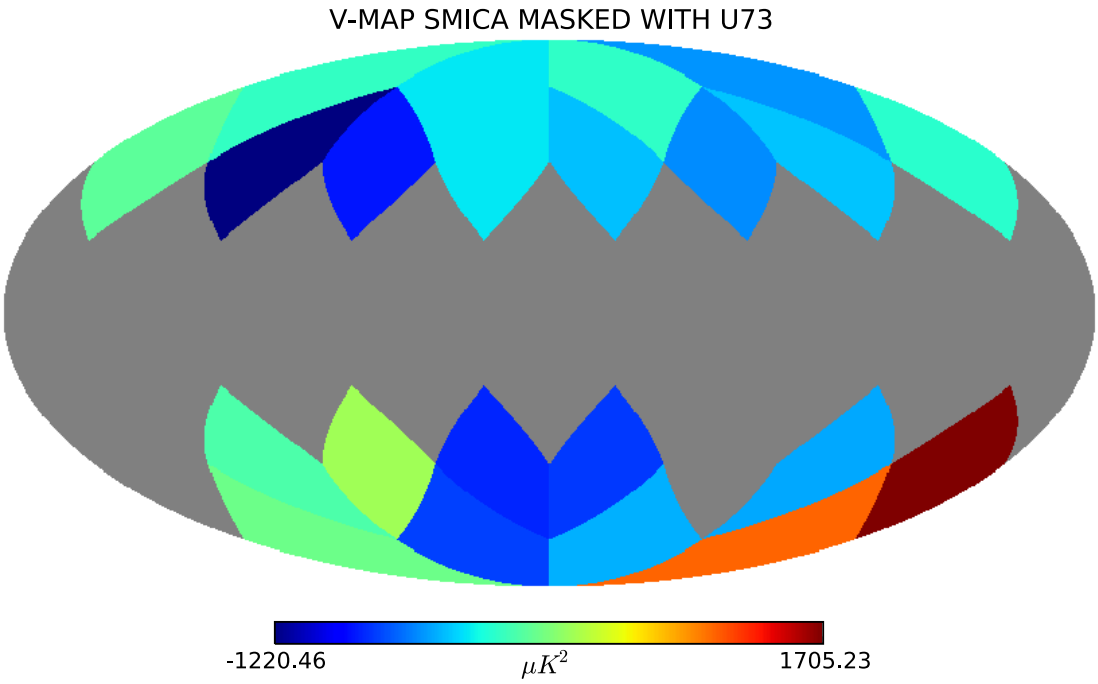

Fig. *4.10:* $N'_{side=2}$ *V-map for the* $N_{side} = 2048$ *SMICA CMB estimate masked with the U73 mask.*

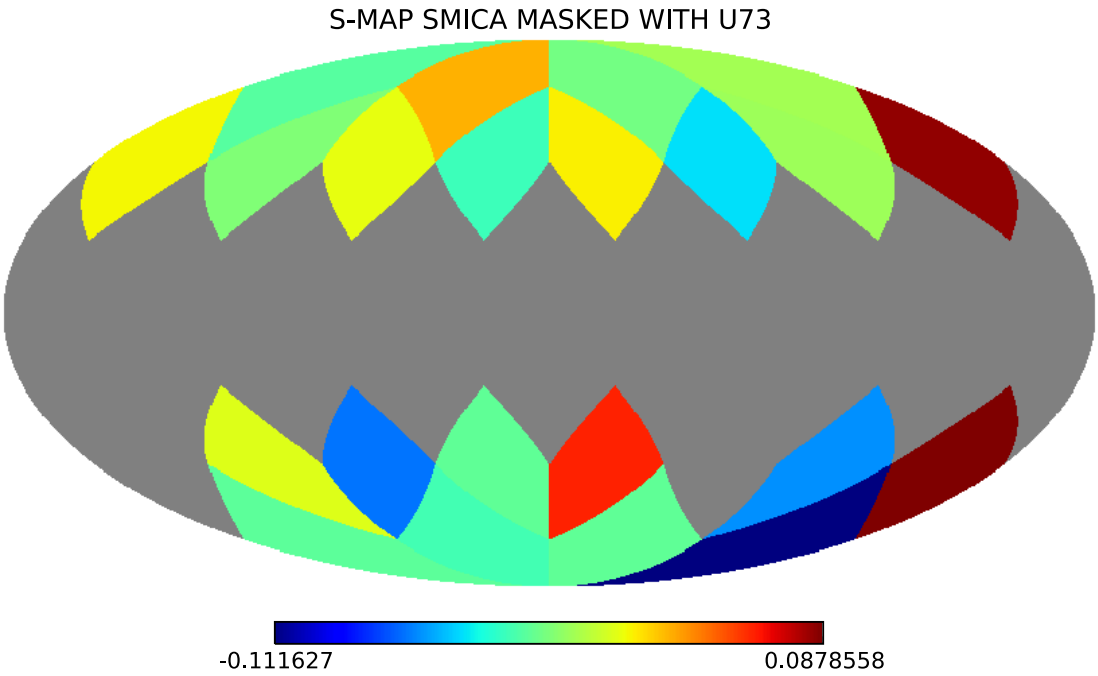

Fig. *4.11:* $N'_{side=2}$ *S-map for the* $N_{side} = 2048$ *SMICA CMB estimate masked with the U73 mask.*

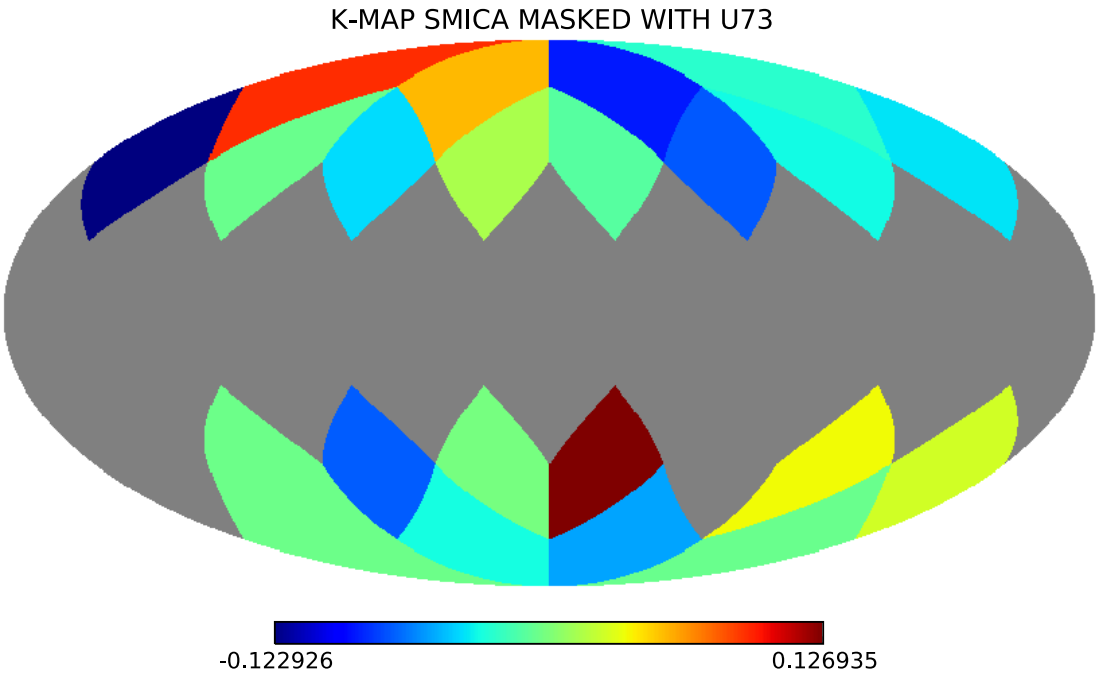

Fig. *4.12:* $N'_{side=2}$ *K-map for the* $N_{side} = 2048$ *SMICA CMB estimate masked with the U73 mask.*

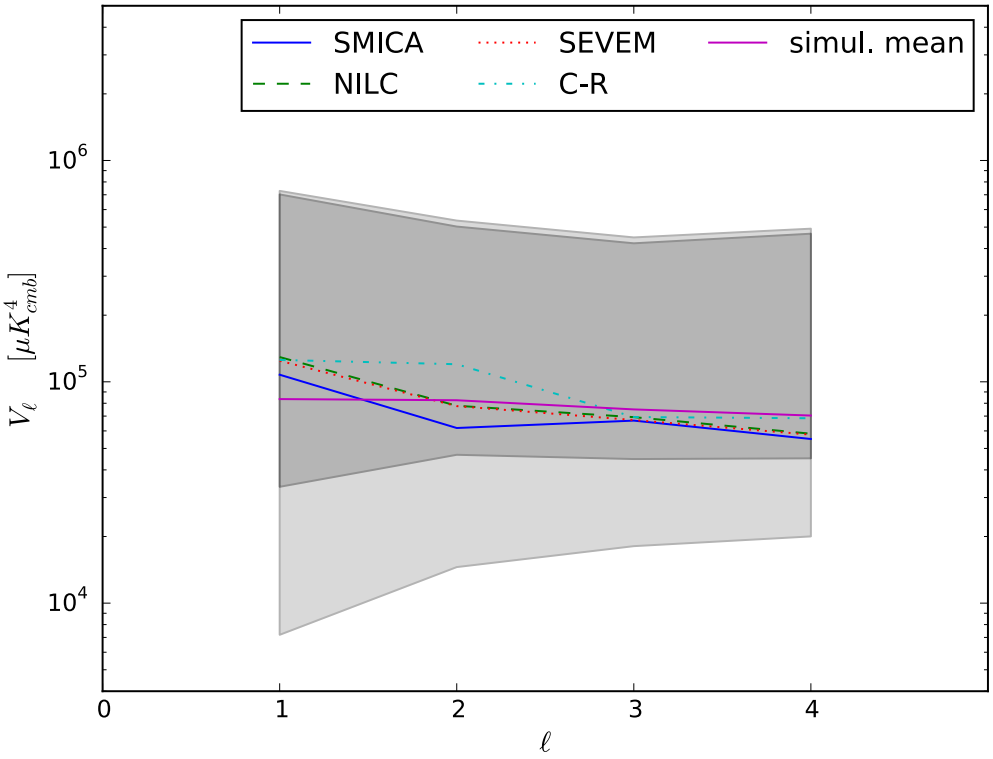

Fig. *4.13: Angular power spectra of the* $N'_{side} = 2$ *V-map for the four* $N_{side} = 2048$ *CMB estimates. The magenta line indicates the mean angular power spectrum for* 1000 *Monte Carlo simulations and the shaded dark and light gray regions indicate the* 68 *per cent and* 95 *per cent confidence regions, respectively.*

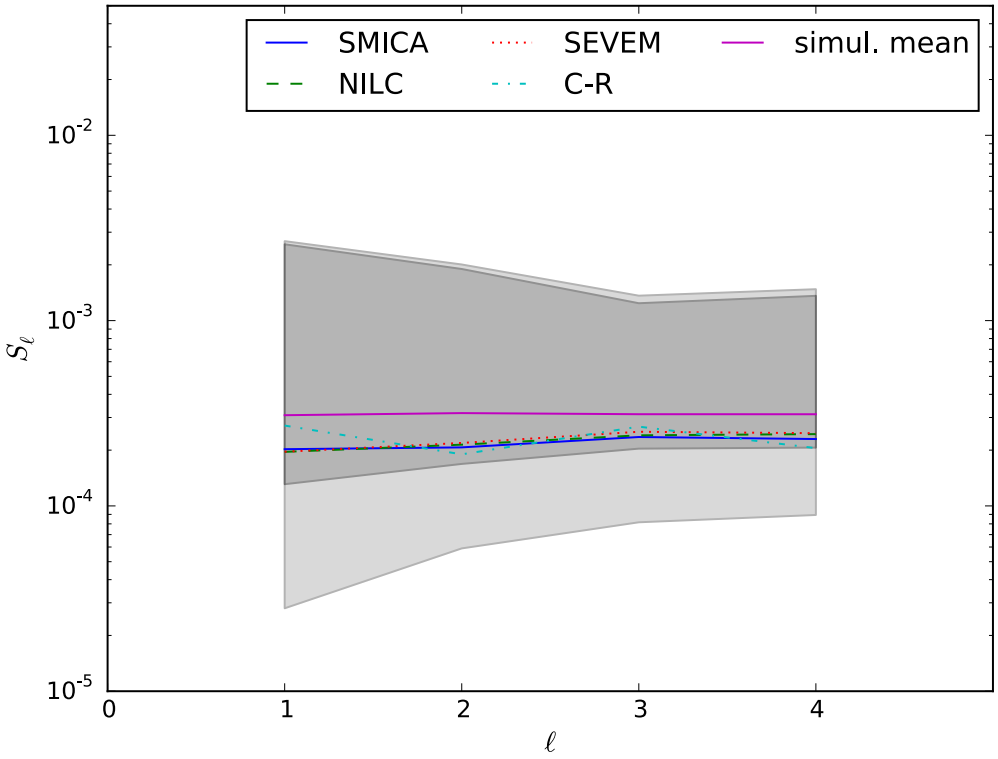

Fig. *4.14: Angular power spectra of the* $N'_{side} = 2$ *S-map for the four* $N_{side} = 2048$ *CMB estimates. The magenta line indicates the mean angular power spectrum for* 1000 *Monte Carlo simulations and the shaded dark and light gray regions indicate the* 68 *per cent and* 95 *per cent confidence regions, respectively.*

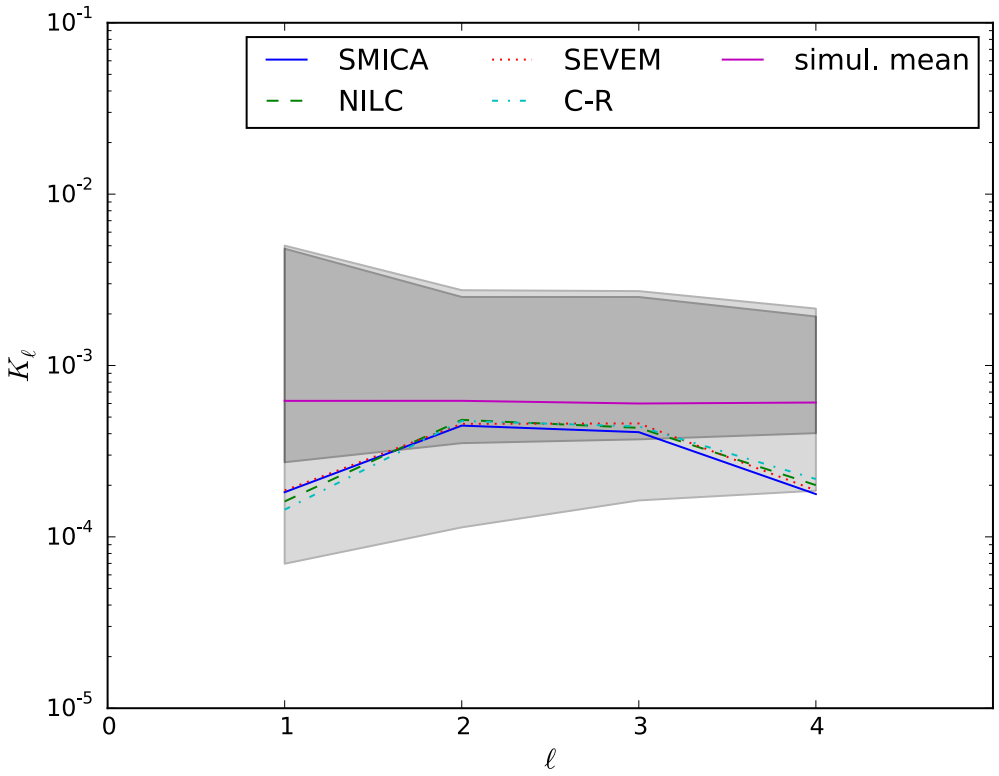

Fig. *4.15: Angular power spectra of the* $N'_{side} = 2$ *K-map for the four* $N_{side} = 2048$ *CMB estimates. The magenta line indicates the mean angular power spectrum for* 1000 *Monte Carlo simulations and the shaded dark and light gray regions indicate the* 68 *per cent and* 95 *per cent confidence regions, respectively.*

Tab. *4.2: Lower-tail probability for the V, S, K estimators using different N'_{side}, for different resolutions N_{side} of the* `SMICA` *CMB estimate using the U73 mask.*

	Probability		
N'_{side}	V	S	K
		$N_{side} = 2048$	
2	0.004	0.024	0.367
4	0.893	0.407	0.340
8	0.695	0.116	0.406
		$N_{side} = 1024$	
2	0.556	0.022	0.281
4	0.873	0.446	0.229
8	0.782	0.117	0.264
16	0.442	0.084	0.153
		$N_{side} = 512$	
2	0.711	0.027	0.229
4	0.898	0.485	0.240
8	0.794	0.103	0.140
16	0.311	0.200	0.146
		$N_{side} = 256$	
2	0.040	0.123	0.225
4	0.996	0.480	0.404
8	1.0	0.235	0.104
16	1.0	0.584	0.459

***Tab.** 4.3: Lower-tail probability for the V, S, K estimators at $N'_{side} = 2$, for the SMICA CMB estimate using different masks.*

	Probability		
N'_{side}	V	S	K
		U73 ($f_{sky} = 73\%$)	
2	0.004	0.024	0.367
4	0.893	0.407	0.340
8	0.695	0.116	0.406
		VALMASK ($f_{sky} = 89\%$)	
2	0.004	0.022	0.357
4	0.895	0.371	0.343
8	0.7	0.099	0.385
		INP_MASK ($f_{sky} = 97\%$)	
2	0.003	0.016	0.382
4	0.897	0.367	0.374
8	0.685	0.099	0.428

angular power spectrum.

The VSK method applied to inpainted *Planck* maps brings about the following features. The V estimator indicates no departure (95 per cent confidence region) of the null hypothesis at the level of the dipole and the quadrupole. Thus far, these results are robust against both component separation and the parameter N'_{side} of the VSK method. The S estimator is fully consistent with the null hypothesis in both CMB estimates. This is not the case for the K estimator, where only inpainted SMICA turns out to be consistent with the simulations. According to the K estimator, the inpainting method applied to NILC induces kurtosis on all scales allowed by a given N'_{side}. It remains to be seen whether or not this discrepancy with the null hypothesis becomes less significant when higher N'_{side} is employed.

We studied several aspects of the VSK method applied to the almost full-sky *Planck* maps. In particular, we considered the VSK method applied to the four component separation CMB estimates by using different resolutions of the data (N_{side}), masks, and N'_{side}. Thus far, all the four component separation methods are fully consistent with the hypothesis of a universe statistically isotropic and Gaussian regardless of these parameters of the VSK method. It remains to be seen, however, whether the VSK method using a larger sky fraction of the sky would bring about anomalies such as north-south asymmetry or quadrupole alignment.

When applying the VSK method to masked CMB maps one must be careful. Since the method computes the full-sky angular power spectrum of V-map, S-map, and K-map, the masked region of those maps might include spurious correlations. A modified VSK method should take into account only unmasked pixels of the V-map, S-map, and K-map and use orthogonal functions on the cut sphere in order to avoid this caveat. Since both the simulations and the data are affected in the same way by this limitation of the method, such a modification might not alter our results (consistency with the null hypothesis), but produce the true shape of the angular power spectra.

Finally, we notice that the results presented in this chapter are just preliminary and the project is ongoing. The 2015 *Planck* data is now available and includes a sophisticated set of Gaussian, isotropic simulations (the FFP8 simulations). These simulations are maps of the CMB for the different frequencies in the *Planck* satellite. Since we have shown that the four component separation methods are in agreement with each other when analysed with the VSK method, the use of the FFP8 simulations in this project would require the implementation of at least one the component separation methods. We plan to do this for the `SEVEM` component separation. Another additional point worthy of further investigation would be the dependence of the results with CMB frequency. These two additional points – use of FFP8 simulations and frequency dependence – would make possible a direct comparison with the results found by the *Planck* team.

Chapter 5

Summary and outlook

Almost two decades after the discovery of the universe's acceleration in 1998 its fundamental cause remains largely unknown and one of the most important questions in cosmology. The current concordance cosmological model, although both simple and a good fit for the universe's expansion, lacks in fundamental grounds. On the one hand, physicists have been making a huge effort to find direct evidence of dark matter, but thus far no detection has been observed. On the other hand, the incredibly small value of the observed vacuum energy has eluded an explanation within the quantum field theory framework.

Some alternative approaches to explain the universe's accelerating expansion from first principles have been proposed over past years (e.g., evolving scalar fields models, modified gravity models, higher dimensions), but degeneracies at the model level remain. Although analyses of current data sets have made it possible to shrink the allowed regions in parameter space, this effort has not been enough to rule out most of the alternatives to the concordance model of cosmology. This situation is however expected to change with the come of new data from the new generation of both ground-based and space-based experiments; future galaxy surveys like Euclid will map the distribution of matter in the universe at scales comparable to the horizon; the James Webb Space Telescope (Webb), which is the successor of the Hubble Space Telescope, will probably help to augment the sample of SNe Ia hosts; the Gaia mission will surely provide parallax measurements of new Cepheid stars in our galaxy. Precise measurements of the Hubble constant H_0, the equation of state of the dark energy w, and the matter power spectrum would allow to conclusively discriminate ΛCDM from its alternatives.

Precise measurements will require careful modelling and statistical methods as good as the data sets, otherwise the analysis could lead to biased results and underestimation of error bars. In Chapter 3, Martin Kunz, Valeria Pettorino, and I have applied a Bayesian method to determine the universe's current expansion rate H_0. Our detailed analysis of samples of Cepheid variables and SNe Ia hosts from [32, 78] show that the precision of our measurements depends on the consistency of the data sets. We found our measurements of H_0 to be in good agreement with those by Riess et al. [32, 78], but with slightly larger error bars. Our results therefore confirm the disagreement between local and indirect determinations of the Hubble constant. This tension could arise from issues with the statistical method used in the determination of H_0, be a hint of remaining CMB systematics [32], or signify new physics. Despite using a different statistical method as in Riess et al [32], both results agree very well. This leads to the conclusion that the current local measurement of H_0 is robust against method biases. When adding external data sets to the CMB data, the Planck collaboration utilised a conservative prior given by the analysis of G. Efstathiou [117] that only uses NGC4258 megamaser system as an anchor distance. Although Efstathiou's value is consistent, within error bars, with our determination of H_0 using the R16 data set, his measurement has larger error bars. The inclusion of Efstathiou's value in the Planck analysis should therefore be revised as it discards data and might hinder our understanding of both cosmological model and data sets.

An accurate and precise measurement of the Hubble constant H_0 will certainly be key in determining the neutrino absolute mass scale. CMB data and local measurements of the Hubble constant, for instance, will help to break degeneracies (e.g., H_0 and m_ν) and improve constraints on cosmological parameters from future galaxy surveys. Ruth Durrer, Martin Kunz, Francesco Montanari, and I have however shown in Ref. [31] that a careful modelling of number counts will be required. In particular, relativistic effects such as lensing convergence will need to be included in analyses of data from future galaxy surveys. Neglecting lensing convergence when constraining neutrino masses, for instance, would lead to spurious detection of their absolute mass scale, thus hindering one of the key goals of future surveys. Since biases of cosmological parameters in analyses neglecting lensing might reach several standard deviations, the usual linear approximation in Fisher matrix formalisms breaks down and might not be appropriate any longer. We have shown that a Markov Chain Monte Carlo approach is suitable for reliable forecasts of neutrino masses. The analysis in Ref. [31] used the number counts angular power spectrum $C_\ell(z, z')$ – an observable – to make forecasts for an Euclid-like satellite. It took into account all relevant relativistic effects, but included non-linear effects very conservatively and

analysed scales up to $\ell = 400$. Non-linear effects will be key in determining neutrino masses considering that the effect of massive neutrinos on the angular matter power spectrum is brought about on small scales. Therefore, a natural extension of the analysis presented in Chapter 2 should divide the galaxy sample in more red-shift bins. Scales up to $\ell = 2000$ should be included and the likelihood adapted for a possible error covering insensitivities to the deep non-linear regime. This extension requires an optimisation of the computing tools used in Ref. [31] (i.e., both Boltzmann and MCMC codes) which is currently under development.

One of the main scientific objectives of future galaxy surveys is to understand the nature of dark energy and dark matter. By using weak lensing and galaxy clustering, an Euclid-like survey will be able to constrain dark energy parameters and distinguish General Relativity from a wide range of modified gravity theories. Dark energy anisotropic stress is a key feature since it allows to discriminate the standard dynamical dark energy model – a scalar field minimally coupled to gravity – from the so-called modified gravity models. In linear theory, the former class of models does not support any anisotropic stress whereas models such as scalar-tensor and $f(R)$ generically have a non-zero anisotropic stress. Determining how well anisotropic dark energy will be constrained by the combination of data from both Planck-like and Euclid-like satellites is therefore a challenging problem. A phenomenological approach could be suitable to deliver satisfactory results. In Ref. [30], Lukas Hollenstein, Martin Kunz, and I have worked on a phenomenological model of anisotropic dark energy which combines both internally and externally sourced anisotropic stress, that also allows for a scale dependence. Our model comprehends, for instance, models of dark energy coupled to dark matter, modified gravity models, and isotropic dark energy. In our analysis we constrained the parameter space of the model using mainly observations of the CMB from the Planck satellite. Large-scale structure observations were not included in the analysis but meanwhile the tools to include the angular matter power spectrum have been developed. We have shown that the dark energy anisotropic stress might act as a source of both dark matter and dark energy perturbations. It would therefore be very important to investigate to what extent observations of galaxy clustering could improve our results in Ref. [30]. The detection of a non-zero anisotropic stress would play a key role in our understanding of the fundamental causes of the universe's late-time acceleration.

Appendices

Appendix A

Stability

The non-autonomous system of coupled differential equations (1.2)–(1.3) for density and velocity perturbations can be written as

$$\vec{\mathbf{x}}' = \mathbf{B}(a;\theta_j)\,\vec{\mathbf{x}}\,, \tag{A.1}$$

where $\vec{\mathbf{x}}^{\intercal} = (\delta_m,\, V_m,\, \delta_{de},\, V_{de})$, $\mathbf{B}$ is a 4×4 matrix which depends on the parameters $\theta_j = \{H_0,\, w,\, \Omega_m,\, \Omega_x,\, c_s,\, e_\pi,\, f_\pi,\, g_\pi\}$, on the mode k and the scale factor a. In order to obtain information about the parameter space, we assess the stability of the system (A.1). We compute the eigenvalues $\lambda_k(a,\,\theta_j)$ of the matrix $\mathbf{B}(a;\theta_j)$ numerically and look at the regions in the θ_j-space where all eigenvalues have negative real parts for the whole time interval we consider, that is, from matter domination to the present time.

For the system (A.1) we find one eigenvalue which does not have a region in θ_j-space where $\mathrm{Re}\,(\lambda_k(a,\,\theta_j)) < 0$. Then, since we know that in matter dominated era and on sub-horizon scales matter perturbations grow linearly, that is, $\delta_m \propto a$, we use the following approach to assess the stability of the system. First, we rescale the variables $\vec{\mathbf{x}}$ dividing them by a power a^m of the scale factor, $\vec{\mathbf{y}} = a^{-m}\vec{\mathbf{x}}$. It follows that the system (A.1) becomes

$$\vec{\mathbf{y}}' = \mathbf{A}(a;\theta_j)\,\vec{\mathbf{y}}\,, \tag{A.2}$$

where $\mathbf{A}(a;\theta_j) = \mathbf{B}(a;\theta_j) - \frac{m}{a}\mathbf{I}$, with $\mathbf{I}$ the identity matrix. Second, we find regions in parameter space where all the eigenvalues of the matrix $\mathbf{A}$ have negative real parts. We study models with $e_\pi = g_\pi = 0$ since the effective sound speed c^2_{eff} is only defined in terms of c_s and f_π; moreover we check the robustness of our method with

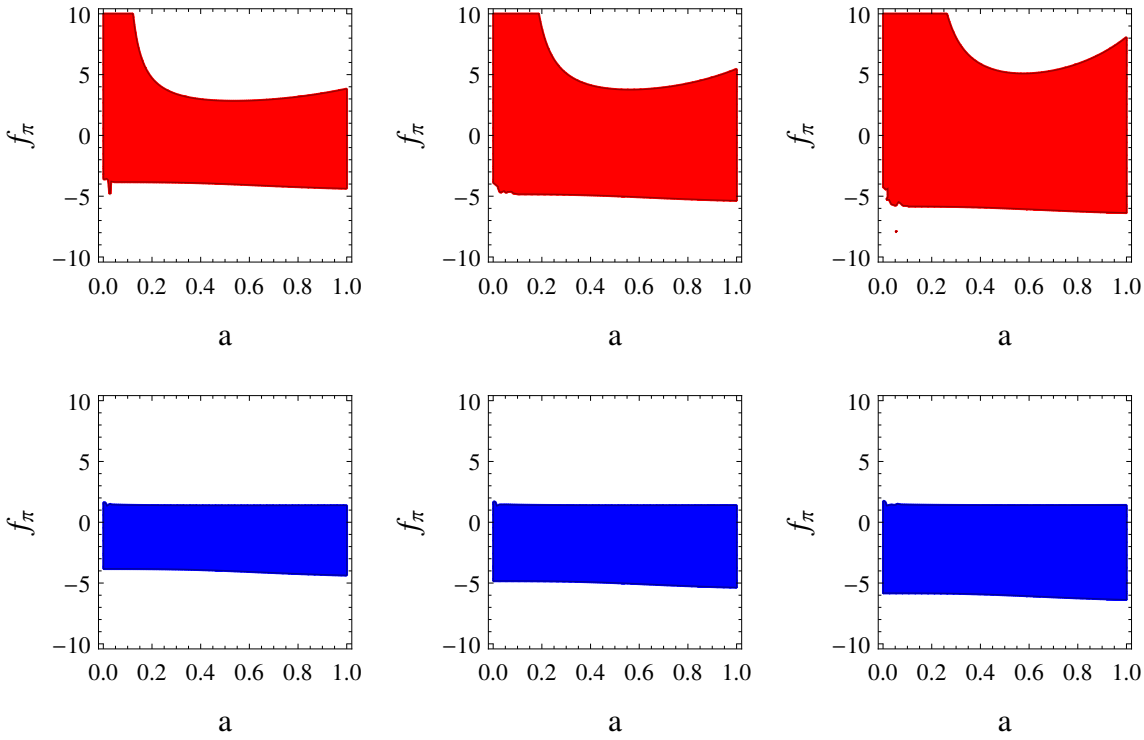

Fig. *A.1: The figure shows the region in the $f_\pi-$space for which all the eigenvalues of the matrix* **A** *in Eq. (A.2) have negative real parts. The red region (upper panel) corresponds to a mode on super-horizon scales ($k = 5H_0$) in matter domination. The blue region (lower panel) shows a sub-horizon mode ($k = 300H_0$). We have used $c_s^2 = 1$, $w = -1.05$, $e_\pi = 0$ and $g_\pi = 0$. In each column, from left to right, we rescale the variables by using powers $m = 2, 3, 4$.*

different powers m. Figure A.1 shows regions where all eigenvalues have real part negative in the time interval relevant for both super and sub-horizon scales. Since we use $c_s^2 = 1$ we can see clearly an upper limit on $f_\pi = 3/2$, which nicely agrees with $c_{\rm eff}^2 > 0$.

Then we study the impact of the parameter g_π on the stability of the system. For a given scale factor a we determine regions in the plane $c_{\rm eff} - f_\pi$ for which the system (A.2) is stable for both $g_\pi \gg 1$ and $g_\pi \ll 1$. Figure A.2 shows again the stable regions for large and small scales.

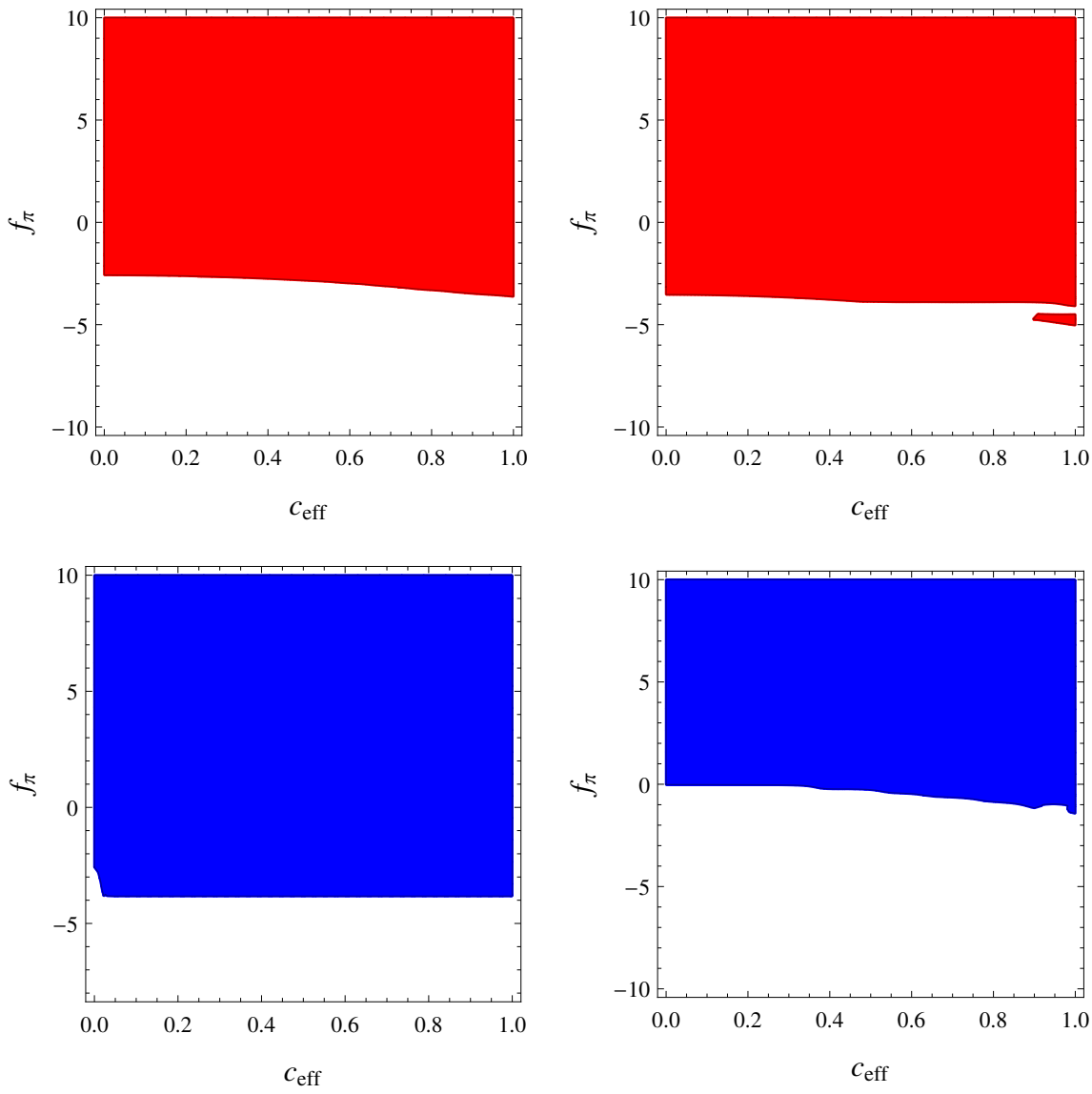

Fig. *A.2: Stability regions: parameter regions where the perturbations grow more slowly than* a^2 *at* $a = 5 \times 10^{-2}$*, for* $w = -1.05$ *and* $e_\pi = 0$*. The upper row (red contours) are for* $k = 5H_0$*, while the lower row (blue contours) is for* $k = 300H_0$*. The right panels are for* $g_\pi = 10^{-5}$ *and the left panels for* $g_\pi = 10^5$*.*

Appendix B

General solutions

In Section 1.3 we study some limiting cases in the 4−dimensional system (1.2)–(1.3) for which dark matter and dark energy perturbations decouple from each other. In this appendix we give some solutions which are a bit cumbersome to be written in the main body of the paper.

On sub-horizon scales and during matter dominance, dark energy density perturbations are governed by Eq. (1.16) whose full solution is

$$\begin{aligned}
\delta_{de} &= \left(\frac{c_{\rm eff}k}{\mathcal{H}}\right) a^{\alpha_8} \left\{ A_5\, J_{-\nu_5}\left(\frac{2c_{\rm eff}k}{\mathcal{H}}\right) + A_6\, J_{\nu_5}\left(\frac{2c_{\rm eff}k}{\mathcal{H}}\right)\right\} \\
&+ e_\pi \beta_6\, a^{\alpha_7} \left(\frac{c_{\rm eff}k}{\mathcal{H}}\right)^{\alpha_6} J_{\nu_5}\left(\frac{2c_{\rm eff}k}{\mathcal{H}}\right) {}_1\tilde{F}_2\left(\nu_6\,;\,\alpha_6\,,\nu_7\,;-\frac{k^2c_{\rm eff}^2}{\mathcal{H}^2}\right) \\
&- e_\pi \beta_7 a^{\alpha_7} \left(\frac{c_{\rm eff}k}{\mathcal{H}}\right)^{\alpha_9} J_{-\nu_5}\left(\frac{2c_{\rm eff}k}{\mathcal{H}}\right) {}_1\tilde{F}_2\left(\nu_8\,;\,\alpha_9\,,\nu_9\,;-\frac{k^2c_{\rm eff}^2}{\mathcal{H}^2}\right),
\end{aligned} \tag{B.1}$$

where

$$\begin{aligned}
\nu_5^2 &= \frac{432c_{\rm eff}^4 + 48f_\pi^2 + 72c_{\rm eff}^2(-1+4f_\pi-6w) + 3(1+6w)^2}{12} \\
&- \frac{8f_\pi(3+4g_\pi^2+18w)}{12}\,,
\end{aligned} \tag{B.2}$$

$$\nu_6 = -\frac{5}{4} - f_\pi + n + \frac{3w-\nu_5}{2}\,, \tag{B.3}$$

$$\nu_7 = \nu_6 + 1\,, \tag{B.4}$$
$$\nu_8 = -\frac{5}{4} - f_\pi + n + \frac{3w+\nu_5}{2}\,, \tag{B.5}$$
$$\nu_9 = \nu_8 + 1\,, \tag{B.6}$$
$$\alpha_6 = 1 - \nu_5\,, \tag{B.7}$$
$$\alpha_7 = -2(1+f_\pi) + 3w + n\,, \tag{B.8}$$
$$\alpha_8 = -f_\pi + \frac{3w}{2} - \frac{3}{4}\,, \tag{B.9}$$
$$\alpha_9 = 1 + \nu_5\,, \tag{B.10}$$

$$\begin{aligned}\beta_6 &= \frac{1}{24}\frac{c_{\rm eff}^{-2-4f_\pi+6w}k^{-4f_\pi+6w}}{H_0^{2-4f_\pi+6w}}\Omega_m^{-1+2f_\pi-3w}\pi\delta_0\csc(\pi\nu_5)\\ &\times \Gamma(\alpha_6)\,\Gamma(\nu_6)\,\Gamma(\alpha_9)\,,\end{aligned} \tag{B.11}$$
$$\begin{aligned}\beta_7 &= \frac{1}{24}\frac{c_{\rm eff}^{-2-4f_\pi+6w}k^{-4f_\pi+6w}}{H_0^{2-4f_\pi+6w}}\Omega_m^{-1+2f_\pi-3w}\pi\delta_0\csc(\pi\nu_5)\\ &\times \Gamma(\alpha_6)\,\Gamma(\nu_9)\,\Gamma(\alpha_9)\,,\end{aligned} \tag{B.12}$$

A_5, A_6 are constants of integration and ${}_1\tilde{F}_2$ stands for the regularized generalized hypergeometric function. The last two terms in Eq. (B.1) are due to the external anisotropic stress.

On the other hand, for sub-sound horizon scales, during dark energy domination and without external contribution to the dark energy anisotropic stress ($e_\pi = 0$), we find (by using Eq. (1.35)) for dark energy velocity perturbations

$$\begin{aligned}V_{de} =& \frac{1}{2}\left(\frac{x_3}{2}\right)^{\frac{1-\alpha_4}{1+3w}}\Bigg\{\left[6(c_s^2-w)+1-\alpha_4\right]\times\\ &\times\left[B_4\,\Gamma\left(\frac{2+3w-\alpha_4}{1+3w}\right)J_{-\nu_1}(x_3) + A_4\,\Gamma\left(\frac{3w+\alpha_4}{1+3w}\right)J_{\nu_1}(x_3)\right]\\ &+\frac{x_3(1+3w)}{4}\left[B_4\,\Gamma\left(\frac{2+3w-\alpha_4}{1+3w}\right)\left[J_{-1-\nu_1}(x_3) - J_{1-\nu_1}(x_3)\right]\right.\\ &\left.+\,A_4\,\Gamma\left(\frac{3w+\alpha_4}{1+3w}\right)\left[J_{-1+\nu_1}(x_3) - J_{1+\nu_1}(x_3)\right]\right]\Bigg\}\,,\end{aligned} \tag{B.13}$$

while for dark matter velocity perturbations

$$
\begin{aligned}
V_m &= \frac{3(1+2f_\pi)}{1+3w} 2^{-\frac{2-\alpha_4+\nu_1+3w(1+\nu_1)}{1+3w}} x_3^{-\frac{-1+\alpha_4+\nu_1+3w\nu_1}{1+3w}} \Bigg\{ A_4\, x_3^{2\nu_1} \\
&\times \Gamma\left(\frac{3w+\alpha_4}{1+3w}\right) \Gamma\left(\frac{2-\alpha_4+3w(\nu_1-1)+\nu_1}{2+6w}\right) \\
&\times {}_1F_2\left(\left\{\frac{2-\alpha_4+3w(\nu_1-1)+\nu_1}{2+6w}\right\}, \right. \\
&\quad \left. \left\{1+\nu_1,\, \frac{4-\alpha_4+\nu_1+3w(1+\nu_1)}{2+6w}\right\}, -\frac{1}{4}x_3^2\right) \\
&+ B_4\, 4^{\nu_1} \Gamma\left(\frac{2+3w-\alpha_4}{1+3w}\right) \Gamma\left(-\frac{-2+\alpha_4+\nu_1+3w(1+\nu_1)}{2+6w}\right) \\
&\times {}_1F_2\left(\left\{\frac{2-\alpha_4-3w(\nu_1+1)-\nu_1}{2+6w}\right\}, \right. \\
&\quad \left. \left\{1-\nu_1,\, \frac{4-\alpha_4-\nu_1-3w(-1+\nu_1)}{2+6w}\right\}, -\frac{1}{4}x_3^2\right) \Bigg\}, \qquad \text{(B.14)}
\end{aligned}
$$

where α_4, ν_1 and x_3 are given by Eq. (1.36). By means of this solution we can easily find an expression for dark matter density perturbations by solving the differential equation

$$
\delta_m' = \frac{V_m}{a}\,. \qquad \text{(B.15)}
$$

Appendix C

Basic expressions for the Fisher analysis

The Fisher information matrix $F_{\alpha\beta}$ is given by

$$F_{\alpha\beta} = \sum_{\ell=2}^{\ell_{\rm max}} \sum_{(ij)(pq)} \frac{\partial C_\ell^{ij}}{\partial\theta_\alpha} \frac{\partial C_\ell^{pq}}{\partial\theta_\beta} {\rm Cov}^{-1}_{C_{\ell\,[({\rm ij}),({\rm pq})]}}\,, \tag{C.1}$$

where θ_a denotes a given cosmological parameter, C_ℓ^{ij} is the number counts angular power spectrum of Eq. (2.5), and the covariance matrix ${\rm Cov}^{-1}_{C_{\ell\,[({\rm ij}),({\rm pq})]}}$ is

$${\rm Cov}_{C_{\ell\,[({\rm ij}),({\rm pq})]}} = \frac{C_\ell^{{\rm A},({\rm ip})} C_\ell^{{\rm A},({\rm jq})} + C_\ell^{{\rm A},({\rm iq})} C_\ell^{{\rm A},({\rm jp})}}{(2\ell+1) f_{\rm sky}}, \tag{C.2}$$

where $A = $ obs, th; $i, j, p, q = 1, ..., N_{\rm bin}$; and $f_{\rm sky}$ is the covered sky fraction. The derivatives in Eq. (C.1) are computed with a five-point stencil [97]; we choose the step for each parameter with an iterative procedure: the step is chosen to be of the same size as the 1-σ widths obtained when fixing the other parameters $\sigma_{\theta_\alpha} = 1/\sqrt{F_{\alpha\alpha}}$. We have verified that our results are not significantly affected by the particular step values. Since we treat non-linearities in a conservative way, we sum up to $\ell_{\rm max} = 400$. The second sum in Eq. (C.1) is over the couple of matrix indices (ij) and (pq) with $i \leq j$ and $p \leq q$ which run from 1 to the total number of bins $N_{\rm bin}$ when all bin auto- and cross-correlations are taken into account.

In an analysis only including auto-correlations the covariance matrix (C.2) must be first reduced to the relevant components, and subsequently inverted. We denote the

number counts angular power spectrum of a model neglecting lensing convergence by $\widetilde{C}_\ell$. The shift in the best-fit values due to neglecting lensing convergence is estimated through the systematic error [106, 108, 162, 163]

$$\Delta C_\ell = C_\ell^{\rm obs} - \widetilde{C}_\ell \tag{C.3}$$

where $C_\ell^{\rm obs}$ consistently includes lensing convergence. The bias induced by incomplete modelling of number counts angular power spectrum is then given by

$$\Delta_{\theta_\alpha} = \sum_\beta \left[\left(\widetilde{F}\right)^{-1}\right]_{\alpha\beta} B_\beta \ , \tag{C.4}$$

where

$$B_\beta \equiv \sum_{(ij)(pq)} \sum_\ell \Delta C_\ell^{ij} \frac{\partial \widetilde{C}_\ell^{pq}}{\partial \theta_\beta} {\rm Cov}^{-1}_{\widetilde{C}_{\ell\,[({\rm ij}),({\rm pq})]}} \ , \tag{C.5}$$

and a tilde always denote the quantity computed according to the model neglecting lensing convergence. This expression assumes that the systematic error does not affect the covariance. Moreover, it is only valid if the shifts (C.4) are small compared to the variances $\Delta^2_{\theta_\alpha}/\sigma^2_{\theta_\alpha} < 1$. The MCMC analysis shows that biases in cosmological parameters due to neglecting lensing convergence easily reach several standard deviations, so none of these assumptions is satisfied in our case. Another point worth noticing is that Eq. (C.1) can only be used to estimate error contours by assuming that the underlying universe is described either by C_ℓ or by $\tilde{C}_\ell$, and does not give information about error contours obtained when fitting the wrong model $\tilde{C}_\ell$ to data consistent with the full C_ℓ spectra. This signifies an advantage of the MCMC approach over the Fisher matrix technique, as shown in Chapter 2.

Bibliography

[1] E. Hubble, *A relation between distance and radial velocity among extra-galactic nebulae*, *Proc. Nat. Acad. Sci.* **15** (1929) 168–173.

[2] G. Gamow, *Expanding universe and the origin of elements*, *Phys. Rev.* **70** (1946) 572–573.

[3] R. A. Alpher, H. Bethe, and G. Gamow, *The origin of chemical elements*, *Phys. Rev.* **73** (1948) 803–804.

[4] G. Gamow, *On Relativistic Cosmogony*, *Rev. Mod. Phys.* **21** (1949) 367–373.

[5] R. A. Alpher and R. C. Herman, *Theory of the Origin and Relative Abundance Distribution of the Elements*, *Rev. Mod. Phys.* **22** (1950) 153–212.

[6] A. A. Penzias and R. W. Wilson, *A Measurement of excess antenna temperature at 4080-Mc/s*, *Astrophys. J.* **142** (1965) 419–421.

[7] **Supernova Search Team** Collaboration, A. G. Riess et al., *Observational evidence from supernovae for an accelerating universe and a cosmological constant*, *Astron. J.* **116** (1998) 1009–1038, [astro-ph/9805201].

[8] **Supernova Cosmology Project** Collaboration, S. Perlmutter et al., *Measurements of Omega and Lambda from 42 high redshift supernovae*, *Astrophys. J.* **517** (1999) 565–586, [astro-ph/9812133].

[9] H. P. Robertson, *Kinematics and World-Structure*, *Astrophys. J.* **82** (1935) 284–301.

[10] A. G. Walker, *On Milnes's Theory of World-Structure*, *Procedings of the London Mathematical Society* **s2-42** (1937), no. 1937 90–127.

[11] C. Caprini, S. Biller, and P. G. Ferreira, *Constraints on the electrical charge asymmetry of the universe*, *JCAP* **0502** (2005) 006, [hep-ph/0310066].

[12] A. Friedman, *On the Curvature of space*, *Z. Phys.* **10** (1922) 377–386. [Gen. Rel. Grav.31,1991(1999)].

[13] A. Friedmann, *On the Possibility of a world with constant negative curvature of space*, *Z. Phys.* **21** (1924) 326–332. [Gen. Rel. Grav.31,2001(1999)].

[14] G. Lemaitre, *A homogeneous Universe of constant mass and growing radius accounting for the radial velocity of extragalactic nebulae*, *Annales Soc. Sci. Brux. Ser. I Sci. Math. Astron. Phys.* **A47** (1927) 49–59.

[15] G. Lemaitre, *The Expanding Universe*, *Mon. Not. Roy. Astron. Soc.* **91** (1931) 490–501.

[16] F. Zwicky, *Die Rotverschiebung von extragalaktischen Nebeln*, *Helv. Phys. Acta* **6** (1933) 110–127.

[17] A. H. Guth and D. I. Kaiser, *Inflationary cosmology: Exploring the Universe from the smallest to the largest scales*, *Science* **307** (2005) 884–890, [astro-ph/0502328].

[18] G. F. Smoot et al., *Structure in the COBE differential microwave radiometer first year maps*, *Astrophys. J.* **396** (1992) L1–L5.

[19] **WMAP** Collaboration, C. L. Bennett et al., *First year Wilkinson Microwave Anisotropy Probe (WMAP) observations: Preliminary maps and basic results*, *Astrophys. J. Suppl.* **148** (2003) 1–27, [astro-ph/0302207].

[20] **Planck** Collaboration, P. A. R. Ade et al., *Planck 2013 results. I. Overview of products and scientific results*, *Astron. Astrophys.* **571** (2014) A1, [arXiv:1303.5062].

[21] **Planck** Collaboration, P. A. R. Ade et al., *Planck 2015 results. XIII. Cosmological parameters*, arXiv:1502.01589.

[22] **Planck** Collaboration, P. A. R. Ade et al., *Planck 2015 results. XVI. Isotropy and statistics of the CMB*, arXiv:1506.07135.

[23] **SDSS** Collaboration, M. Tegmark et al., *The 3-D power spectrum of galaxies from the SDSS*, *Astrophys. J.* **606** (2004) 702–740, [astro-ph/0310725].

[24] **SDSS** Collaboration, M. Tegmark et al., *Cosmological parameters from SDSS and WMAP*, *Phys. Rev.* **D69** (2004) 103501, [astro-ph/0310723].

[25] **SDSS** Collaboration, D. J. Eisenstein et al., *Detection of the baryon acoustic peak in the large-scale correlation function of SDSS luminous red galaxies*, *Astrophys. J.* **633** (2005) 560–574, [astro-ph/0501171].

[26] E. J. Copeland, M. Sami, and S. Tsujikawa, *Dynamics of dark energy*, *Int. J. Mod. Phys.* **D15** (2006) 1753–1936, [hep-th/0603057].

[27] T. Clifton, P. G. Ferreira, A. Padilla, and C. Skordis, *Modified Gravity and Cosmology*, *Phys. Rept.* **513** (2012) 1–189, [arXiv:1106.2476].

[28] **Planck** Collaboration, P. A. R. Ade et al., *Planck 2015 results. XVII. Constraints on primordial non-Gaussianity*, arXiv:1502.01592.

[29] **Planck** Collaboration, P. A. R. Ade et al., *Planck 2015 results. XX. Constraints on inflation*, arXiv:1502.02114.

[30] W. Cardona, L. Hollenstein, and M. Kunz, *The traces of anisotropic dark energy in light of Planck*, *JCAP* **1407** (2014) 032, [arXiv:1402.5993].

[31] W. Cardona, R. Durrer, M. Kunz, and F. Montanari, *Lensing convergence and the neutrino mass scale in galaxy redshift surveys*, arXiv:1603.06481.

[32] A. G. Riess et al., *A 2.4% Determination of the Local Value of the Hubble Constant*, arXiv:1604.01424.

[33] R. Durrer and R. Maartens, *Dark Energy and Modified Gravity*, arXiv:0811.4132.

[34] J. Frieman, M. Turner, and D. Huterer, *Dark Energy and the Accelerating Universe*, *Ann.Rev.Astron.Astrophys.* **46** (2008) 385–432, [arXiv:0803.0982].

[35] L. Amendola and S. Tsujikawa, *Dark Energy: Theory and Observations*. Cambridge University Press, 2010.

[36] **Euclid Theory Working Group** Collaboration, L. Amendola et al., *Cosmology and fundamental physics with the Euclid satellite*, *Living Rev.Rel.* **16** (2013) 6, [arXiv:1206.1225].

[37] M. Kunz, *The phenomenological approach to modeling the dark energy*, *Comptes Rendus Physique* **13** (2012) 539–565, [arXiv:1204.5482].

[38] R. A. Battye and J. A. Pearson, *Effective action approach to cosmological perturbations in dark energy and modified gravity*, *JCAP* **1207** (2012) 019, [arXiv:1203.0398].

[39] I. Sawicki, I. D. Saltas, L. Amendola, and M. Kunz, *Consistent perturbations in an imperfect fluid*, *JCAP* **1301** (2013) 004, [arXiv:1208.4855].

[40] T. Baker, P. G. Ferreira, and C. Skordis, *The Parameterized Post-Friedmann Framework for Theories of Modified Gravity: Concepts, Formalism and Examples*, *Phys.Rev.* **D87** (2013) 024015, [arXiv:1209.2117].

[41] G. Gubitosi, F. Piazza, and F. Vernizzi, *The Effective Field Theory of Dark Energy*, *JCAP* **1302** (2013) 032, [arXiv:1210.0201].

[42] J. K. Bloomfield, E. E. Flanagan, M. Park, and S. Watson, *Dark energy or modified gravity? An effective field theory approach*, *JCAP* **1308** (2013) 010, [arXiv:1211.7054].

[43] L. Amendola, M. Kunz, and D. Sapone, *Measuring the dark side (with weak lensing)*, *JCAP* **0804** (2008) 013, [arXiv:0704.2421].

[44] W. Hu and I. Sawicki, *A Parameterized Post-Friedmann Framework for Modified Gravity*, *Phys.Rev.* **D76** (2007) 104043, [arXiv:0708.1190].

[45] L. Amendola, M. Kunz, M. Motta, I. D. Saltas, and I. Sawicki, *Observables and unobservables in dark energy cosmologies*, *Phys.Rev.* **D87** (2013) 023501, [arXiv:1210.0439].

[46] M. Motta, I. Sawicki, I. D. Saltas, L. Amendola, and M. Kunz, *Probing Dark Energy through Scale Dependence*, *Phys.Rev.* **D88** (2013) 124035, [arXiv:1305.0008].

[47] M. Kunz and D. Sapone, *Dark Energy versus Modified Gravity*, *Phys.Rev.Lett.* **98** (2007) 121301, [astro-ph/0612452].

[48] I. D. Saltas and M. Kunz, *Anisotropic stress and stability in modified gravity models*, *Phys.Rev.* **D83** (2011) 064042, [arXiv:1012.3171].

[49] D. Sapone, *Dark Energy in Practice*, *Int.J.Mod.Phys.* **A25** (2010) 5253–5331, [arXiv:1006.5694].

[50] J. M. Bardeen, *Gauge Invariant Cosmological Perturbations*, *Phys.Rev.* **D22** (1980) 1882–1905.

[51] H. Kodama and M. Sasaki, *Cosmological Perturbation Theory*, *Prog.Theor.Phys.Suppl.* **78** (1984) 1–166.

[52] C.-P. Ma and E. Bertschinger, *Cosmological perturbation theory in the synchronous and conformal Newtonian gauges*, *Astrophys.J.* **455** (1995) 7–25, [astro-ph/9506072].

[53] G. Ballesteros, L. Hollenstein, R. K. Jain, and M. Kunz, *Nonlinear cosmological consistency relations and effective matter stresses*, *JCAP* **1205** (2012) 038, [arXiv:1112.4837].

[54] K. Koyama and R. Maartens, *Structure formation in the dgp cosmological model*, *JCAP* **0601** (2006) 016, [astro-ph/0511634].

[55] Y.-S. Song, L. Hollenstein, G. Caldera-Cabral, and K. Koyama, *Theoretical Priors On Modified Growth Parametrisations*, *JCAP* **1004** (2010) 018, [arXiv:1001.0969].

[56] T. Koivisto and D. F. Mota, *Dark energy anisotropic stress and large scale structure formation*, *Phys.Rev.* **D73** (2006) 083502, [astro-ph/0512135].

[57] D. Mota, J. Kristiansen, T. Koivisto, and N. Groeneboom, *Constraining Dark Energy Anisotropic Stress*, *Mon.Not.Roy.Astron.Soc.* **382** (2007) 793–800, [arXiv:0708.0830].

[58] D. Sapone and E. Majerotto, *Fingerprinting Dark Energy III: distinctive marks of viscosity*, *Phys.Rev.* **D85** (2012) 123529, [arXiv:1203.2157].

[59] D. Sapone, E. Majerotto, M. Kunz, and B. Garilli, *Can dark energy viscosity be detected with the Euclid survey?*, *Phys.Rev.* **D88** (2013) 043503, [arXiv:1305.1942].

[60] W. Hu, *Structure formation with generalized dark matter*, *Astrophys.J.* **506** (1998) 485–494, [astro-ph/9801234].

[61] D. Sapone and M. Kunz, *Fingerprinting dark energy*, *Phys. Rev. D* **80** (Oct, 2009) 083519.

[62] A. Lewis and S. Bridle, *Cosmological parameters from CMB and other data: A Monte Carlo approach*, *Phys.Rev.* **D66** (2002) 103511, [astro-ph/0205436].

[63] A. Lewis and S. Bridle, *Cosmological MonteCarlo (CosmoMC)*, 2013. Publicly available Markov-Chain Monte-Carlo likelihood sampler: http://cosmologist.info/cosmomc.

[64] A. Lewis, A. Challinor, and A. Lasenby, *Efficient Computation of Cosmic Microwave Background Anisotropies in Closed Friedmann-Robertson-Walker Models*, *Astrophys.J.* **538** (2000) 473–476, [astro-ph/9911177].

[65] A. Lewis and A. Challinor, *Code for Anisotropies in the Microwave Background (CAMB)*, 2013. Publicly available CMB-Boltzmann code: http://www.camb.info.

[66] O. Pisanti, A. Cirillo, S. Esposito, F. Iocco, G. Mangano, et al., *PArthENoPE: Public Algorithm Evaluating the Nucleosynthesis of Primordial Elements*, *Comput.Phys.Commun.* **178** (2008) 956–971, [arXiv:0705.0290].

[67] **Planck collaboration** Collaboration, P. Ade et al., *Planck 2013 results. XV. CMB power spectra and likelihood*, arXiv:1303.5075.

[68] **Planck Collaboration** Collaboration, P. Ade et al., *Planck 2013 results. XVI. Cosmological parameters*, arXiv:1303.5076.

[69] **WMAP** Collaboration, C. Bennett, D. Larson, J. Weiland, N. Jarosik, G. Hinshaw, et al., *Nine-Year Wilkinson Microwave Anisotropy Probe (WMAP) Observations: Final Maps and Results*, *Astrophys.J.Suppl.* **208** (2013) 20, [arXiv:1212.5225].

[70] K. Story, C. Reichardt, Z. Hou, R. Keisler, K. Aird, et al., *A Measurement of the Cosmic Microwave Background Damping Tail from the 2500-square-degree SPT-SZ survey*, *Astrophys.J.* **779** (2013) 86, [arXiv:1210.7231].

[71] S. Das, T. Louis, M. R. Nolta, G. E. Addison, E. S. Battistelli, et al., *The Atacama Cosmology Telescope: Temperature and Gravitational Lensing Power Spectrum Measurements from Three Seasons of Data*, *JCAP* **1404** (2014) 014, [arXiv:1301.1037].

[72] **SDSS Collaboration** Collaboration, W. J. Percival et al., *Baryon Acoustic Oscillations in the Sloan Digital Sky Survey Data Release 7 Galaxy Sample*, *Mon.Not.Roy.Astron.Soc.* **401** (2010) 2148–2168, [arXiv:0907.1660].

[73] N. Padmanabhan, X. Xu, D. J. Eisenstein, R. Scalzo, A. J. Cuesta, et al., *A 2Methods and Application to the Sloan Digital Sky Survey*, *Mon.Not.Roy.Astron.Soc.* **427** (2012) 2132, [arXiv:1202.0090].

[74] F. Beutler, C. Blake, M. Colless, D. H. Jones, L. Staveley-Smith, et al., *The 6dF Galaxy Survey: Baryon Acoustic Oscillations and the Local Hubble*

Constant, *Mon.Not.Roy.Astron.Soc.* **416** (2011) 3017–3032, [arXiv:1106.3366].

[75] C. Blake, E. Kazin, F. Beutler, T. Davis, D. Parkinson, et al., *The WiggleZ Dark Energy Survey: mapping the distance-redshift relation with baryon acoustic oscillations*, *Mon.Not.Roy.Astron.Soc.* **418** (2011) 1707–1724, [arXiv:1108.2635].

[76] L. Anderson, E. Aubourg, S. Bailey, D. Bizyaev, M. Blanton, et al., *The clustering of galaxies in the SDSS-III Baryon Oscillation Spectroscopic Survey: Baryon Acoustic Oscillations in the Data Release 9 Spectroscopic Galaxy Sample*, *Mon.Not.Roy.Astron.Soc.* **427** (2013), no. 4 3435–3467, [arXiv:1203.6594].

[77] A. Conley, J. Guy, M. Sullivan, N. Regnault, P. Astier, et al., *Supernova Constraints and Systematic Uncertainties from the First 3 Years of the Supernova Legacy Survey*, *Astrophys.J.Suppl.* **192** (2011) 1, [arXiv:1104.1443].

[78] A. G. Riess, L. Macri, S. Casertano, H. Lampeitl, H. C. Ferguson, A. V. Filippenko, S. W. Jha, W. Li, and R. Chornock, *A 3% Solution: Determination of the Hubble Constant with the Hubble Space Telescope and Wide Field Camera 3*, *Astrophys. J.* **730** (2011) 119, [arXiv:1103.2976]. [Erratum: Astrophys. J.732,129(2011)].

[79] M. Kilbinger, L. Fu, C. Heymans, F. Simpson, J. Benjamin, et al., *CFHTLenS: Combined probe cosmological model comparison using 2D weak gravitational lensing*, *Monthly Notices of the Royal Astronomical Society* **430** (2013), no. 3 2200–2220, [arXiv:1212.3338].

[80] **Planck Collaboration** Collaboration, P. Ade et al., *Planck 2013 results. XX. Cosmology from Sunyaev-Zeldovich cluster counts*, arXiv:1303.5080.

[81] R. Bean and O. Dore, *Probing dark energy perturbations: The Dark energy equation of state and speed of sound as measured by WMAP*, *Phys.Rev.* **D69** (2004) 083503, [astro-ph/0307100].

[82] R. de Putter, D. Huterer, and E. V. Linder, *Measuring the Speed of Dark: Detecting Dark Energy Perturbations*, *Phys.Rev.* **D81** (2010) 103513, [arXiv:1002.1311].

[83] M. Kunz, P.-S. Corasaniti, D. Parkinson, and E. J. Copeland, *Model-independent dark energy test with sigma(8) using results from the*

Wilkinson microwave anisotropy probe, *Phys.Rev.* **D70** (2004) 041301, [astro-ph/0307346].

[84] L. Hollenstein, D. Sapone, R. Crittenden, and B. M. Schaefer, *Constraints on early dark energy from CMB lensing and weak lensing tomography*, *JCAP* **0904** (2009) 012, [arXiv:0902.1494].

[85] L. Amendola and C. Quercellini, *Skewness as a test of the equivalence principle*, *Phys.Rev.Lett.* **92** (2004) 181102, [astro-ph/0403019].

[86] E. V. Linder, *Cosmic growth history and expansion history*, *Phys.Rev.* **D72** (2005) 043529, [astro-ph/0507263].

[87] L. Pogosian, A. Silvestri, K. Koyama, and G.-B. Zhao, *How to optimally parametrize deviations from General Relativity in the evolution of cosmological perturbations?*, *Phys.Rev.* **D81** (2010) 104023, [arXiv:1002.2382].

[88] R. Bean and M. Tangmatitham, *Current constraints on the cosmic growth history*, *Phys.Rev.* **D81** (2010) 083534, [arXiv:1002.4197].

[89] J. Lesgourgues and S. Pastor, *Massive neutrinos and cosmology*, *Phys. Rept.* **429** (2006) 307–379, [astro-ph/0603494].

[90] J. Lesgourgues and S. Pastor, *Neutrino mass from Cosmology*, *Adv. High Energy Phys.* **2012** (2012) 608515, [arXiv:1212.6154].

[91] W. Hu, D. J. Eisenstein, and M. Tegmark, *Weighing neutrinos with galaxy surveys*, *Phys. Rev. Lett.* **80** (1998) 5255–5258, [astro-ph/9712057].

[92] H. A. Feldman, N. Kaiser, and J. A. Peacock, *Power spectrum analysis of three-dimensional redshift surveys*, *Astrophys. J.* **426** (1994) 23–37, [astro-ph/9304022].

[93] E. Di Dio, F. Montanari, R. Durrer, and J. Lesgourgues, *Cosmological Parameter Estimation with Large Scale Structure Observations*, *JCAP* **1401** (2014) 042, [arXiv:1308.6186].

[94] C. Bonvin and R. Durrer, *What galaxy surveys really measure*, *Phys. Rev.* **D84** (2011) 063505, [arXiv:1105.5280].

[95] A. Challinor and A. Lewis, *The linear power spectrum of observed source number counts*, *Phys. Rev.* **D84** (2011) 043516, [arXiv:1105.5292].

[96] J. Yoo, N. Hamaus, U. Seljak, and M. Zaldarriaga, *Going beyond the Kaiser redshift-space distortion formula: a full general relativistic account of the effects and their detectability in galaxy clustering*, *Phys. Rev.* **D86** (2012) 063514, [arXiv:1206.5809].

[97] F. Montanari and R. Durrer, *Measuring the lensing potential with tomographic galaxy number counts*, *JCAP* **1510** (2015), no. 10 070, [arXiv:1506.01369].

[98] E. Di Dio, F. Montanari, J. Lesgourgues, and R. Durrer, *The CLASSgal code for Relativistic Cosmological Large Scale Structure*, *JCAP* **1311** (2013) 044, [arXiv:1307.1459].

[99] **WMAP** Collaboration, L. Verde et al., *First year Wilkinson Microwave Anisotropy Probe (WMAP) observations: Parameter estimation methodology*, *Astrophys. J. Suppl.* **148** (2003) 195, [astro-ph/0302218].

[100] T. Namikawa, T. Okamura, and A. Taruya, *Magnification effect on the detection of primordial non-Gaussianity from photometric surveys*, *Phys. Rev.* **D83** (2011) 123514, [arXiv:1103.1118].

[101] C. Duncan, B. Joachimi, A. Heavens, C. Heymans, and H. Hildebrandt, *On the complementarity of galaxy clustering with cosmic shear and flux magnification*, *Mon. Not. Roy. Astron. Soc.* **437** (2014), no. 3 2471–2487, [arXiv:1306.6870].

[102] J. Lesgourgues, *The Cosmic Linear Anisotropy Solving System (CLASS) I: Overview*, arXiv:1104.2932.

[103] **VIRGO Consortium** Collaboration, R. E. Smith, J. A. Peacock, A. Jenkins, S. D. M. White, C. S. Frenk, F. R. Pearce, P. A. Thomas, G. Efstathiou, and H. M. P. Couchmann, *Stable clustering, the halo model and nonlinear cosmological power spectra*, *Mon. Not. Roy. Astron. Soc.* **341** (2003) 1311, [astro-ph/0207664].

[104] B. Audren, J. Lesgourgues, S. Bird, M. G. Haehnelt, and M. Viel, *Neutrino masses and cosmological parameters from a Euclid-like survey: Markov Chain Monte Carlo forecasts including theoretical errors*, *JCAP* **1301** (2013) 026, [arXiv:1210.2194].

[105] D. J. Eisenstein and W. Hu, *Baryonic features in the matter transfer function*, *Astrophys. J.* **496** (1998) 605, [astro-ph/9709112].

[106] S. Camera, R. Maartens, and M. G. Santos, *Einstein's legacy in galaxy surveys*, *Mon. Not. Roy. Astron. Soc.* **451** (2015), no. 1 L80–L84, [arXiv:1412.4781].

[107] A. Raccanelli, F. Montanari, D. Bertacca, O. Doré, and R. Durrer, *Cosmological Measurements with General Relativistic Galaxy Correlations*, *JCAP* **1605** (2016), no. 05 009, [arXiv:1505.06179].

[108] T. D. Kitching, A. Amara, F. B. Abdalla, B. Joachimi, and A. Refregier, *Cosmological Systematics Beyond Nuisance Parameters : Form Filling Functions*, *Mon. Not. Roy. Astron. Soc.* **399** (2009) 2107, [arXiv:0812.1966].

[109] R. Trotta, *Applications of Bayesian model selection to cosmological parameters*, *Mon. Not. Roy. Astron. Soc.* **378** (2007) 72–82, [astro-ph/0504022].

[110] Y. Dirian, S. Foffa, M. Kunz, M. Maggiore, and V. Pettorino, *Non-local gravity and comparison with observational datasets. II. Updated results and Bayesian model comparison with ΛCDM*, *JCAP* **1605** (2016), no. 05 068, [arXiv:1602.03558].

[111] H. Jeffreys, *The Theory of Probability*. Oxford Classic Texts in the Physical Sciences. 1939.

[112] A. Heavens, *3d weak lensing*, *Mon. Not. Roy. Astron. Soc.* **343** (2003) 1327, [astro-ph/0304151].

[113] W. L. Freedman, *Determination of the Hubble Constant*, 9612024.

[114] W. L. Freedman and B. F. Madore, *The Hubble Constant*, *Ann. Rev. Astron. Astrophys.* **48** (2010) 673–710, [arXiv:1004.1856].

[115] W. Freedman, B. Madore, and B. Gibson, *Final Results from the Hubble Space Telescope Key Project to Measure the Hubble Constant*, *The Astrophysical Journal* **553** (2001) 47–72.

[116] A. G. Riess et al., *A Redetermination of the Hubble Constant with the Hubble Space Telescope from a Differential Distance Ladder*, *Astrophys. J.* **699** (2009) 539–563, [arXiv:0905.0695].

[117] G. Efstathiou, *H0 Revisited*, *Mon. Not. Roy. Astron. Soc.* **440** (2014), no. 2 1138–1152, [arXiv:1311.3461].

[118] E. M. L. Humphreys, M. J. Reid, J. M. Moran, L. J. Greenhill, and A. L. Argon, *Toward a New Geometric Distance to the Active Galaxy NGC 4258. III. Final Results and the Hubble Constant*, *Astrophys. J.* **775** (2013) 13, [arXiv:1307.6031].

[119] W. H. Press, *Understanding data better with Bayesian and global statistical methods*, in *Conference on Some Unsolved Problems in Astrophysics Princeton, New Jersey, April 27-29, 1995*, 1996. astro-ph/9604126.

[120] V. Marra, L. Amendola, I. Sawicki, and W. Valkenburg, *Cosmic Variance and the Measurement of the Local Hubble Parameter*, *Physical Review Letters* **110** (jun, 2013) 241305.

[121] C. Clarkson, O. Umeh, R. Maartens, and R. Durrer, *What is the distance to the CMB?*, *JCAP* **1411** (2014), no. 11 036, [arXiv:1405.7860].

[122] C. Bonvin, C. Clarkson, R. Durrer, R. Maartens, and O. Umeh, *Do we care about the distance to the CMB? Clarifying the impact of second-order lensing*, *JCAP* **1506** (2015), no. 06 050, [arXiv:1503.07831].

[123] S. Weinberg, *Gravitation and Cosmology*. John Wiley and Sons, New York, 1972.

[124] A. G. Riess et al., *New Hubble Space Telescope Discoveries of Type Ia Supernovae at z>=1: Narrowing Constraints on the Early Behavior of Dark Energy*, *Astrophys. J.* **659** (2007) 98–121, [astro-ph/0611572].

[125] H. S. Leavitt and E. C. Pickering, *Periods of 25 Variable Stars in the Small Magellanic Cloud.*, *Harvard College Observatory Circular* **173** (Mar., 1912) 1–3.

[126] O. Lahav, S. L. Bridle, M. P. Hobson, A. N. Lasenby, and L. Sodre, Jr., *Bayesian 'hyper-parameters' approach to joint estimation: the hubble constant from cmb measurements*, *Mon. Not. Roy. Astron. Soc.* **315** (2000) L45, [astro-ph/9912105].

[127] S. E. Persson, B. F. Madore, W. Krzemiński, W. L. Freedman, M. Roth, and D. C. Murphy, *New Cepheid Period-Luminosity Relations for the Large Magellanic Cloud: 92 Near-Infrared Light Curves*, *The Astronomical Journal* **128** (Nov., 2004) 2239–2264.

[128] K. M. Sebo, D. Rawson, J. Mould, B. F. Madore, M. E. Putman, J. A. Graham, W. L. Freedman, B. K. Gibson, and L. M. Germany, *The Cepheid*

Period-Luminosity Relation in the Large Magellanic Cloud, *The Astrophysical Journal Supplement Series* **142** (Sept., 2002) 71–78.

[129] G. Pietrzynski et al., *An eclipsing binary distance to the Large Magellanic Cloud accurate to 2 per cent*, *Nature* **495** (2013) 76–79, [arXiv:1303.2063].

[130] F. van Leeuwen, M. W. Feast, P. A. Whitelock, and C. D. Laney, *Cepheid Parallaxes and the Hubble Constant*, *Mon. Not. Roy. Astron. Soc.* **379** (2007) 723–737, [arXiv:0705.1592].

[131] J. Polshaw et al., *A supernova distance to the anchor galaxy NGC 4258*, *Astron. Astrophys.* **580** (2015) L15, [arXiv:1509.00507].

[132] **WMAP** Collaboration, G. Hinshaw et al., *Nine-Year Wilkinson Microwave Anisotropy Probe (WMAP) Observations: Cosmological Parameter Results*, *Astrophys. J. Suppl.* **208** (2013) 19, [arXiv:1212.5226].

[133] D. W. Hogg, D. J. Eisenstein, M. R. Blanton, N. A. Bahcall, J. Brinkmann, J. E. Gunn, and D. P. Schneider, *Cosmic homogeneity demonstrated with luminous red galaxies*, *Astrophys. J.* **624** (2005) 54–58, [astro-ph/0411197].

[134] **WMAP** Collaboration, D. N. Spergel et al., *First year Wilkinson Microwave Anisotropy Probe (WMAP) observations: Determination of cosmological parameters*, *Astrophys. J. Suppl.* **148** (2003) 175–194, [astro-ph/0302209].

[135] **Planck** Collaboration, P. A. R. Ade et al., *Planck 2013 results. XXIII. Isotropy and statistics of the CMB*, *Astron. Astrophys.* **571** (2014) A23, [arXiv:1303.5083].

[136] C. Copi, D. Huterer, D. Schwarz, and G. Starkman, *The Uncorrelated Universe: Statistical Anisotropy and the Vanishing Angular Correlation Function in WMAP Years 1-3*, *Phys. Rev.* **D75** (2007) 023507, [astro-ph/0605135].

[137] M. Tegmark, A. de Oliveira-Costa, and A. Hamilton, *A high resolution foreground cleaned CMB map from WMAP*, *Phys. Rev.* **D68** (2003) 123523, [astro-ph/0302496].

[138] D. J. Schwarz, G. D. Starkman, D. Huterer, and C. J. Copi, *Is the low-l microwave background cosmic?*, *Phys. Rev. Lett.* **93** (2004) 221301, [astro-ph/0403353].

[139] P. Bielewicz, H. K. Eriksen, A. J. Banday, K. M. Gorski, and P. B. Lilje, *Multipole vector anomalies in the first-year WMAP data: A Cut-sky analysis*, *Astrophys. J.* **635** (2005) 750–760, [astro-ph/0507186].

[140] K. Land and J. Magueijo, *The Axis of evil*, *Phys. Rev. Lett.* **95** (2005) 071301, [astro-ph/0502237].

[141] H. K. Eriksen, F. K. Hansen, A. J. Banday, K. M. Gorski, and P. B. Lilje, *Asymmetries in the Cosmic Microwave Background anisotropy field*, *Astrophys. J.* **605** (2004) 14–20, [astro-ph/0307507]. [Erratum: Astrophys. J.609,1198(2004)].

[142] F. K. Hansen, A. J. Banday, K. M. Gorski, H. K. Eriksen, and P. B. Lilje, *Power Asymmetry in Cosmic Microwave Background Fluctuations from Full Sky to Sub-degree Scales: Is the Universe Isotropic?*, *Astrophys. J.* **704** (2009) 1448–1458, [arXiv:0812.3795].

[143] H. K. Eriksen, D. I. Novikov, P. B. Lilje, A. J. Banday, and K. M. Gorski, *Testing for non-Gaussianity in the WMAP data: Minkowski functionals and the length of the skeleton*, *Astrophys. J.* **612** (2004) 64–80, [astro-ph/0401276].

[144] H. K. Eriksen, A. J. Banday, K. M. Gorski, and P. B. Lilje, *The N-point correlation functions of the first-year Wilkinson Microwave Anisotropy Probe sky maps*, *Astrophys. J.* **622** (2005) 58–71, [astro-ph/0407271].

[145] C. Rath, P. Schuecker, and A. J. Banday, *Model-Independent Test for Scale-Dependent Non-Gaussianities in the Cosmic Microwave Background*, *Phys. Rev. Lett.* **102** (2009) 131301, [astro-ph/0702163].

[146] G. Rossmanith, C. Raeth, A. J. Banday, and G. Morfill, *Non-Gaussian Signatures in the five-year WMAP data as identified with isotropic scaling indices*, *Mon. Not. Roy. Astron. Soc.* **399** (2009) 1921–1933, [arXiv:0905.2854].

[147] P. Vielva, E. Martinez-Gonzalez, R. B. Barreiro, J. L. Sanz, and L. Cayon, *Detection of non-Gaussianity in the WMAP 1 - year data using spherical wavelets*, *Astrophys. J.* **609** (2004) 22–34, [astro-ph/0310273].

[148] M. Cruz, E. Martinez-Gonzalez, P. Vielva, and L. Cayon, *Detection of a non-gaussian spot in wmap*, *Mon. Not. Roy. Astron. Soc.* **356** (2005) 29–40, [astro-ph/0405341].

[149] J. Kim and P. Naselsky, *Anomalous parity asymmetry of the Wilkinson Microwave Anisotropy Probe power spectrum data at low multipoles*, *Astrophys. J.* **714** (2010) L265–L267, [arXiv:1001.4613].

[150] D. Larson, J. L. Weiland, G. Hinshaw, and C. L. Bennett, *Comparing Planck and WMAP: Maps, Spectra, and Parameters*, *Astrophys. J.* **801** (2015), no. 1 9, [arXiv:1409.7718].

[151] A. Bernui and M. J. Rebouças, *Mapping possible non-Gaussianity in the Planck maps*, *Astron. Astrophys.* **573** (2015) A114, [arXiv:1405.1128].

[152] A. Bernui, A. F. Oliveira, and T. S. Pereira, *North-South non-Gaussian asymmetry in PLANCK CMB maps*, *JCAP* **1410** (2014), no. 10 041, [arXiv:1404.2936].

[153] **Planck** Collaboration, P. A. R. Ade et al., *Planck 2013 results. XII. Diffuse component separation*, *Astron. Astrophys.* **571** (2014) A12, [arXiv:1303.5072].

[154] A. Bernui and M. J. Reboucas, *Searching for non-Gaussianity in the WMAP data*, *Phys. Rev.* **D79** (2009) 063528, [arXiv:0806.3758].

[155] A. Bernui and M. J. Reboucas, *Non-gaussianity in the foreground-reduced CMB maps*, *Phys. Rev.* **D81** (2010) 063533, [arXiv:0912.0269].

[156] A. Bernui and M. J. Reboucas, *Mapping the large-angle deviation from Gaussianity in simulated CMB maps*, *Phys. Rev.* **D85** (2012) 023522, [arXiv:1109.6086].

[157] W. A. Cardona, A. Bernui, and M. J. Reboucas, *A comparative study of non-Gaussianity in ILC-7yr CMB map*, *Int. J. Mod. Phys. Conf. Ser.* **18** (2012) 286–293, [arXiv:1305.5872].

[158] W. Cardona, A. Bernui, and M. J. Reboucas, *Two statistical procedures for mapping large-angle non-Gaussianity*, arXiv:1310.2667.

[159] Y. Akrami, Y. Fantaye, A. Shafieloo, H. K. Eriksen, F. K. Hansen, A. J. Banday, and K. M. Górski, *Power asymmetry in WMAP and Planck temperature sky maps as measured by a local variance estimator*, *Astrophys. J.* **784** (2014) L42, [arXiv:1402.0870].

[160] K. M. Gorski, *On Determining the spectrum of primordial inhomogeneity from the Cobe DMR sky maps. 1. Method*, *Astrophys. J.* **430** (1994) L85, [astro-ph/9403066].

[161] E. Hivon, K. M. Gorski, C. B. Netterfield, B. P. Crill, S. Prunet, and F. Hansen, *Master of the cosmic microwave background anisotropy power spectrum: a fast method for statistical analysis of large and complex cosmic microwave background data sets*, *Astrophys. J.* **567** (2002) 2, [astro-ph/0105302].

[162] L. Knox, R. Scoccimarro, and S. Dodelson, *The Impact of inhomogeneous reionization on cosmic microwave background anisotropy*, *Phys. Rev. Lett.* **81** (1998) 2004–2007, [astro-ph/9805012].

[163] A. F. Heavens, T. D. Kitching, and L. Verde, *On model selection forecasting, Dark Energy and modified gravity*, *Mon. Not. Roy. Astron. Soc.* **380** (2007) 1029–1035, [astro-ph/0703191].